UNIVERSITY OF PATRAS
DEPARTMENT OF MECHANICAL ENGINEERING & AERONAUTICS
DIVISION OF APPLIED ENGINEERING
LABORATORY OF TECHNOLOGY & STRENGTH OF MATERIALS

STUDENT THESIS

METHODOLOGY OF STRUCTURAL ANALYSIS IN A COMMERCIAL AIRCRAFT WING WITH DISTRIBUTED PROPULSION

GIANNELOS VASILEIOS

1067248

Supervisor
PROFESSOR LABEAS GEORGE

Student Thesis submitted at Department of Mechanical Engineering & Aeronautics at University of Patras

PATRAS, March 2024

University of Patras, Department of Mechanical Engineering & Aeronautics
GIANNELOS VASILEIOS

UNIVERSITY OF PATRAS

DEPARTMENT OF MECHANICAL ENGINEERING & AERONAUTICS

DIVISION OF APPLIED ENGINEERING

LABORATORY OF TECHNOLOGY & STRENGTH OF MATERIALS

ΜΕΘΟΔΟΛΟΓΙΑ ΔΟΜΙΚΗΣ ΑΝΑΛΥΣΗΣ ΠΤΕΡΥΓΑΣ ΕΠΙΒΑΤΙΚΟΥ ΑΕΡΟΣΚΑΦΟΥΣ ΜΕ ΚΑΤΑΝΕΜΗΜΕΝΗ ΠΡΟΩΣΗ

Η παρούσα σπουδαστική εργασία εκπονήθηκε

από τον

ΓΙΑΝΝΕΛΟ ΒΑΣΙΛΕΙΟ

1067248

Μάρτιος, 2024

ΠΕΡΙΛΗΨΗ

Ο ταχέως αναπτυσσόμενος τεχνολογικός κόσμος έχει δημιουργήσει αυξανόμενες απαιτήσεις για τις αερομεταφορές όσον αφορά τις επιδόσεις, τη λειτουργία και, κυρίως, τις περιβαλλοντικές επιπτώσεις των αεροσκαφών. Η επιθυμία να επιτευχθεί η βιωσιμότητα των αερομεταφορών οδήγησε τη βιομηχανία να επικεντρωθεί στην εφαρμογή εναλλακτικών διαμορφώσεων, όπως τα συστήματα κατανεμημένης πρόωσης σε συνδυασμό με βιώσιμες πηγές ενέργειας. Στην παρούσα Σπουδαστική Εργασία, παρουσιάζεται η προοπτική εφαρμογής μιας διαμόρφωσης κατανεμημένης ηλεκτρικής πρόωσης που τροφοδοτείται από ένα σύστημα κυψελών υγρού υδρογόνου σε ένα μικρό, επιβατικό αεροσκάφος τύπου LSA,, συγκεκριμένα το Zodiac CH 650 B της Zenith Aircraft Company. Σκοπός είναι να παρουσιαστεί μια διεξοδική βιβλιογραφική ανασκόπηση σχετικά με την κατανεμημένη πρόωση και τις πλήρως ηλεκτρικές αερομεταφορές ενώ παράλληλα να παρουσιαστεί η μεθοδολογία μιας δομικής ανάλυσης στο Zenith Zodiac CH 650 B, που θα λάβει χώρα στα πλαίσια της Διπλωματικής Εργασίας. Η αναλυτική μέθοδος βασίζεται στην αντοχή των υλικών, στις ελαφρές κατασκευές και στην αεροδυναμική θεωρία, ενώ η μέθοδος των πεπερασμένων στοιχείων απαιτεί επίσης σχεδιασμό και μοντελοποίηση της δομής της πτέρυγας σε λογισμικό CAD και FEA αντίστοιχα. Το πλαίσιο που παρουσιάζεται στην παρούσα Σπουδαστική Εργασία μπορεί να αξιοποιηθεί και να επεκταθεί σε μελλοντικές Διπλωματικές Εργασίες.

Λέξεις Κλειδιά

Επιβατικό Αεροσκάφος, Δομική Ανάλυση Πτέρυγας, Κατανεμημένη Ηλεκτρική Πρόωση, Βιώσιμες Αερομεταφορές, Κυψέλες Υγρού Υδρογόνου

ABSTRACT

The rapidly developing technological world has created growing aviation demands regarding aircraft performance, operation and crucially; environmental impact. The urge to achieve aviation sustainability has led the industry to focus on implementing alternative configurations, such as Distributed Propulsion systems coupled with sustainable power sources. In this Student Thesis, the prospect of implementing a Distributed Electric Propulsion configuration powered by a liquid Hydrogen Fuel-Cell system on a small, commercial Light Sport Aircraft, specifically the Zodiac CH 650 B produced by Zenith Aircraft Company, is presented. The purpose is to present a thorough literature review regarding Distributed Propulsion and Electric Aviation while also providing the methodology of a structural analysis on the Zenith Zodiac CH 650 B, to be performed in the Diploma Thesis. The analytical method relies on strength of materials, lightweight structures and aerodynamic theory while the finite element method also requires designing and modeling the wing structure in CAD and FEA software respectively. The framework presented in this Student Thesis can be utilized and expanded in future Diploma Theses.

Keywords

Commercial Aircraft, Wing Structural Analysis, Distributed Electric Propulsion, Sustainable Aviation, Liquid Hydrogen Fuel-Cell

LIST OF TABLES

LIST OF FIGURES

ABBREVIATIONS

DP	Distributed Propulsion
DEP	Distributed Electric Propulsion
TeDP	Turboelectric Distributed Propulsion
ICE	Internal Combustion Engine
STOL	Short Take-Off Landing
VTOL	Vertical Take-Off Landing
MTOW	Maximum Take-Off Weight
OWE	Empty Operating Weight
PAY	Payload
HWB	Hybrid Wing Body
BWB	Blended Wing Body
NZE	Near-Zero Emissions
AEA	All-Electric Aircraft
MEA	More-Electric Aircraft
AR	Aspect Ratio
TR	Taper Ratio
v_0	Freestream Velocity
v_i	Propeller-Induced Velocity
L	Lift
D	Drag
PM	Pitching Moment
C_L	Lift Coefficient
C_D	Drag Coefficient
L/D	Lift/Drag Ratio
C_M	Pitching Moment Coefficient

AoA	Angle of Attack
Re	Reynolds Number
T	Thrust
σ	Normal Stress
q	Shear Flow
τ	Shear Stress
ε	Strain
Q	Shear Force
M	Bending Moment
M_T	Torsion Moment
c	Chord
F	Cross-Section
A	Surface Area
I_{axis}	Second Moment of Inertia
S_{axis}	First Moment of Inertia

CONTENTS - INDEX

1.0 INTRODUCTION

1.1 DISTRIBUTED PROPULSION DEFINITION

Distributed Propulsion in aircraft application is the spanwise distribution of the propulsive thrust system such that overall vehicle benefits in terms of aerodynamics, propulsive, structural and/or other efficiencies are mutually maximized to enhance the vehicle mission [2].

The concept of Distributed Propulsion is based on dividing up the thrust for the beneficiary gain of noise reduction, shorter take-off and landing, enhanced specific fuel consumption and flight range [1].

2.0 LITERATURE REVIEW

2.1 TYPES OF DISTRIBUTED PROPULSION

A number of fixed wing aircraft using Distributed Propulsion have been proposed and flown before. These configurations can also be categorized based on the overall concept, type of propulsion system and/or the energy source. For example, we have:

- **Multiple Discrete Engines:** Various types of aircraft using multiple propulsors have been proposed and flown. For these aircraft, propulsors such as propellers, turbojets, or turbofans are mounted in front of the wing, at the back of wing, or within the thick section of wing.
- **Distributed Multi-Fans driven by few Engine Cores:** Distributed propulsion employing multiple propulsors driven by a few fuel-efficient engine cores has been studied and is being pursued under NASA's SFW N+3 project (presented in Chapter 2.4, Sustainability in Aviation). Under this category, three types of propulsion system are identified and described below.
    1. *Gas-driven Multi-Fans:*
       Multi-Fans operation actuated via hot exhaust gases from a number of Gas Generators.
    2. *Gear-driven Multi-Fans:*
       Multi-Fans powered by an engine core and transferred via Gear mechanism.
    3. *Electrically-driven Multi-Fans:*
       The electricity is provided to the Multi-Fans via power lines, utilizing Battery, Fuel-Cell, hybrid Turboelectric (TeDP) systems etc.
- **Jet Flaps:** A concept where a high-velocity thin jet sheet emanates from a tangential slot at or near the wing trailing edge and provides spanwise thrust for cruise and supercirculation for high lift around the whole wing section during take-off and landing.

- **Cross-Flow Fan:** The cross-flow fan (CFF), or transverse fan, is a two-dimensional spanwise propulsor that is integrated within a wing structure to distribute the thrust along the wingspan. The fan ingests the wing upper and lower surface boundary layer air and ejects the air at the wing trailing edge. In this configuration, two gas generators mounted at the wing root and the wing tip transmit the power to the CFF rotors that are placed near the wing trailing edge and connected by flex-couplings or universal joints. However, because of low performance of the fan and difficulty of installation within an aircraft wing structure, this transport concept was never put into practice.

In the broad aspect of engine configurations, one can also divide distributed vectored propulsion into three main categories [1] (while also seeing the similarities with the categorization above):

- **Distributed Engines (DEN):** Distribution of Thrust via Distribution of Engines
  (Multiple Discrete Engines)
- **Distributed Exhausts (DEX):** Distribution of Thrust via Distribution of Exhaust Gases
  (Jet Flaps, Cross-Flow Fan)
- **Common-core Multi-Fans/Propulsors (CMF/CMP):** Multiple Fans/Propellers powered by a common energy source
  (Distributed Multi-Fans driven by few Engine Cores)

An All-Electric Aircraft (AEA) concept in combination with Distributed Propulsion technology is considered, as the electric aircraft trend displays one of the environmentally friendly propulsion options for future commercial aircraft [1].

2.2 ADVANTAGES OF DISTRIBUTED PROPULSION

A Distributed Propulsion configuration can present plenty of advantages in aircraft applications, through improvement in operation, performance and environmental impact, according to various studies. Some of them are mentioned below.

- DP can result in **Fuel Consumption reduction** by ingesting the thick boundary layer flow and filling in the wake generated by the airframe with the distributed engine thrust stream.
- DP can provide **High Lift spanwise** via high-aspect-ratio trailing edge nozzles for **Thrust Vectoring** (TV) providing **powered lift**, **boundary layer control** and/or **supercirculation** around the wing, all of which enable **Short Take-Off Landing** (STOL) capabilities.
- DP can lead to better integration of the propulsion system with the airframe for **reduction in Noise** to the surrounding community through **airframe shielding**.
- DP can offer **reduction of aircraft propulsion Installation Weight** through inlet/nozzle/wing **structure integration**.
- DP can **eliminate aircraft Control Surfaces** through differential and vectoring thrust for pitch, roll and yaw moments.
- DP can offer **high production rates and easy replacement** of engines or propulsors that are small and light.
- For the Multi-Fan/Single Engine Core concept such as TeDP, the configuration provides a very **high bypass ratio**, enabling **low fuel burn**, **emissions and noise** to surrounding communities [2].

- Distributing the propulsion system using a number of small engines instead of a few large ones could **reduce the total propulsion system noise**.
- Another advantage is the **improvement in safety due to engine redundancy**. With numerous engines, an engine-out condition is not as critical to the aircraft's operation in terms of loss of available thrust and controllability.

- The **minimization of heavy concentrated weight** burden on the wing structure and **load re-distribution** provided by the engines/propulsors has the potential to alleviate passive load alleviation problems, thus resulting in a **lower Wing Weight**.
- Possible improvement in **affordability** due to the use of smaller, easily-**interchangeable engines** [3].

- DP systems can be **more efficient** than traditional centralized propulsion systems. They allow for better control of power distribution, which can lead to reduced energy losses and **increased overall system efficiency**.
- DP allows for **greater design flexibility** in terms of **aircraft layout** and configuration. It can lead to more innovative and unconventional aircraft designs.
- DEP configurations offer **local Zero-Emissions** and if combined with electricity or hydrogen produced by renewable sources, **carbon neutral** operation can be achieved. Carbon neutrality would prove that **sustainable aviation** is achievable.
- DEP Propeller systems that are powered by **Electric Motors** can significantly **reduce the noise** due to the absence of fuel-burning Turbojets/Turbofans or aircraft Internal Combustion Engines.
- DEP configurations also provide **additional power for take-off**, **reduction of runway length** and **propeller drag force** and finally **skid avoidance during the landing phase**.
- For a given wing surface area and conditions (density, freestream velocity and angle of attack), a DEP configuration provides a **significant increase in Lift production**. Therefore, either the surface area can be reduced, resulting in **friction drag reduction**, or the increased lift can be utilized for **STOL capabilities**.

The increase of Lift during Take-Off and Landing and the resulting STOL capabilities and Runway Length reduction is a crucial advantage in aircraft performance and will be investigated more thoroughly in Chapter 4.1.2, where the propeller-air interaction and the Slipstream effect are studied.

2.3 DISADVANTAGES OF DISTRIBUTED PROPULSION

Distributed Propulsion can present important advantages albeit without ignoring potential disadvantages. Some of them are mentioned below.

- Usually, DP configurations result in **weight penalties**, due to the need for additional components, such as multiple engines, motors, batteries, hydrogen tanks etc. Such weight penalties might reduce the passenger capacity or the payload.
- Big Turbojets/Turbofans Engines achieve high **thermal efficiency** (partly due to higher bypass ratios), whereas smaller such engines significantly lack this kind of efficiency.
- The added **complexity** and components of DP systems can lead to **higher manufacturing and maintenance costs**. DEP systems, in particular, may have higher initial costs due to the expense of Electric Motors, Inverters, Batteries and Fuel-Cells.
- Another challenge of DP configurations is the **thermal management**. Managing heat generated by multiple propulsion units in a distributed system can be challenging. Efficient thermal management is crucial to prevent overheating and ensure safe operation.
- **Technology** that could prove vital to DP application is **not adequately advanced**, such as the superconductors/superconducting materials that are required in TeDP configurations to improve drastically the system efficiency.
- DP configurations may present **challenges in integrating** multiple propulsion units into the aircraft's design, requiring careful consideration of aerodynamics, structural integrity, and thermal management.

2.4 SUSTAINABILITY IN AVIATION

Concerns about the environment and the energy usage, along with the constant increase of air passengers, have resulted in increased aviation demands and led the aerospace and the engineering sector to explore alternative solutions in materials, propulsion systems etc. in order to achieve technological innovation and sustainability in aviation.

The needs for aviation sustainability currently motivate the identification of propulsion systems solutions that address some of the published goals for future aviation. These visions primarily target reduction of fuel consumption, aircraft emissions, aircraft noise and may also stress the minimization of the industrial impact on the global on the global environment [1].

In response to the growing aviation demands and concerns about the environment and energy usage, **NASA's Subsonic Fixed Wing program** (SFW) focuses on 4 'corners' of the technical trade spaces for future aircraft design: fuel burn, emissions, noise, field length. Created in 2010, NASA set three timeframes of accomplishments, named N+1 (2015), N+2 (2020), N+3 (2025) respectively. Although it may not be feasible to meet all the goals for each time frame, the multi-objective studies attempt to identify possible vehicle concepts that have the best potential to meet the combined goals. In order to meet NASA's N+3 goals, drastic changes in propulsion and airframe systems are required and proposed. One such proposed concept is based on a distributed propulsion system using advanced electric power generation and transfer of power to remotely located distributed electric fans [2].

European Union's **FlightPath2050** goals have already been set and agreed by the aviation partners. Among them, one set goal is protecting the environment and the energy supply (75% reduction in CO2 emission per passenger kilometer, 90% reduction in NOx emissions, 65% reduction in noise emission and emission-free aircraft movement when taxiing) [4].

CORNERS OF THE TRADE SPACE	N+1 (2015)*** Technology Benefits Relative to a Single Aisle Reference Configuration	N+2 (2020)*** Technology Benefits Relative to a Large Twin Aisle Reference Configuration	N+3 (2025)*** Technology Benefits
Noise (cum below Stage 4)	- 32 dB	- 42 dB	- 71 dB
LTO NOx Emissions (below CAEP 6)	-60%	-75%	better than -75%
Performance: Aircraft Fuel Burn	-33%**	-50%**	better than -70%
Performance: Field Length	-33%	-50%	exploit metroplex* concepts

*** Technology Readiness Level for key technologies = 4-6
** Additional gains may be possible through operational improvements
* Concepts that enable optimal use of runways at multiple airports within the metropolitan areas

Εικόνα 1: NASA's Future Aviation Goals

2.5 THE ELECTRIC AIRCRAFT

Tracing the evolution of the electric aircraft is interesting from both a historical point of view and for future considerations of civil aviation, especially taking into account the rising aviation demands in terms of sustainability.

One of the distinct characteristics of the electric aircraft is that it employs electric motors instead of internal combustion engines. For this purpose, the electricity can be supplied to the electric motors using different methods. In the past, fuel cells, batteries, solar cells, ultra capacitors and other means have been considered for this purpose.

The electric aircraft can broadly be divided into two main categories: the All-Electric Aircraft (AEA) and the More-Electric Aircraft (MEA). A deeper understanding of the Primary Power Systems (PPS) referring to the main propulsion power, and Secondary Power Systems (SPS) referring to the distributed power around the airframe and the engine systems can cast light on the AEA and MEA concepts.

Many complexities with electric aircraft propulsion have played a noteworthy role in the evolution of the AEA. Restrictions in a given technology have further motivated the exploration of alternative systems to be used in the electric aircraft. An important example for this is the introduction of Fuel-Cells in aeronautics. Early Fuel-Cells were associated with other technical objectives rather than used as electrochemical devices to produce electricity. Fuel-Cells provided an alternative technology for the electric aircraft. As knowledge, research and technology have significantly advanced, Fuel-Cells are now a serious proposal in AEA applications and could be the answer to sustainability demands as explained further in this Thesis.

Electric aircraft propulsion system topologies are presented below. While all or most topologies will be covered in this Thesis, focus will be mainly given to the All-Electric topologies due to the sustainable aviation demands in the industry. The electric aircraft propulsion topology chosen to implement in the Zenith Zodiac CH 650 B is the Fuel Cell based one, with only Fuel Cell powered electric propulsors.

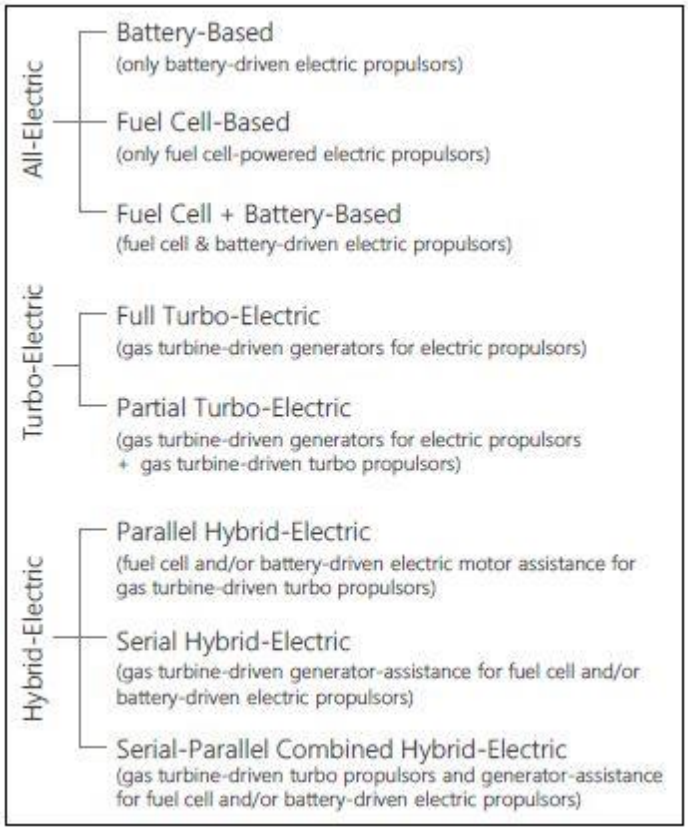

Εικόνα 2: Electric Aircraft Propulsion Architectures

2.6 HISTORICAL REVIEW

The idea of Distributed Propulsion and All-Electric Aircraft concepts in aviation is not a matter of the last few decades. A brief Historical Review of the respective milestones is presented below.

2.6.1 Conceptual Milestones of Aircraft Distributed Propulsion

In 1924, Manzel proposed multiple propeller units arranged in rows or series as the propelling mechanism for airships, aircrafts etc. The motivation behind this concept was the feasibility of ascent without a special landing field.

In 1932, Altieri's invention was based on using auxiliary propellers fore and aft of the aircraft wings. Recognizing the small effect of supplemental propulsion assistance, using additional propellers, this concept was primarily aimed for proper and safe landings.

In 1954, Griffith replaced the earlier propositions of propellers with gas turbines and presented the concept of an aircraft with a master combustion engine unit in combination with a number of gas turbine 'slave' units that were spaced in the spanwise direction of the aircraft wing structure, providing the means for Thrust Vectoring (TV), Short Take-Off and Landing (STOL) and low fuel consumption. This invention combined many new technical features of significant potential [1].

In the late 1960's, a Vertical/Short Take-off and Landing (V/STOL) air-deflection and modulation (ADAM III) fighter concept was studied for various missions, utilizing a Distributed Propulsion system with Gas-driven Multi-Fans. The design never went into production possibly because of the problem of ducting hot gas through the wing structure. In this concept, the gas generators and their inlets were installed near the fuselage to provide hot gas to the wing mounted turbines that drove high-bypass-ratio turbofans. The turbofans and turbines were co-located in the wing section away from the gas generators. The hot gases from the gas generators were routed through long ducts across the wingspan to the location where the turbines and fans were installed. The inlets and nozzles for the turbofans and turbines were also all within the wing structure away from the gas generators and provided distributed thrust to the vehicle.

Then in the 1970's, a Gas-driven Multi-Fan transport aircraft was conceived, and a model was tested for STOL operation. It was based on a conventional 'tube and wing' airframe configuration with 16 tip-driven fans spread along the top surface near the wing trailing edge. The tip-driven fans with fan pressure ratio of 1.25 were powered by high-pressure discharge air from the low-pressure compressor stages and mounted on a hinged flap to achieve high lift via supercirculation. In addition, the massive suction effect in front of inlets created additional lift on the airframe and delayed flow separation on the wing upper surface [2].

In 1974, pursuing another research front, Malvestuto Jr. took interest in an aircraft capable of carrying substantial payloads. Using a wing structure, divided into several wing portions equipped with rotors together with rotors in arrangement with lighter-than-air buoyancy units, this rotor-wing combination distributed the power over a much larger effective area to achieve considerably higher power loadings, in comparison to a conventional power loading of a helicopter. As a result, distributed propulsion was also considered and introduced for Vertical Take-Off and Landing (VTOL) aircraft. One could argue that this concept brought Manzel's 1924 concept to a new level, using a wealth of knowledge that was gained over almost 60 years.

In 1983, a concept for a solar powered aircraft with a cruciform wing structure was proposed. Equipped with solar cells and multiple propellers positioned on the wingtips, details were provided on how to maintain surfaces normal to the sun's rays to utilize the direct solar energy. This concept, amongst others, served as a crucial step towards the development of solar airplanes, such as the first generation High-Altitude Long Endurance (HALE) vehicle, Pathfinder.

In 1988, NASA proposed a number of derailed concepts for airframe and propulsion interactions and integrations. A commonality between these concepts is the employment of different propulsion systems.

SnAPII featured twin fuselages separated by a circulation-control wing that contributed to high lift coefficients during takeoff and landing. Using two tail-mounted engines at the end of each fuselage with Thrust Vectoring (TV) and reversing, fuselage Boundary Layer Ingestion (BLI) and smart inlet and nozzle technology, SnAPII also used a device to power flow control on the outer portions of the wing. Wing tip turbines could further reduce the wake hazard at takeoff and landing. This concept merged two individual fuselages with their propulsive units into one main body.

A hypothetical scenario of total engine failure for either one of the combined fuselages was simplified in the subsequent proposal for a Distributed Engines (DEN) regional STOL aircraft.

This airplane made use of an array of wing-integrated mini-engines to provide lift augmentation and distribution with increased redundancy. Employing another array of mini-engines at the tail, integrated with inlet and nozzle, deflectors enabled the Coanda effect for TV.

Using a similar circulation-control wing similar to SnAPII, a blended forward swept wing body concept was envisioned. This aircraft used three aft-mounted high-bypass ratio turbofans with BLI, TV and reversing, smart inlet, nozzle technology and flow control systems.

The Trans-Oceanic Air-Train was characterized by two vehicles, the Lead and the Mule. These vehicles rendezvous to complete the cruise configuration of a long-range transport of cargo. Although the design was aimed at freight flight in the low transonic regime, in favor of high aspect ratio wings and span loading for minimal fuel consumption, parts of this concept could potentially also be applied to commercial aviation. Equipped with TV-technology for optimal takeoff performance, the Lead vehicle was designated as the primary fuel carrier and responsible for flight control activities of all Mule vehicles [1].

A Gear-driven Distributed Propulsion concept employing a dual fan driven by one engine core on a HWB airframe was recently studied by NASA . The study was to determine the effects of a dual-fan engine configuration on the vehicle-level performance (i.e., range) of a representative subsonic transport and to develop a preliminary understanding of the challenges associated with the implementation of distributed propulsion schemes. The mentioned study shows one such concept where an engine core drives two large-diameter fans via gears and shafts, providing a very high bypass ratio. In this configuration, the core engine is outside the airframe boundary layer flow with almost 100% inlet total pressure recovery, and the dual fan ingests full boundary layer flow approaching the inlet cowl lip.

For the Silent Aircraft Initiative, the Cambridge-MIT Institute developed the SAX-40 conceptual HWB aircraft using a similar Gear-driven Multi-Fan propulsion concept. The purpose of this study was to design an aircraft with noise being the primary design variable addressed, such that the noise would be contained within the perimeter of an urban airport. This aircraft employs three engine nacelles where each nacelle houses three fans that are connected to a single engine core through gears and shafts. Similar to NASA’s study, this propulsion concept also has a very high bypass ratio and low engine noise. Also, it features inlets with a high amount of airframe upper surface boundary layer ingestion.

Recently, a cruise-efficient STOL (CESTOL) aircraft was proposed based on a high subsonic HWB or BWB transport configuration because of its high cruise efficiency, low noise characteristics, and a large internal volume for integrating embedded distributed propulsion system. The propulsion system employed 12 small conventional engines partially embedded within the wing structure and mounted along the wing upper surface near the trailing edge to enable STOL operation using low-pressure-fan diverted-bypass air. The vehicle concept uses distributed propulsion for quiet powered lift using an internally blown flap, with substantial engine noise shielding effect by the airframe, rapid climb out, and steep descent approach to provide a very low noise footprint on the ground. These characteristics of the aircraft may enable 24-hour use of the underutilized regional and city-center airports to increase the capacity of the overall airspace while still maintaining efficient high subsonic cruise flight capability.

To improve performance and to reduce environmental impacts even further, a drastic change in the power transmission of distributed propulsion system for large transport aircraft was proposed and studied on HWB as well as tube and wing airframes. Thus, the N3-X Vehicle was conceived by NASA. Using a new concept called “Turboelectric Distributed Propulsion (TeDP)”, one of the vehicles adopts the mentioned above 12-engine CESTOL-HWB airframe but employs two (2) remotely located gas turbine-driven superconducting generators to drive 14 distributed fans instead of using many small conventional engines. This arrangement allows the use of many small partially embedded fans while retaining the superior efficiency of large core engines, which are physically separated but connected to the fans through electric power lines. The airframe is derived from Boeing’s N2A HWB configuration with similar mission characteristics of a 6,000-nmi | 11,112-km range, a 103,000-lb | 46,720-kg payload capacity, and the ability to fly at the aerodynamic design point (ADP) of Mach 0.8 at 31,000 ft | 9445 m altitude. The propulsion system utilizes superconducting electrically driven, distributed low-pressure-ratio (1.35) fans with power provided by two remote superconducting electric generators based on a conventional turbofan core engine design. The use of electrical power transmission allows a high degree of flexibility in positioning the turbogenerators and propulsor modules to best advantage. In the aircraft configuration examined the turbogenerators were located at the wing tips where the turbogenerator would experience undisturbed free-stream conditions, while the fan modules were positioned in a continuous fan nacelle across the rear fuselage where they ingest the thick boundary-layer flow,

fill the wake of aircraft with fan discharge air, and thereby reduce the thrust required by the vehicle. This concept is one of the several concepts pursued by NASA to meet N+3 goals.

As a part of NASA's Small Business Innovative Research (SBIR) phase 1 contract study, Empirical Systems Aerospace, LLC, conducted a system study of integrating an advanced cryogenic electric propulsion system onto a 150-passenger STOL regional airliner, the ECO-150, and a larger 250-passenger large transport, the ECO-250. A key feature of these two concepts, is the integration of the superconducting-electric motor-driven fans with the wing such that the inboard wing is separated into top and bottom sections, and all electric-driven propulsors are completely embedded within the airfoil or wing structure. This feature provides a benefit of wing weight reduction through wing bending moment relief because the distributed electric fans and the use of the common nacelle as wing rib structure provide stress relief to the wing structure. In addition, a favorable aerodynamic advantage exists such that at low speed, thrust vectoring of a two-dimensional low temperature nozzle may provide supercirculation of airflow around the airfoil for a large improvement in lift coefficient. Another key feature of the concepts is the use of liquid hydrogen both as a cooling fluid for the superconducting system and as fuel for the turboelectric generator engine. Although the study was very preliminary in nature, these propulsion system features along with the vehicle configuration itself did certainly point toward large reduction in fuel burn for both ECO-150 and ECO-250 configurations.

Another TeDP vehicle concept named "H3.1" was recently proposed and studied by MIT as a part of NASA's SFW N+3 cooperative work. The vehicle is based on the HWB configuration with a range of 7,600 nmi (14,075 km), 354 passengers, and cruise Mach 0.8 at 35,000 ft (10,668 m) altitude. Similar to NASA's N3-X vehicle, this vehicle also ingests upper airframe surface boundary-layer flow to improve propulsive and hence the fuel efficiency while minimizing noise impact to the surrounding community by shielding the propulsion-related noise with the airframe. Another key feature of this configuration is the use of cryogenic methane as fuel because of its higher specific energy, which improve the fuel efficiency of the aircraft. In addition, the cryogenic fuel allows the use of superconducting materials to distribute the electric power from three turboelectric generators to 23 electric fans that are semi-embedded in the upper surface of the airframe [2].

Depiction	Aircraft	Year
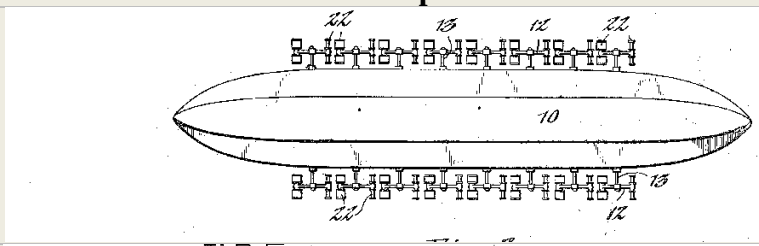	Manzel's Propeller-Array Airship Concept	1924
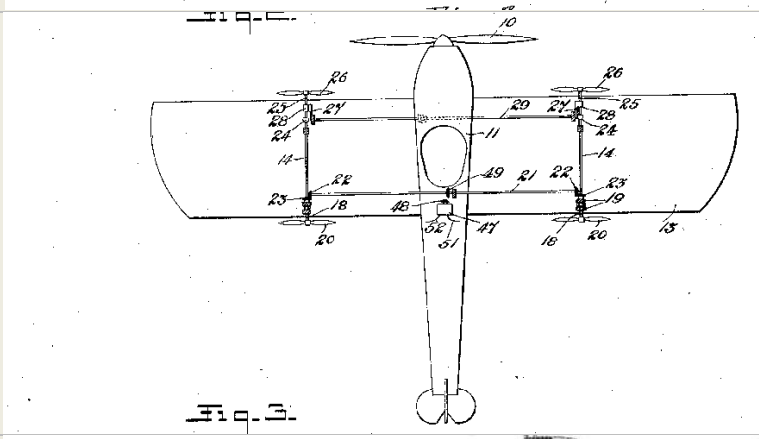	Altieri's 5-Propeller Concept	1932
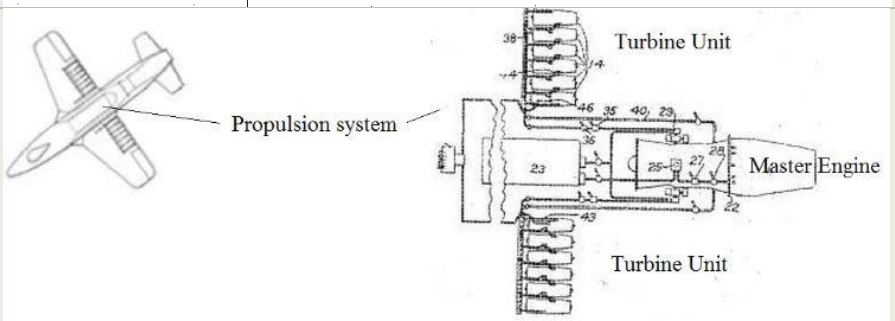	Griffith's Concept	1954
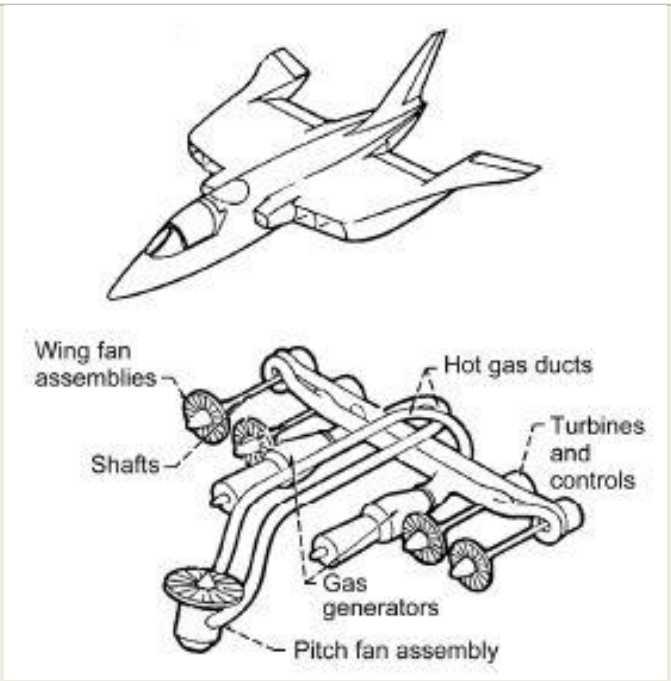	ADAM III Gas-Driven Multi-Fans Fighter Plane Concept	1960s

	Gas-Driven Multi-Fans STOL Transport Concept	1970s
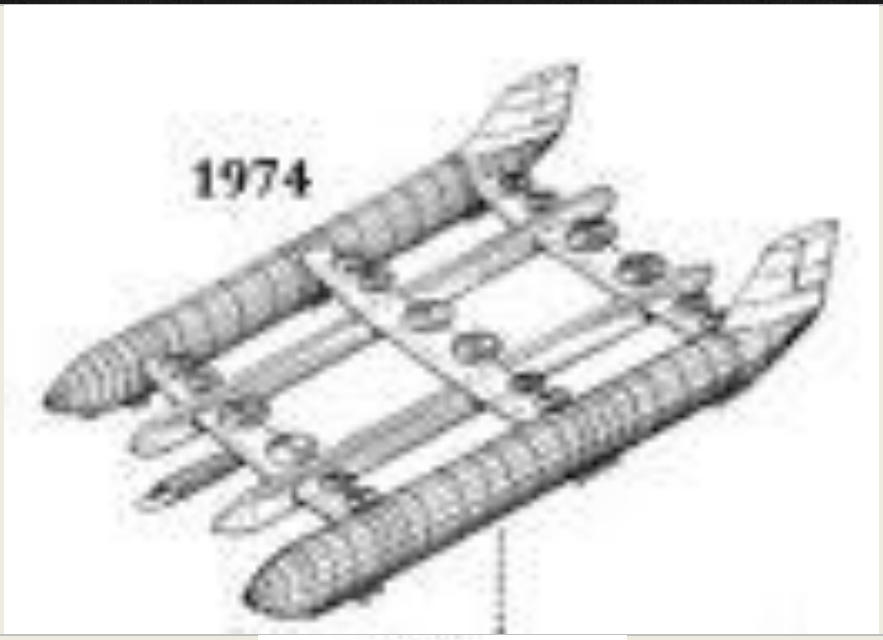	Malvestuto Jr.'s VTOL Aircraft Concept	1974
	Cruciform Solar-powered Aircraft Concept	1983

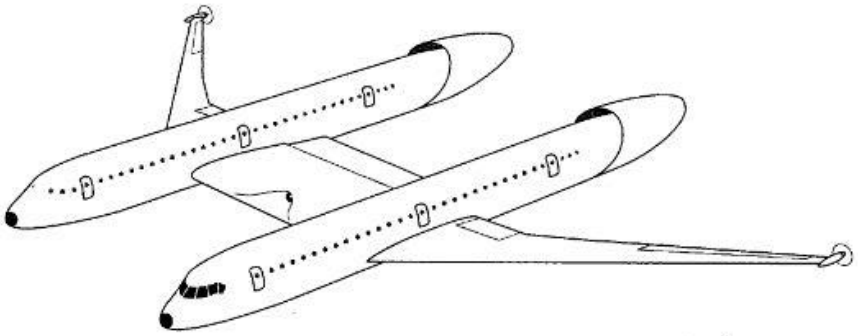	NASA's SnAPII Twin-Fuselage Wingtip Turbines Concept	1988
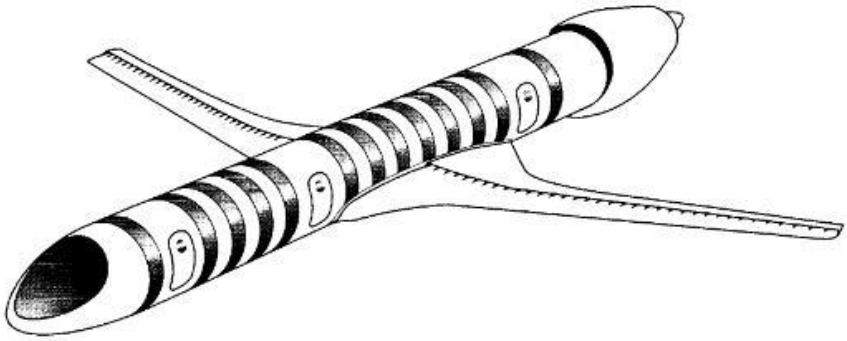	NASA's Distributed Engine Regional STOL Concept	1988
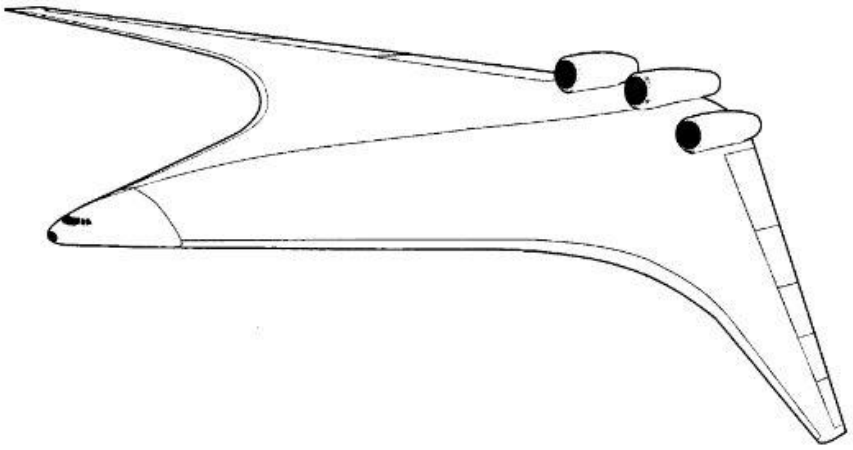	NASA's Forward Swept BWB Concept	1988
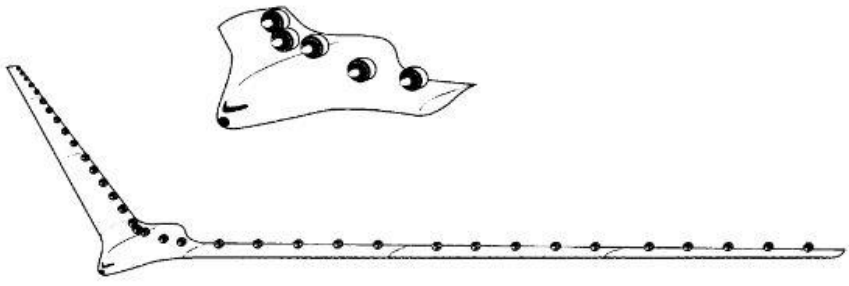	Trans-Oceanic Air-Train Concept	1988

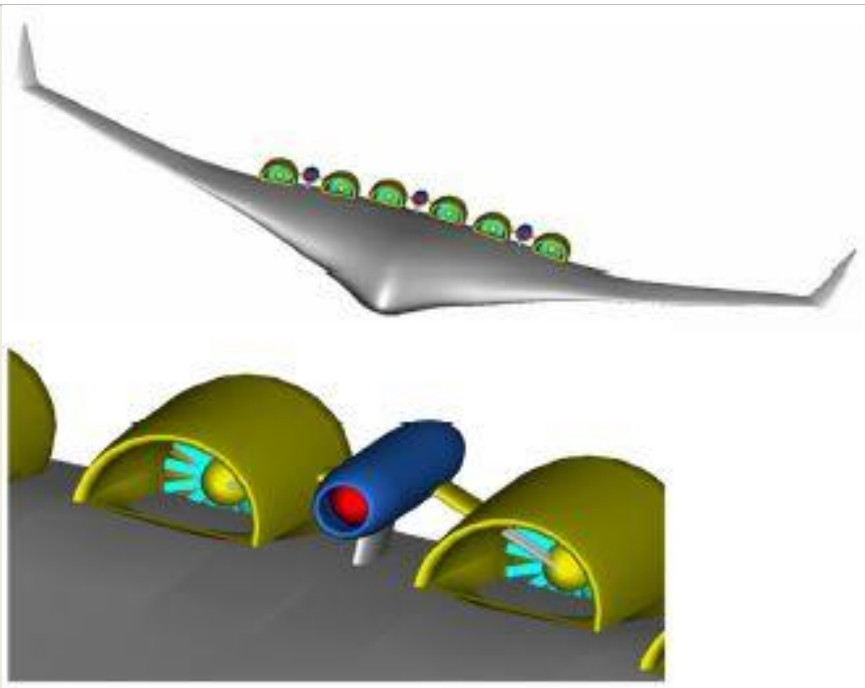	Gear-Driven Dual Fan, Single Core HWB Concept	Present Day
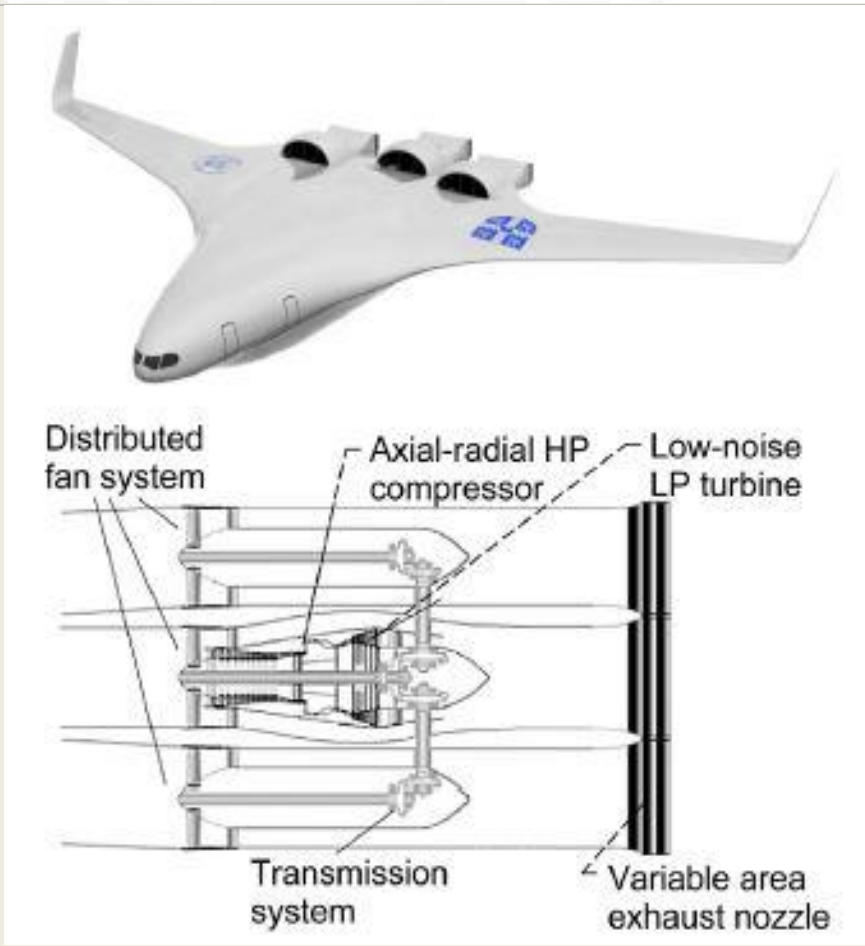	Cambridge & NASA's Gear-Driven Multi-Fans SAX-40 Concept	Present Day

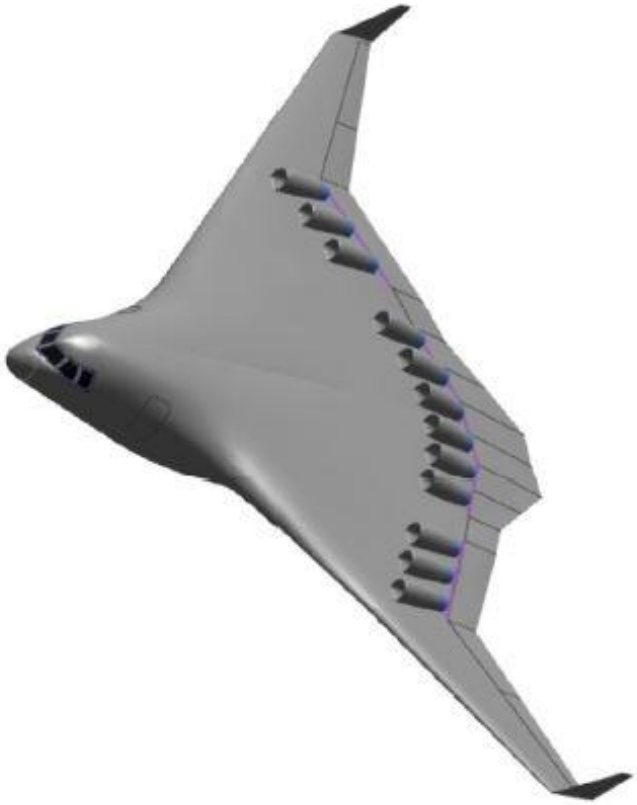	NASA's CESTOL Concept	Present Day
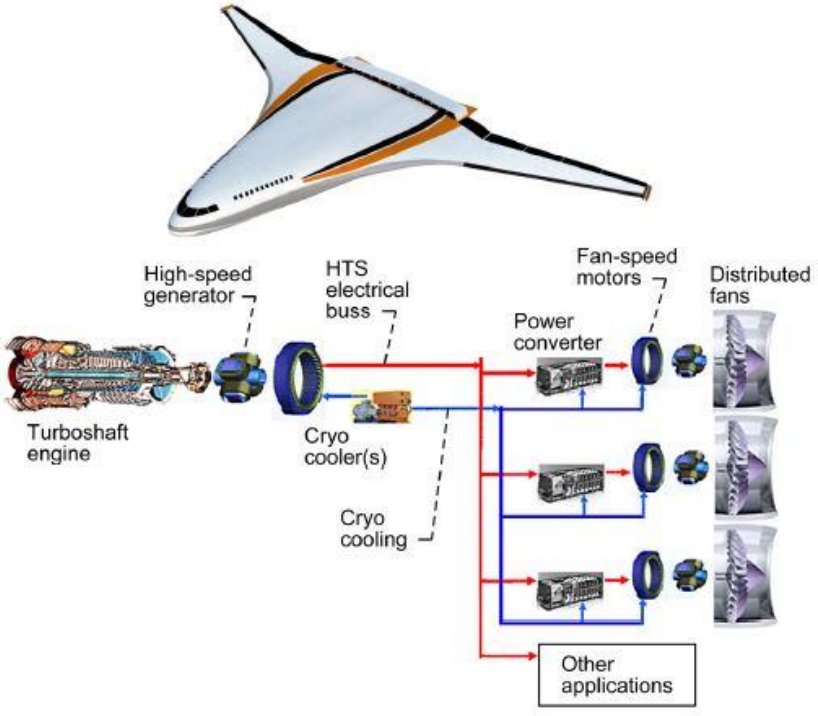	NASA's TeDP N3-X Concept	Present Day

	 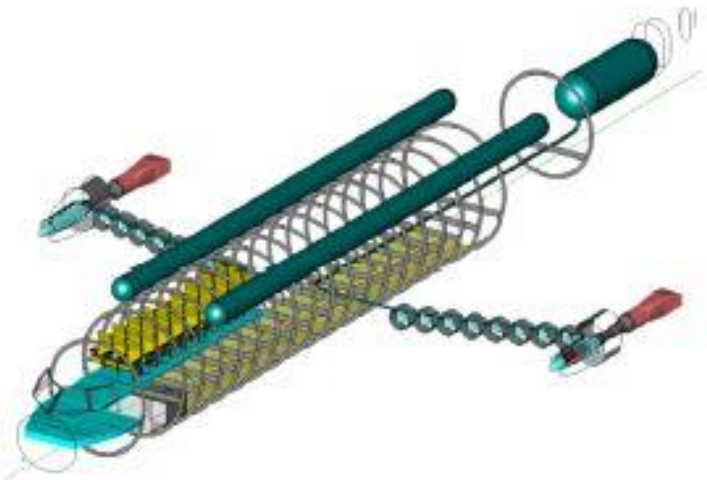	Empirical Systems Aerospace TeDP ECO-150 Concept	Present Day
		NASA & MIT's TeDP H3.1 Concept	Present Day

Πίνακας 1: Conceptual Milestones of Aircraft Distributed Propulsion

2.6.2 Actual Milestones of Aircraft Distributed Propulsion

For the purpose of elucidating ideas that became reality, a short visit is made along the historical axis of time, to point out some aircraft that implemented three or more units of propulsion and were chosen for commercial, experimental, cargo, research and military applications. Unlike the early days of conceptual aviation where distributed propulsion was introduced in the airship industry, many promising proposals that would have progressed into production were never funded. One possible cause for this, at least in the latter part of the 20th century, emerged from the misconception that hydrogen was the primary cause of the Hindenburg catastrophe. Doubtlessly, the term “Hindenburg syndrome” had a negative influence on the general public and the airship industry, but regardless of this significant impact, the aviation industry embraced many different designs featuring distributed propulsion [1]. Here are some actual milestones of Aircraft Distributed Propulsion:

In 1929, Dornier Do X, the world’s largest aircraft at the time, flew for the first time. Intended for transatlantic flights, this aircraft left Friedrichshafen, Germany, on 2 November 1930 with 17 passengers and crew for the USA. It was equipped with faired-in engine supports for its 12 engines. Early long-range flight attempts with Distributed Propulsion revealed many unforeseen parameters that could not be efficiently addressed or investigated during the conceptual design phase. Engine cooling was one of these problems. Using multiple engines without any cooling measures caused a thrust reduction for the rear engines.

The same year the Dornier Do X aircraft left Friedrichshafen, Handley Page H.P.42 made its first flight. Intended for the purpose of linking various parts of the British Empire, this aircraft used two engines on each of the large unequal-span biplanes, leaving a brilliant record of safety with no fatal accidents after a decade of service. An innovative part of H.P.42’s design was to position the propulsion units on different wings.

Seemingly a successful trend for long-range missions, multiple engine solutions were chosen more often, and this involved also two historical flying boats. The first aircraft, Blohm und Voss BV222 Wiking, the largest operational flying-boat during World War II, was specifically designed for long-range passenger transport in the late 1930s and was equipped with six vertically opposed engines distributed over the wing.

Following this success, a historical flight was made by Howard Hughes' famous H-4 Hercules in 1947. H-4 Hercules was the largest flying boat ever built and consisted of a single hull and eight radial engines. Taking into consideration the significant size of the aircraft, a substitution of wood for metal served as a new gateway for non-conventional approaches to aircraft design The design practices of this aircraft revealed, however, many technical difficulties ranging from the integration of power systems to large control surfaces. These problems added a new dimension to the earlier observed difficulties with engine cooling procedures in aircraft DP [1].

The DP configuration of Multiple Discrete Engines was implemented on the 1940's flying wing Northprop YB-49. It had four linearly arranged conventional turbojet engines in each side of wing with subsonic rectangular inlets at the leading edge and conventional circular nozzles at the trailing edge of the wing.

An aircraft utilizing the DP concept of Jet Flaps (DEX) was the Hunting H.126 aircraft, that was built and flown in the 1960's at lift coefficient C_L = 7.5 and maximum operationally usable C_L = 5.5. To enable such high lift, the engine diverted almost 60% of its thrust across its wing trailing edge to achieve very high lift capability. Its first flight was completed in 1963 [2].

The Bell D-2127 aircraft (X-22) took the concept of distributed propulsion one step further with its tilting arrangement of ducted fans. 1966 was the first time this aircraft took to the skies and almost two decades later it had contributed significantly to the VTOL/STOL research through programs at NASA and Federal Aviation Administration (FAA).

1969 was the year when the Boeing 747 aircraft, perhaps one of the most commonly known historical airplanes in commercial aviation, had its first flight. The Boeing 747 used four turbofan engines in pods pylon-mounted on wing leadings edges. Equipped with air-cooled generators mounted on each wing for electrical supply, two additional generators could provide primary electrical power when the engine-mounted generators were not operational. Technological advancement and the Boeing 747's efficient propulsion system integration were evident in a blunt comparison to the Dornier Do X's engine mishaps. The engine arrangement on the Boeing 747 has become a standard configuration for many commercial aircraft.

The Antonov An-225 MRIYA was an aircraft which was not designed to transport air travelers, but rather to transport the Soviet space shuttle. In 1989, Antonov An-225 completed this task with its six engines fitted with thrust reversers and glass fiber engine cowlings.

Nine years later, two DP systems were combined in a propulsion scheme with virtually no harmful emissions. Centurion, an unmanned solar-powered aircraft, first flown in 1997, with 61.8 meters wingspan and 14 brushless direct-electric motors, could reach altitudes of 30km. Envisioned as the 'Eternal Airplane' with the objective to fly for months, solar arrays were used to power electrical motors. The environmental impact of this aircraft has contributed to considerations for more environmentally friendly propulsion systems [1].

Depiction	Aircraft	Year
	Dornier Do X	1929
	Handley Page H.P.42	1929
	Blohm und Voss BV222 Wiking	1930s

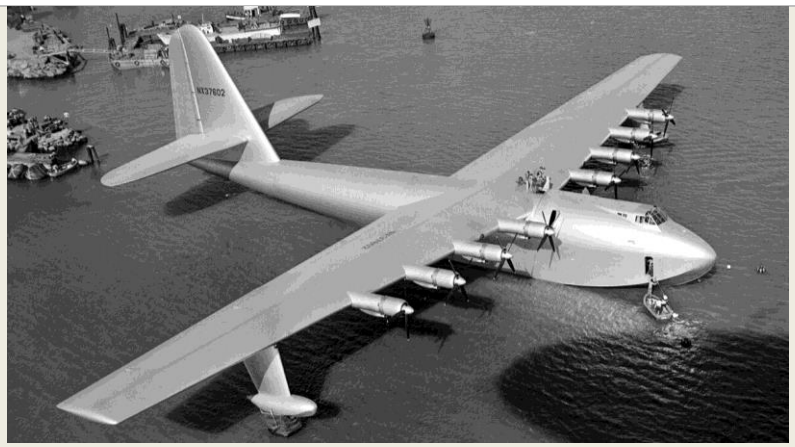	Howard Hughes H-4 Hercules	1947
	Northprop YB-49	1949
	Hunting H.126	1962

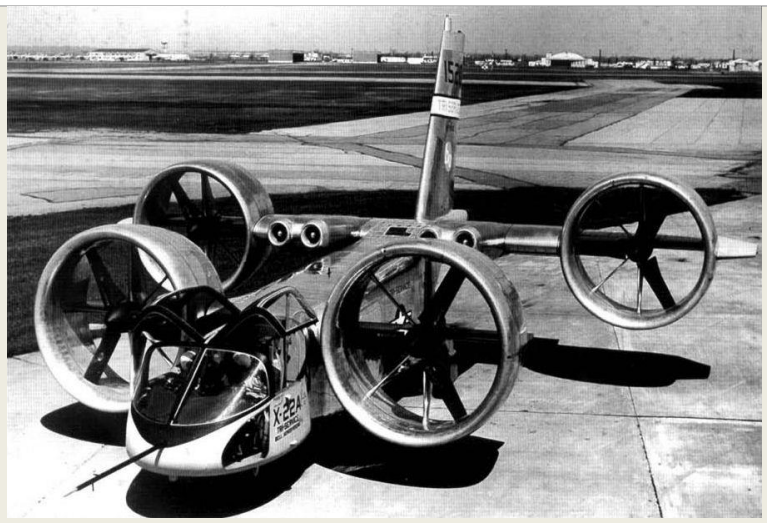	Bell D-2127	1966
	Boeing 747	1969
	Antonov Ant-225 MRIYA	1989
	NASA's Centurion	1997

Πίνακας 2: Actual Milestones of Aircraft Distributed Propulsion

2.6.3 Milestones of the All-Electric Aircraft

Since we are investigating alternative aircraft solutions that will satisfy the growing aviation and sustainability demands and one of those solutions is the electric propulsion, here are some actual milestones of the All-Electric Aircraft:

Early days of the electric aircraft included a minimal electric part, which primarily consisted of the electrical power dependency for ignition purposes for the very first powered flights in 1903. Growing dependency on electrical power was soon evident with more electrical subsystems, for example radio communication.

In 1943, Kilgore proposed the electrical airplane propulsion system shown below to drive multiple rotating propellers. Equipped with one or a small number of poly-phase synchronous generators in the speed range of 10,000 RPM to 20,000 RPM, a pole-number range of 4 and 8, and a number of propeller-driving poly-phase motors energized from the generators, this power plant arrangement revealed a number of advantages. Additional power for take-off, reduction of runway length and propeller drag force, skid avoidance during the landing phase, wheel brakes, reduction of detachable conductors, elimination of sparks using induction-motors to drive the motors, and minimization of heavy concentrated weight burden on the wing structure, were some of the significant benefits of this concept.

In 1974, an electro-motorically driven aircraft was suggested by Meier. This configuration employed fuel cells or batteries for driving the propellers. The perennial drawback of the weight-to-power ratio, along with the excessive weights of fuel cells and batteries, constantly motivated researchers to restrict the usage of electric aircraft to unmanned, low speed aircraft with high aspect ratios wings. Many of these concepts employed a distributed propulsion arrangement. Even though substantial efforts were made to increase the power-to-weight ratios, many of the goals in favor of the electric aircraft could not be achieved. Suggestions made by the team of Meier, and other scientists around the world, considered a variety of possibilities for the electric aircraft. A true display of the electric aircraft technology came to reality through the solar-powered research programs initiated by NASA and AeroVironment, Inc., in the beginning of the 1970s. Similar research endeavors were also pursued around the globe by other scientists and research teams. The

highlighted research programs at NASA represent a small portion of the technologies involved with the electric aircraft, and thus a few milestones of this specific era will be revisited.

The concept of the Sunrise I airplane was born in the early 1970s and this aircraft made its first flight on November 4, 1974, as the world's first solar-powered airplane. Although the usage of solar power limited the aircraft today flight and cloud avoidance, it served as a proof-of-concept to develop electric-powered fixed-wing aircraft. Even though Sunrise did not attain extended solar flights, it was able to provide the tools for an improved version of solar- powered aircraft, called the Sunrise II.

Sunrise II displayed even more potential to reach high altitudes and could benefit from improved aerodynamics. In 1980, Gossamer Penguin used the removed solar panels from Sunrise II for its initial flights. The aircraft had a 71-foot wingspan and used 3920 solar cells to produce 541 Watts of power. After flight tests with solar cells, batteries and an electric motor, it was proven that electric aircraft could also be manned.

The first official manned flight of direct solar power was completed on 7 April 1980, and this concept was evolved into Solar Challenger that had a 46.5-foot wingspan and accommodated 16128 solar cells. Solar Challenger was designed to with stand normal turbulence levels and was equipped with batteries, solar cells, an electric motor and a propeller. In late 1980, the initial flights were moved from California to Marana Airpark, northwest of Tucson, Arizona. By that time the aircraft had already moved from flights using batteries to solar-powered flights. Solar Challenger was able to complete a manned flight from Paris to London on 7 July 1981 in an attempt to show the feasibility of the aircraft's efficiency.

The same year Solar Challenger took to the skies, the classified program High Altitude SOLar Energy (HALSOL) was launched by the U.S. Government to explore the feasibility of solar-electric flight above 65,000 feet. About a decade later some of the findings from the HALSOL program contributed to Pathfinder, an unmanned aircraft that was able to reach a record altitude of 50500 feet for solar-powered aircraft. In 1997, Pathfinder was eventually transferred to Hawaii, due to the high levels of sunlight available in that location. Pathfinder was able to reach a world altitude record of 71530 feet for solar-powered and propeller-driven aircraft.

Moreover, Pathfinder was upgraded to Pathfinder Plus during 1988. This aircraft was able to reach even higher altitudes than the original Pathfinder by reaching an altitude of 80210 feet and breaking the record altitude of propeller-driven aircraft. Some notable changes made to the

Pathfinder Plus enabled it to reach higher altitudes than ever before and served as a framework for an even more improved solar aircraft called the Centurion. Increased wingspan, additional motors, and more efficient silicon solar cells provided Pathfinder Plus with an additional 5000 Watts power in comparison to the 7500 Watts power used for the Pathfinder.

An interesting observation regarding the engine power output is that the number of engines has steadily increased from the Solar Challenger to the Centurion aircraft. Centurion evolved the ideas of a solar-powered aircraft to higher levels and proved that it was possible for an aircraft to use telecommunications relay platforms and stay airborne for weeks and collect scientific sampling data and imaging data. Centurion's flexible wing made of kevlar, carbon fiber and graphite epoxy composites was divided up into five sections and had no taper or sweep. Solar cells were used to power the electric motors, communications, electronic systems and avionics. Centurion was further equipped with a backup lithium battery system that could allow additional two to five hours limited flight after dark. Extensive research progress made for the HALE aircraft category placed solar-powered aircraft concepts into practice. Many of these aircraft employed electric motors, driven by batteries and solar cells. NASA's solar-powered and electrical aircraft initiatives were only a fraction of the extensive research work, done in the direction of the electric aircraft. In many ways, the HALE aircraft are the true representatives of AEA. Further, an increasing number of electric aircraft have entered the manufacturing phase over the years.

IFB Hydrogenius stands out amongst the different electric aircraft, as this particular aircraft also uses liquid hydrogen, batteries and a fuel cell onboard. IFB Hydrogenius delivers the largest engine power through its combination of different power systems, which seems to be the most suitable option for larger MTOWs. This rather simplistic survey exhibits one of the distinguished traits of the electric aircraft which is the limited power densities for given airframe weights. Thus, a combination of different power systems is more likely to present a solution for larger engine powers and should therefore be considered in the future. NASA explored this direction through an analytical performance assessment of a fuel cell powered small electric airplane. Similarly, researchers of the ENFICA-FC project have also looked into the feasibility of powering an all-electric propulsion aircraft with fuel cells. For the sake of AEA discussions, it should be emphasized that fuel cells do not represent the only proposed complementary technology for AEA but are still considered important components in electric aircraft schemes and as possible Auxiliary Power Units (APUs) [1].

Depiction	Aircraft	Year
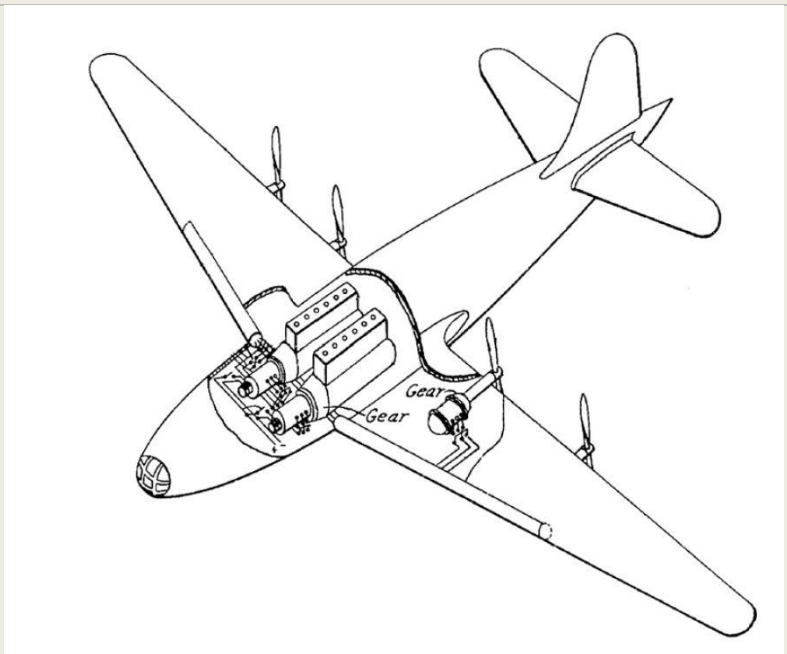	Kilgore's AEA Proposal	1943
	World's First Solar-powered Aircraft, Sunrise I	1974
	Solar-powered Aircraft, Sunrise II	1977

	Solar-powered Aircraft, Solar Challenger	1980
	NASA's Solar-powered Aircraft, Pathfinder	1987
	NASA's Solar-powered Aircraft, Pathfinder Plus	1988
	NASA's Solar-powered Aircraft, Centurion	1997
	Liquid Hydrogen Fuel-Cell AEA, IFB Hydrogenius	2011

Πίνακας 3: All-Electric Aircraft Milestones

2.6.4 Distributed Propulsion and All-Electric Aircraft ongoing Programs

After a brief Historical Review of aircraft Distributed Propulsion and Electric Aviation, it is important to mention several aerospace programs that have been initiated to design and develop airplanes that satisfy the characteristics of sustainability while employing DP and/or AEA configurations.

A state-of-the-art application of a sustainable AEA is the **HY4** aircraft by H2FLY. H2FLY was founded by five engineers from the University of Ulm. H2FLY GmbH is working to deliver a hydrogen-electric aircraft powertrain. Clean hydrogen is converted into electricity in the fuel cell system to power the HY4, proving that zero-emission aviation is within reach. The company develops hydrogen-electric aircraft propulsion systems and is a global leader in the development and testing of such systems. In just a few years, hydrogen-electric aircraft are expected to be able to transport 40 passengers over distances of up to 2,000 km. The HY4 first took off in 2016. On September 7, 2023, H2FLY announced that the HY4 has successfully completed the world's first piloted flight of an electric aircraft powered by *liquid* hydrogen. The twin-prop took off from Maribor, Slovenia before completing four flights. The company says that using cryogenically stored liquid hydrogen instead of a gaseous alternative can double the range of the HY4, taking it from 750 km to 1,500 km, as liquified hydrogen enables significantly lower tank weights and volume, meaning more onboard carrying to increase range and improve payload is possible [8].

Another prime example is the **UNIFIER19** program initiated by Slovenian light aircraft manufacturer Pipistrel. It is a new, environmentally friendly and cost-efficient air mobility solution regarding the development and certification of a hybrid electric commuter, designed as a community friendly miniliner. The potential of the proposed design goes beyond a mere cleaner replacement of existing commuters: UNIFIER19 aims at providing an innovative near-zero emission (NZE) air mobility solution. The UNIFIER19 is a 19-passenger commuter with multiple cargo and passenger-seating cabin layouts powered by a modular hybrid-electric powertrain. It is an AEA with CMF type of Distributed Propulsion and deploys a Hydrogen Fuel-Cell system, powering the distributed electric motors that rotate the wing propellers [7].

Project HEAVEN, a European-government-supported consortium assembled to demonstrate the feasibility of using liquid, cryogenic hydrogen in aircraft. The consortium is led by H2FLY and includes the partners Air Liquide, Pipistrel Vertical Solutions, the German Aerospace Center (DLR), EKPO Fuel Cell Technologies, and Fundación Ayesa. Project HEAVEN is funded by the Fuel Cells and Hydrogen 2 Joint Undertaking (FCH 2 JU) under grant agreement no. 826247. The public-private partnership FCH 2 JU supports research, technology development and demonstration activities in fuel cell and hydrogen energy technologies in Europe. HEAVEN is part of the "Horizon 2020" research and innovation program funded by the European Union as well as Spain, France, Germany and Slovenia. In addition to H2FLY, the HEAVEN consortium is made up of the following partners: Air Liquide (designer-supplier of cryogenic tanks), Pipistrel Vertical Solutions d.o.o., a Textron Inc. (NYSE: TXT) company (tank integration and testing), the DLR German Aerospace Center (fuel cell and system architecture operation and testing), EKPO (fuel cell stack) and Fundación Ayesa (cost analysis) [8].

Last but not least, NASA's concept **X-57 Maxwell** is the agency's first all-electric experimental aircraft, or X-plane, and is NASA's first crewed X-plane in two decades. The primary goal of the X-57 project is to share the aircraft's electric-propulsion-focused design and airworthiness process with regulators, which will advance certification approaches for distributed electric propulsion in emerging electric aircraft markets. The X-57 will undergo as many as three configurations as an electric aircraft, with the final configuration to feature 14 electric motors and propellers (12 high-lift motors along the leading edge of the wing and two large wingtip cruise motors) powered through a lithium-ion Battery system. This design driver includes a 500 percent increase in high-speed cruise efficiency, zero in-flight carbon emissions, and flight that is much quieter for the community on the ground. X-57 will also seek to reach the goal of zero carbon emissions in flight, which would surpass the 2035 N+3 efficiency goals. Electric propulsion provides not only a five-to-ten times reduction in greenhouse gas emissions, but it also provides a technology path for aircraft to eliminate 100 Low Lead AvGas, which is the leading contributor to current lead environmental emissions. Additionally, since the X-57 will be battery-powered, it can run off renewable based electricity, making clear the environmental and economic advantages [9].

Εικόνα 3: H2FLY HY4 (1/2)

Εικόνα 4: H2FLY HY4 (2/2)

Εικόνα 5: Pipistrel UNIFIER-19 (1/2)

Εικόνα 6: Pipistrel UNIFIER-19 (2/2)

Εικόνα 7: NASA's X-57 Maxwell (1/2)

Εικόνα 8: NASA's X-57 Maxwell (2/2)

2.7 DIPLOMA THESIS DISTRIBUTED PROPULSION CONCEPT

2.7.1 System Type

The idea of aircraft Distributed Propulsion is not new. Applications of such systems have been considered and developed in the aviation and military industry since the 1930s. These applications albeit were mostly employing only a larger number of regular turbine engines, thus DEN systems. This study revolves around the implementation of a state-of-the-art CMF/Distributed Electric Multi-Fans system, according to the categorization in Chapter 2.1.

This DEP system utilizes the aerodynamic benefits of augmented Lift during Take-Off and Landing and Wing Tip Vortex elimination, the structural benefits of heavy concentrated Load minimization as well as Wing Weight reduction and the topological benefits of Power Production-Propulsion separation. The AEA with DEP conversion would rather be implemented on a general aviation aircraft for simplicity, CAD geometry access, low cost and ease of experimentation reasons. A small, two-seater Light Sport Aircraft would be ideal.

Since the studied aircraft will be converted to an AEA, the concept provides the opportunity to utilize a liquid Hydrogen Fuel-Cell system, thus satisfying Zero-Emission flight targets, as well as the growing Sustainability demands. The electricity is produced by a Fuel-Cell system, utilizing air and hydrogen, with the latter being stored in a Hydrogen Tank in liquid state (-253 °C).

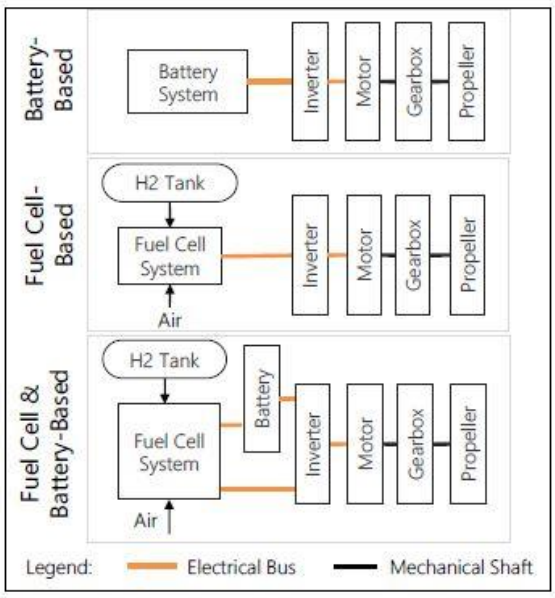

Εικόνα 9: Block Diagram AEA Power Source Architectures

2.7.2 Concept

The Zenith Zodiac CH 650 B propulsion system configuration will be modified in this Thesis in order to investigate the effects of Distributed Electric Propulsion on the wing structure of the aircraft.

The Zodiac's nose-located ICE and propeller are replaced with a Distributed Electric Propulsion system with the electric motors and the fans/propellers mounted spanwise across the wings. The placement of the fuel-cell system powering the electric motors and the distributed propellers, as well as the placement of the tank storing the liquid Hydrogen, are not a matter of particular concern in this Thesis, as it is assumed that they are placed in the fuselage.

NASA's X-57 Maxwell configuration will be significantly followed, so that two Cruise Motors and their Propellers are mounted on the Wingtips and a number of small High-Lift Motors with their Propellers are mounted across the Wingspan of the Zodiac CH 650 B. The Wings now must be able to handle extra loads, due to the weight of the Electric Motors and the Propellers, albeit with fuel no longer needed to be stored in the wing box.

The small spanwise-mounted propellers will be used during take-off and landing in order to increase Lift and provide STOL capabilities, while folding during flight in order to reduce Drag and increase Cruising Efficiency.

Both the high-lift and cruise propellers have a "Inboard Up, Outboard Down" rotation direction. The "Inboard Up, Outboard Down" in the high-lift propellers is preferred due to the lift distribution augmentation towards the fuselage rather than the wing tip, caused by the slipstream effect, explained further in Chapter 4.1.5. A lift distribution stronger towards the fuselage is desirable for structural reasons. The "Inboard Up, Outboard Down" in the cruise propellers presents the advantage of cruise propellers essentially rotating counter to the wing tip vortex direction in order to eliminate induced drag.

3.0 AIRCRAFT SPECIFICATIONS

3.1 LIGHTWEIGHT STRUCTURES

The Design Philosophy of Lightweight Structures refers to the design of a structure with the lowest possible weight, while at the same time maintaining or enhancing the required strength. The goal of lightweight structures is to achieve optimal stiffness, stability and functionality while using less material, which can lead to various benefits, such as energy savings, reduced environmental impact and improved transportability.

Applications of Lightweight Structures can be found in aerospace and motorsport, where one of the most critical performance factors is weight. Lightweight Structure applications can also be found in the automotive and marine industry, civil engineering projects and sports equipment. Essentially, when designing a lightweight structure, the strength-to-weight ratio must be maximized, either by minimizing the weight/material used while maintaining the desirable strength, or by using materials with higher stiffness-to-weight ratio.

This can be achieved through advanced Structural Mechanics, Finite Element Analysis, computational tools such as Topology Optimization or utilization of high strength-to-weight ratio Materials such as composites, aluminum, titanium, and high strength steels.

Depicted below are; a honeycomb sandwich panel that presents a notably increased bending stiffness with a minimal weight penalty; an airframe that is the definition of an aircraft lightweight structure, and finally a metal component with levels of topology optimization, that could be a motorsport application such as a suspension mount part.

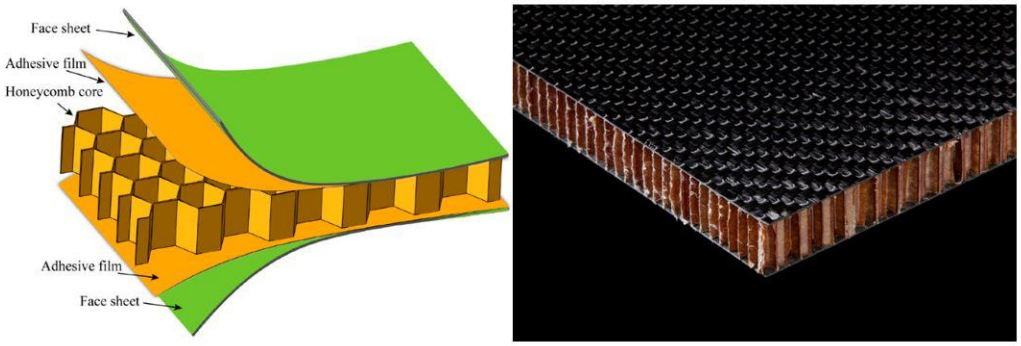

Εικόνα 10: Honeycomb Sandwich Panel

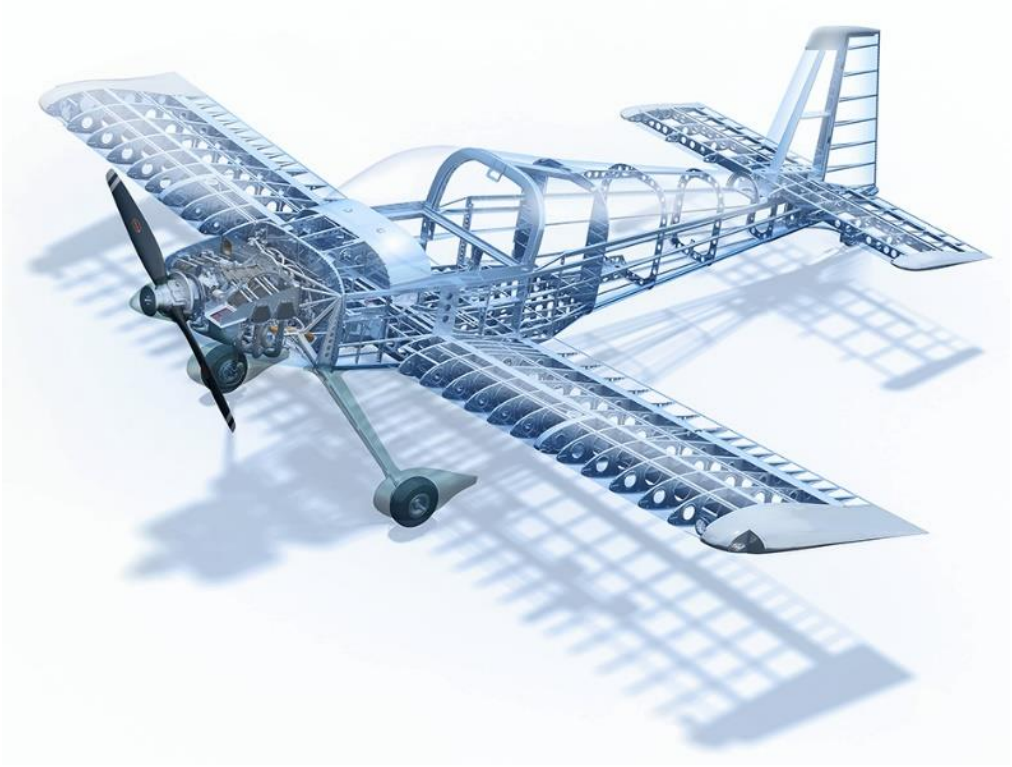

Εικόνα 11: Lightweight Structure Airframe

Εικόνα 12: Stages of Topology Optimization on a Metal Part

3.2 MATERIAL USED

The material used in the components of the Zenith Zodiac CH 650 B wing structure is the Aluminum Alloy series Al 6061-T6. Besides the recent surge in composite materials utilization, Aluminum Alloys are the most common material used in the aerospace industry. That is due to the low weight it presents compared to other metals, the excellent mechanical properties, strength-to-weight ratio and machinability, the decent corrosion resistance, the satisfying recyclability and the relatively low cost.

The material properties of Al 6061-T6 are presented below, along with the tensile experiment figures [10].

6061-T6 Aluminum

Material Notes

Component	Wt. %	Component	Wt. %	Component	Wt. %
Al	95.8 - 98.6	Mg	0.8 - 1.2	Si	0.4 - 0.8
Cr	0.04 - 0.35	Mn	Max 0.15	Ti	Max 0.15
Cu	0.15 - 0.4	Other, each	Max 0.05	Zn	Max 0.25
Fe	Max 0.7	Other, total	Max 0.15		

Physical Properties	Metric	English	Comments
Density	2.7 g/cc	0.0975 lb/in³	AA; Typical
Mechanical Properties			
Hardness, Rockwell B	60	60	Converted from Brinell Hardness Value
Hardness, Vickers	107	107	Converted from Brinell Hardness Value
Ultimate Tensile Strength	310 MPa	45000 psi	AA; Typical
Tensile Yield Strength	276 MPa	40000 psi	AA; Typical
Elongation at Break	12 %	12 %	AA; Typical; 1/16 in. (1.6 mm) Thickness
Modulus of Elasticity	68.9 GPa	10000 ksi	AA; Typical; Average of tension and compression. Compression modulus is about 2% greater than tensile modulus.
Poisson's Ratio	0.33	0.33	Estimated from trends in similar Al alloys.
Fatigue Strength	96.5 MPa	14000 psi	AA; 500,000,000 cycles completely reversed stress; RR Moore machine/specimen
Fracture Toughness	29 MPa-m½	26.4 ksi-in½	KIC; TL orientation.
Shear Strength	207 MPa	30000 psi	AA; Typical

Πίνακας 4: Al6061-T6 Properties

AL6061-T6 Strength properties:

Yield Tensile/Compression Strength: 276 MPa

Ultimate Tensile/Compression Strength: 310 MPa

Shear Strength: 207 MPa

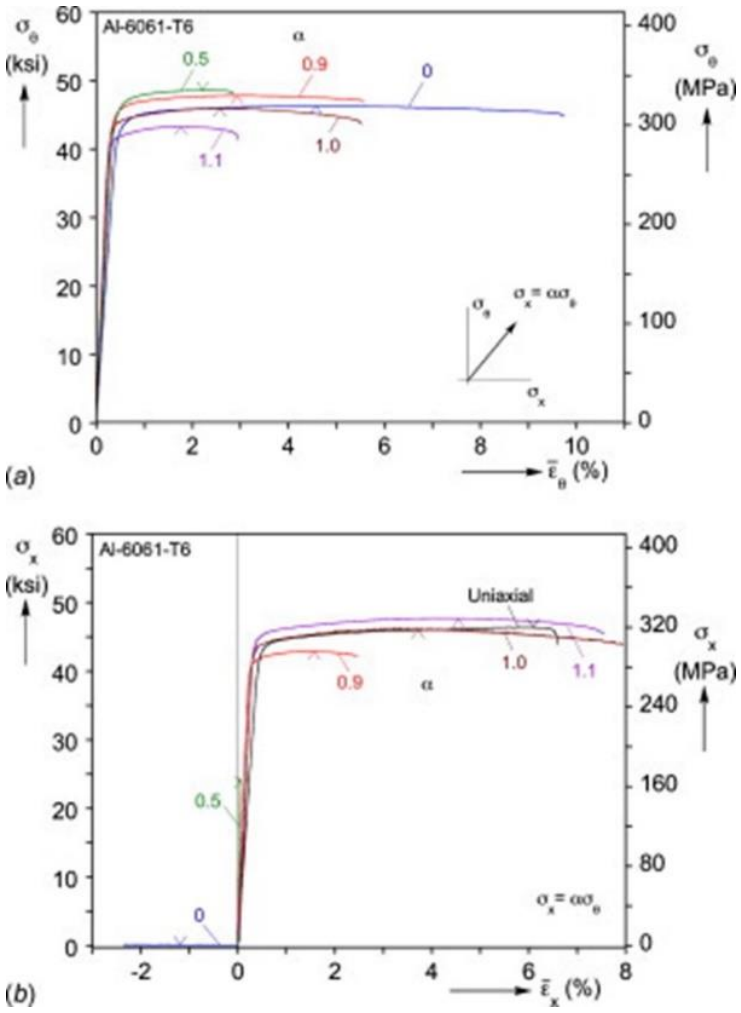

Εικόνα 13: Al6061-T6 Compression Tensile Diagrams

Every component of the Zenith Zodiac CH 650 B wing structure is made from Al6061-T6. However, the fasteners used in the Wing-Fuselage joint (AN-5 Bolts) and the Spar-Root Doubler joint (AN-4 Bolts) are made from Alloy Steel, usually 8740 or 4037.

According to [25], AN Bolts have a minimum tensile strength of 125000 psi and a shear strength of 76000 psi.

STEEL AN BOLTS Strength properties:

Tensile/Compression Strength: 862 MPa

Shear Strength: 524 MPa

3.3 AIRCRAFT DESCRIPTION

The aircraft to be studied in the Diploma Thesis is the Zodiac CH 650 B, produced by Zenith Aircraft Company, that belongs to the Light Sport Aircraft (LSA) category. It is a 2-seat, single engine, non-pressurized cabin aircraft, that due to its design flexibility can be equipped with a plethora of engines, usually with an engine power of 100-130 HP [12].

The Zenith Zodiac CH 650 B has all the typical characteristics of a small single engine aircraft. Its design principles revolve around simplicity, ease of assembly with basic tools, while the chosen method of structural assembling is riveting. Finally, reliability and safe flight has been a great focus with the Zodiac CH 650 B, due to its predecessor's (CH 601) failure history. With the CH 650 B's wing design, no structural failure has been recorded [12].

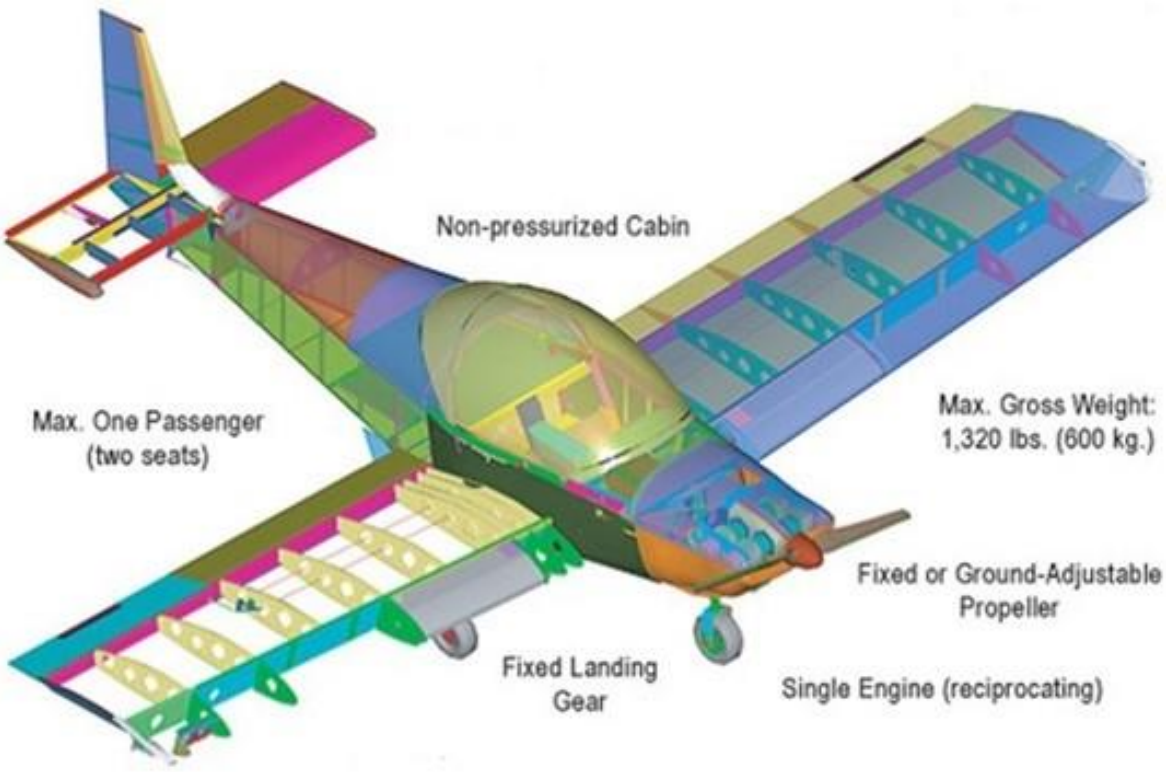

Εικόνα 14: Zenith Zodiac CH 650 B

SPECIFICATIONS	Jabiru 3300		Continental O-200	
LENGTH	20 Ft. 0 In.	6.1 m.	20 Ft. 0 In.	6.1 m.
HEIGHT (rudder tip)	6 Ft. 6 In.	1.98 m.	6 Ft. 6 In.	1.98 m.
WING SPAN	27 Ft. 0 In.	8.23 m.	27 Ft. 0 In.	8.23 m.
WING AREA	132 Sq. Ft.	12.3 m.sq.	132 Sq. Ft.	12.3 m.sq.
WING CHORD (root / tip)	5' 3" / 4' 7"	1.6 m. / 1.4 m.	5' 3" / 4' 7"	1.6 m. / 1.4 m.
HORIZONTAL TAIL SPAN	7 Ft. 7 In.	2.3 m.	7 Ft. 7 In.	2.3 m.
HORIZONTAL TAIL AREA	20 Sq.Ft.	2.24 m.sq.	20 Sq.Ft.	2.24 m.sq.
EMPTY WEIGHT	695 Lbs.	318 kg.	750 Lbs.	340 kg.
DESIGN GROSS WEIGHT	1,320 Lbs.	600 kg.	1,320 Lbs.	600 kg.
USEFUL LOAD	625 Lbs.	282 kg.	570 Lbs.	260 kg.
FUEL CAPACITY (Standard) – FUEL WEIGHT	24 US Gal. = 144 Lbs.	92 *l.* = 65 kg.	24 US Gal. = 144 Lbs.	92 *l.* = 65 kg.
FUEL CAPACITY (Extended Option) – FUEL WEIGHT	30 US Gal. = 180 Lbs.	112 *l.* = 82 kg.	30 US Gal. = 180 Lbs.	112 *l.* = 82 kg.
WING LOADING	9.8 Lbs./Sq.Ft.	48 kg./m.sq.	9.8 Lbs./Sq.Ft.	48 kg./m.sq.
POWER LOADING	13.2 Lbs./BHP	6 kg./HP	13.2 Lbs./BHP	6 kg./HP
DESIGN LOAD FACTOR (Ultimate)	+6 / –3 G	+6 / –3 G	+6 / –3 G	+6 / –3 G
CABIN WIDTH (Shoulders)	44 In.	112 cm.	44 In.	112 cm.
NEVER EXCEED SPEED (V_{NE})	160 MPH	260 km/h	160 MPH	260 km/h

Πίνακας 5: Zenith Zodiac CH 650 B Specifications

PERFORMANCE				
Peformance at Gross Weight	**Jabiru 3300**		**Continental O-200**: 100 hp	
TOP SPEED	148 MPH	238 km/h	140 MPH	225 km/h
CRUISE SPEED (75%)	138 MPH	222 km/h	135 MPH	218 km/h
STALL SPEED (Flaps Down)	44 MPH	70 km/h	44 MPH	70 km/h
RATE OF CLIMB	930 fpm	4.8 m/s	1,000 fpm	5 m/s
TAKE OFF ROLL	500 Ft.	152 Ft.	500 Ft.	152 Ft.
LANDING ROLL	500 Ft.	152 Ft.	500 Ft.	152 Ft.
SERVICE CEILING	16000+ Ft.	4875+ m.	16000+ Ft.	4875+ m.
RANGE (Standard)	575 statute miles	925 km.	560 miles	900 km.
ENDURANCE (Standard)	4.2 Hours	4.2 Hours	4.0 Hours	4.0 Hours

Πίνακας 6: Zenith Zodiac CH 650 B Performance

Note: *The Stall Speed with Flaps Up increases from 70km/h to 80km/h.*

The Wing of the Zenith Zodiac CH 650 B has a straight leading edge and a tapered trailing edge, as seen in the aircraft Dimensions below. That means that the chord length is variable spanwise, with the wing root chord being slightly larger than the wing tip chord.

Also, the Wing presents a dihedral design, meaning that the Wings are tilted upwards and thus are not parallel to the ground plane. The primary reason of applying the wing dihedral is to improve the lateral stability of the aircraft. The lateral stability is mainly a tendency of an aircraft to return to original trim level wing flight condition if disturbed by a gust and rolls around the x axis. The dihedral angle of the Zenith Zodiac CH 650 B is equal to $\Gamma = 5.65°$ (10%).

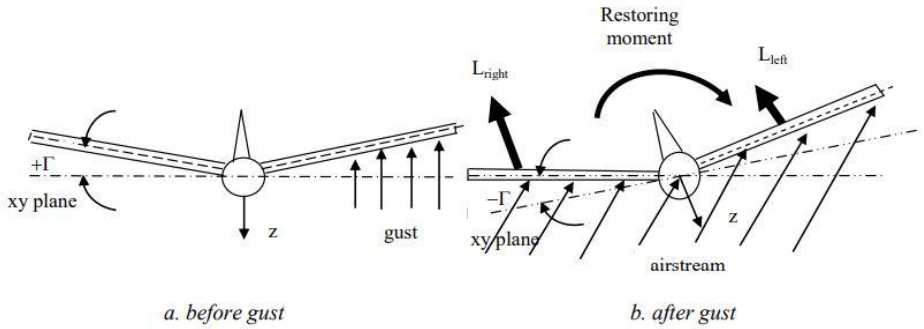

Εικόνα 15: Dihedral Angle

The airfoil used in the Zenith Zodiac CH 650 B is a RIBLETT GA 35-A-415 [16] and is the airfoil used also in the predecessor model, the Zenith Zodiac CH 601.

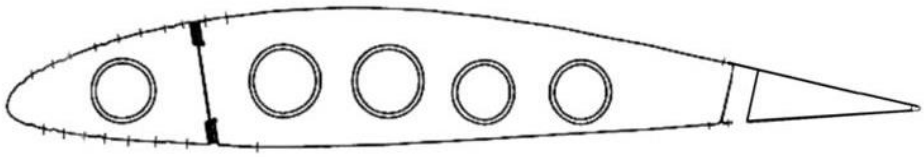

Εικόνα 16: Riblett GA 35-A-415 Wing Sideview

The Internal Combustion Engines originally used in the Zodiac CH 650 B are the Jabiru 3300 and the Continental O-200 [11]. Here are some technical specifications:

	Jabiru 3300	**Continental O-200**
Type | Cylinders	Boxer | 6	Boxer | 4
Power @ 2750 RPM (kW | HP)	89 | 120	75 | 100
Weight (kg | lbs)	81 | 180	91 | 200

Πίνακας 7: Zenith Zodiac CH 650 B ICE Specifications

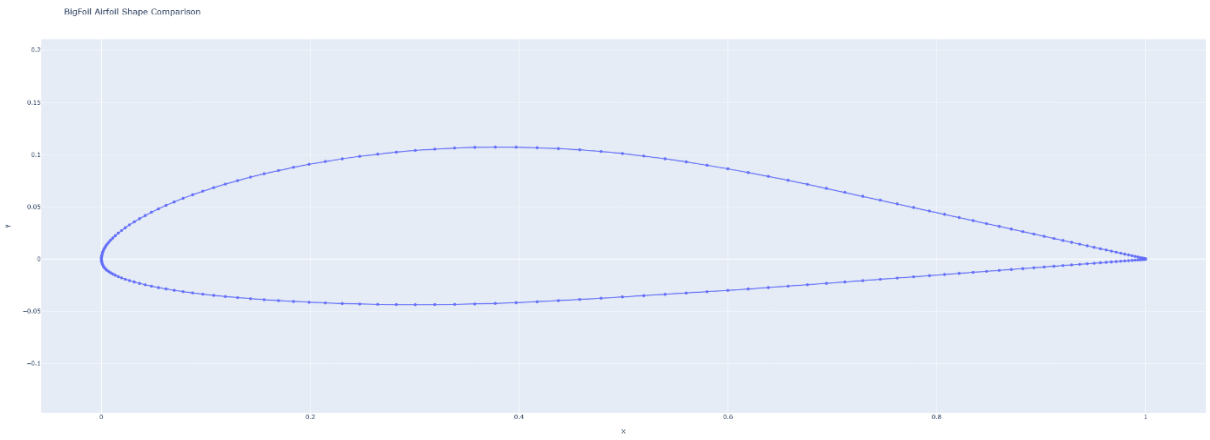

Εικόνα 17: Riblett GA 35-A-415 Airfoil Shape

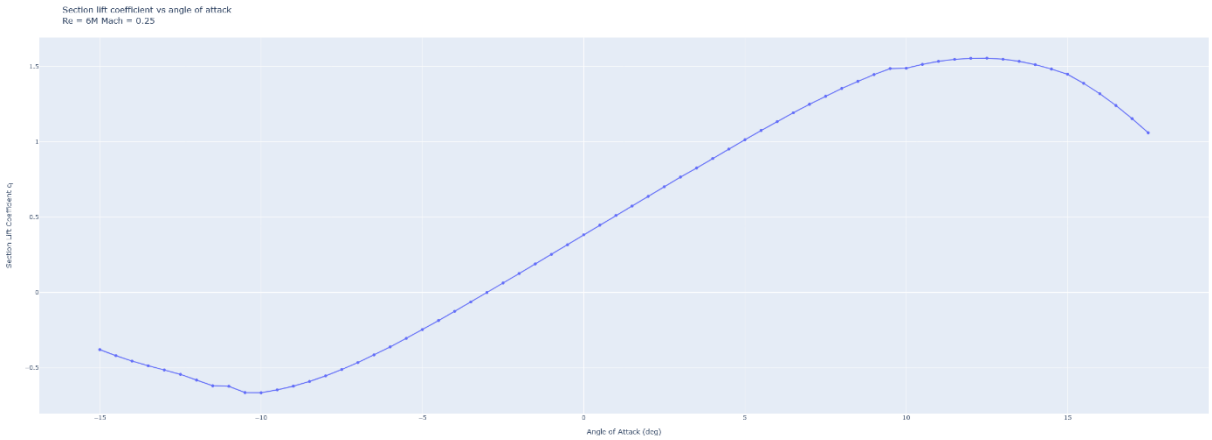

Εικόνα 18: Riblett GA 35-A-415 Lift Coefficient vs Angle of Attack

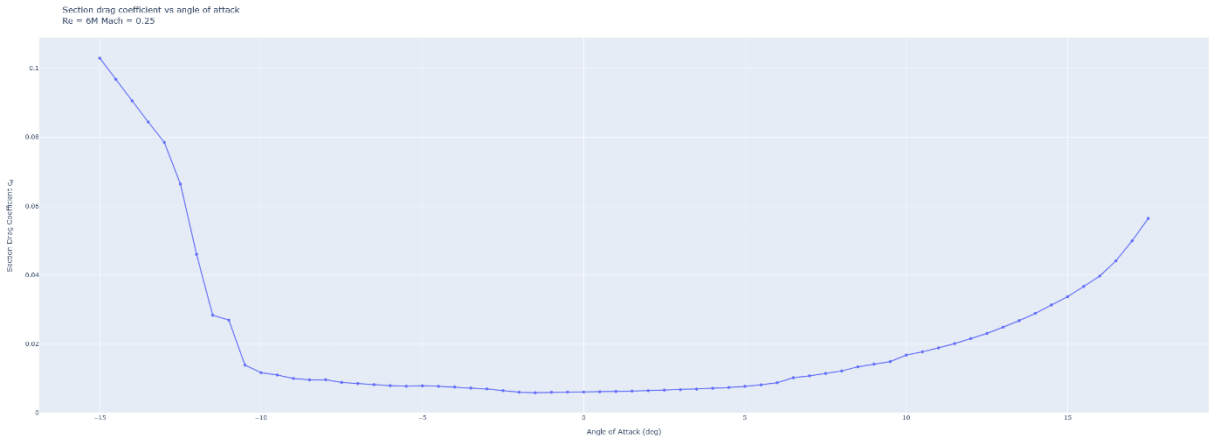

Εικόνα 19: Riblett GA 35-A-415 Drag Coefficient vs Angle of Attack

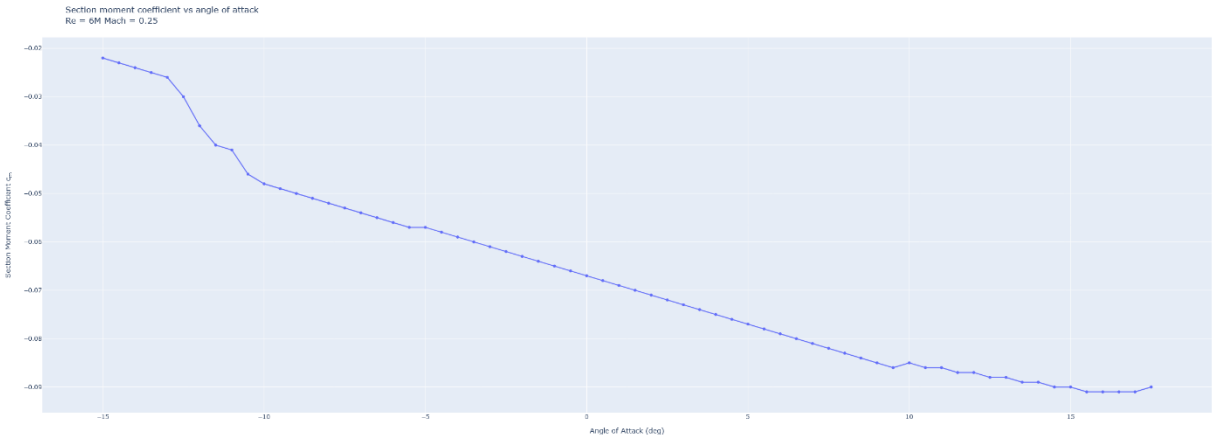

Εικόνα 20: Riblett GA 35-A-415 Pitching Moment Coefficient vs Angle of Attack

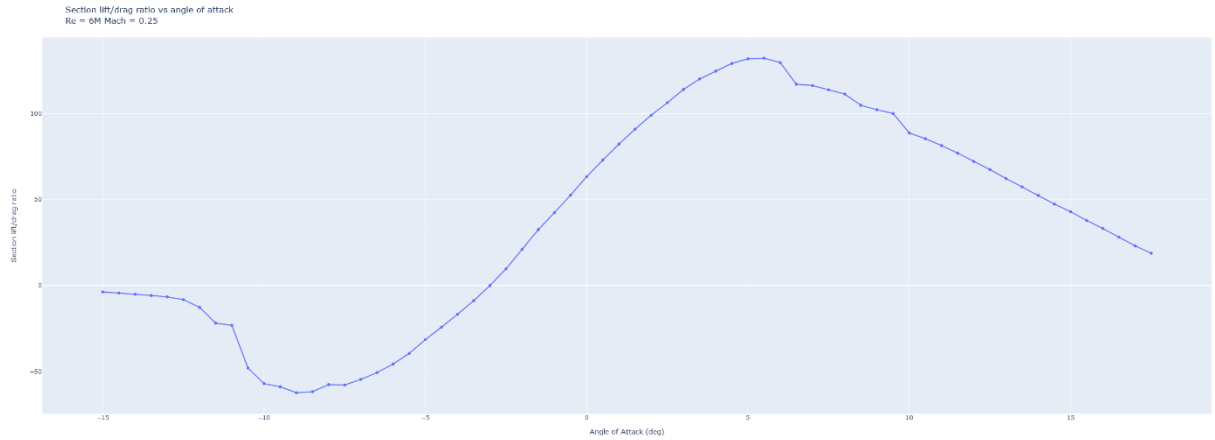

Εικόνα 21: Riblett GA 35-A-415 Lift/Drag Ratio vs Angle of Attack

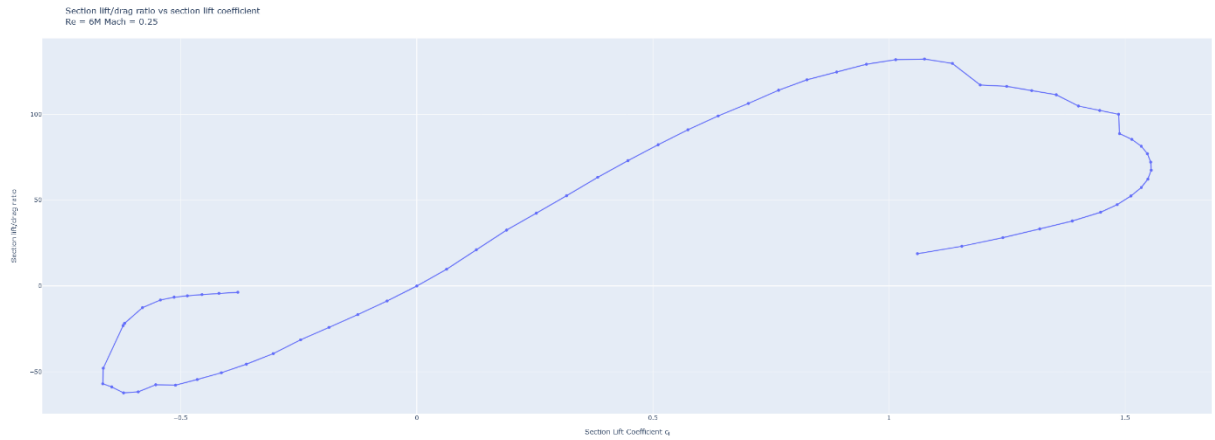

Εικόνα 22: Riblett GA 35-A-415 Lift/Drag Ratio vs Lift Coefficient

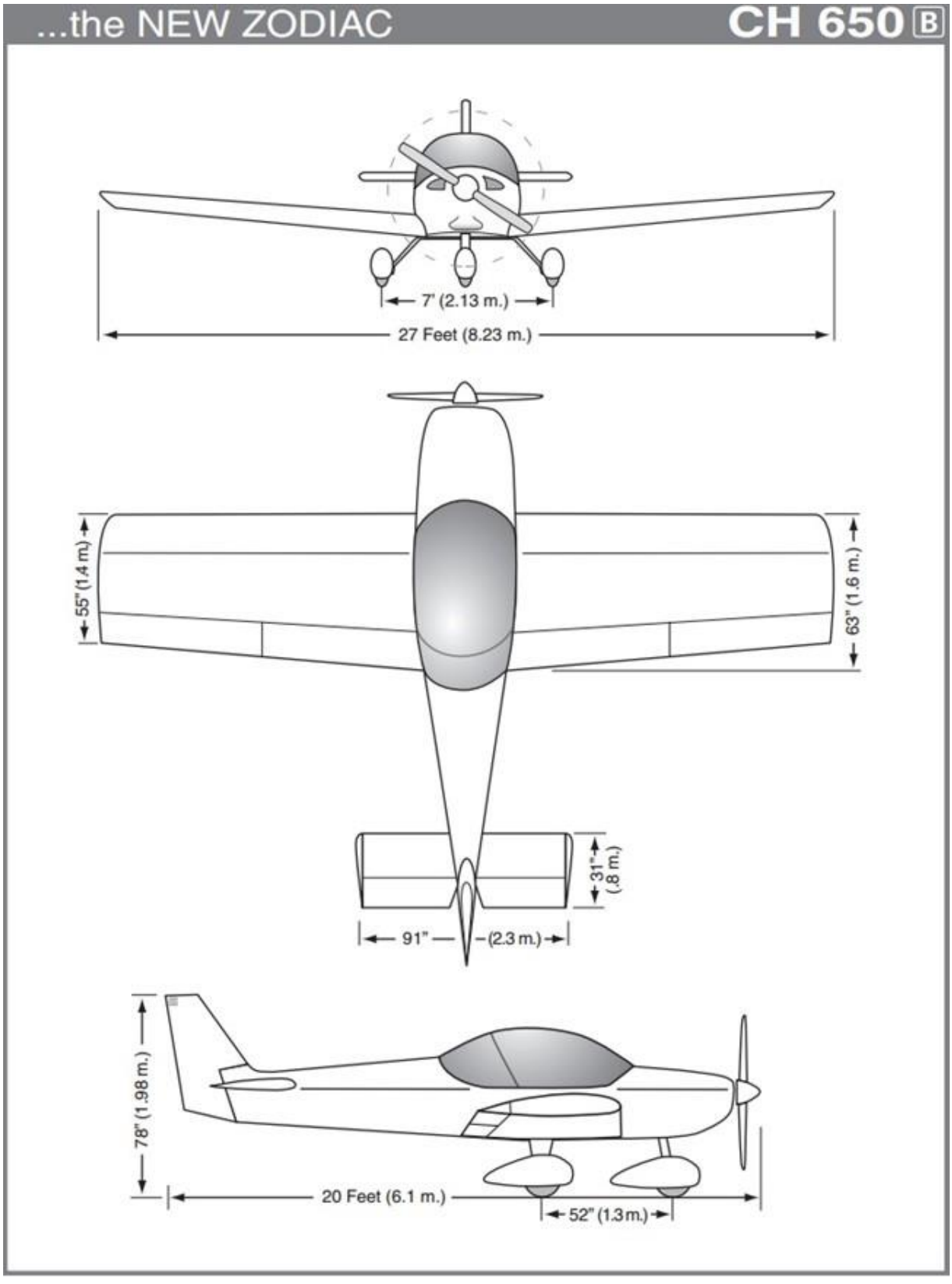

Εικόνα 23: Zenith Zodiac CH 650 B Dimensions

3.4 WING STRUCTURE

A typical wing structure is designed to carry and transmit the loads towards the fuselage safely while also preventing displacements that impact the aerodynamic behavior of the aircraft.

The wing structure consists of the external wing structure (Skin) and the primary and secondary internal wing structure.

The wing structure is responsible for transmitting the mentioned loads, thus longitudinal beams from the wing root to the wing tip (Spars) are used. The number of Spars varies, depending on the wing geometry and the magnitude of the loads. For example, an airfoil with a large chord requires at least two spars due to increased torsional loads. The most common number of Spars used is two, but the number of spars is ultimately a design choice.

The number of Spars used to shape the Wing Box in an aircraft wing could be a subject of further academic research.

The primary wing structure is the Wing Box or Torsion Box and consists of the combination of multiple spars. It is the structural center of the wing and most of the wing components (engines, landing mechanisms) and moving surfaces (slats, flaps, ailerons) are bolted on it. The Torsion Box is also utilized as fuel storage and is designed accordingly to meet the range requirements, as well as the demands of the structural engineer and the aerodynamicist.

The secondary wing structure consists of sheets perpendicular to the Spars (Ribs) and beams parallel to the Spars (Stringers) that support the sheets forming the external surface of the wing (Skin) against Buckling and fuel moving during maneuvers.

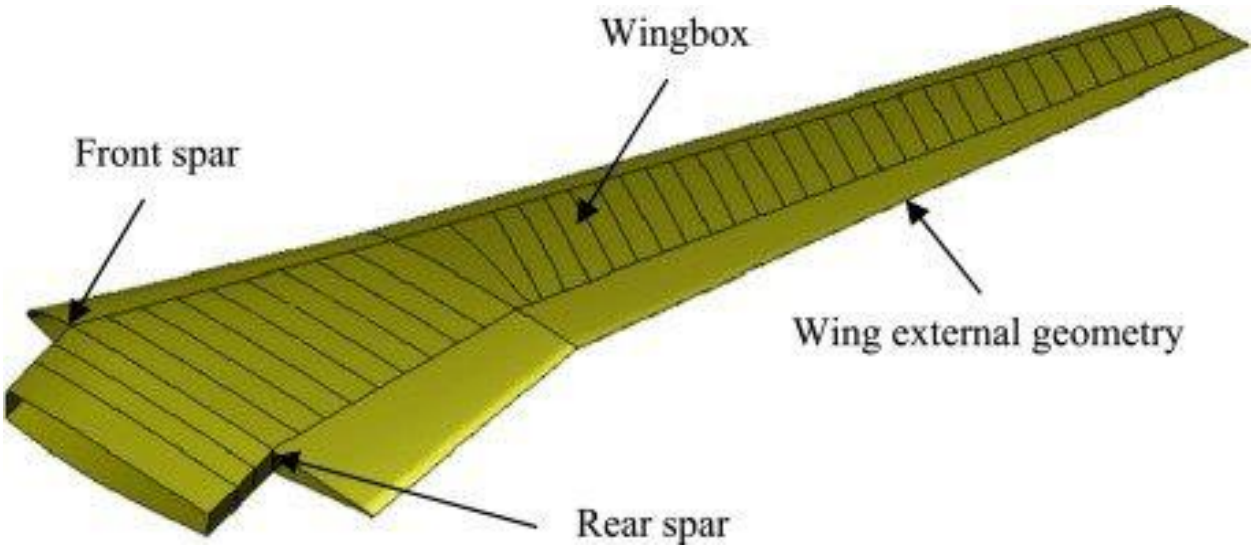

Εικόνα 24: Torsion Box of Aircraft Wing

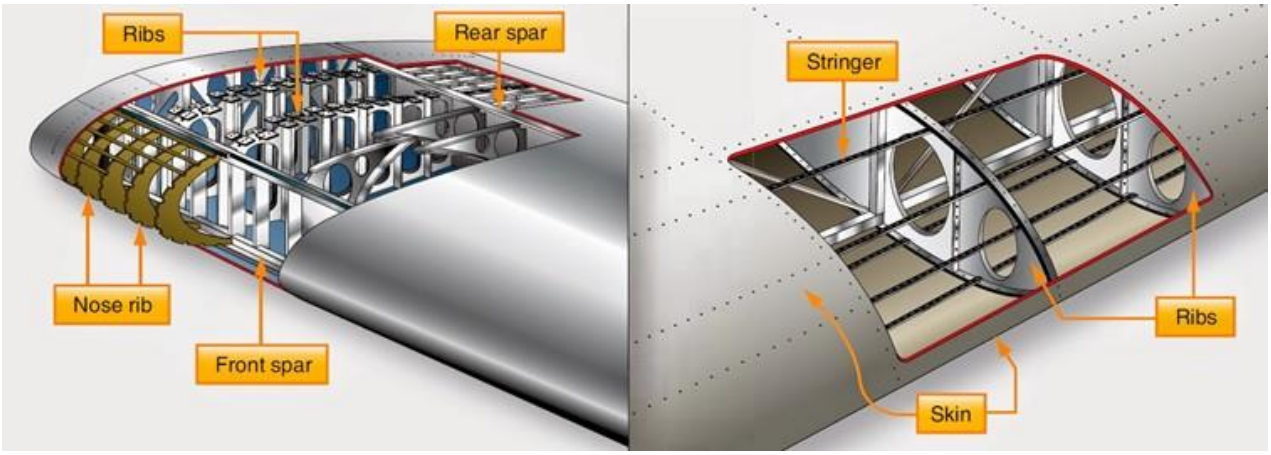

Εικόνα 25: Wing Structure Stiffeners

As we can see below, the components of the Zenith Zodiac CH 650 B wing structure are:

- **Wing Spar**: The Wing Spar is defined as the main lateral member of the aircraft's wing structure. In a fixed wing aircraft, the Wing Spar is usually the main structural wing component, running across the wingspan, while other wing components such as the Ribs are bolted on it. The Wing Spar handles most of the wing Load, such as its own weight, static, aerodynamic and other forces.
- **Stringers**: Stringers are essentially stiffeners, usually of L cross section, that provide more wing structural stability.
- **Ribs**: Ribs are longitudinal components that provide the wing's aerodynamic shape and contribute to the increase of its strength. Ribs are bolted on the Wing Spar and constitute the wing's lightweight structure. The wing's Skin follows the geometry created by said lightweight structure.
- **Rear Spar Channel**: The Rear Spar Channel provides extra wing stability, while the Ribs' other edges, the Flaps and the Ailerons are bolted on it.
- **Skin**: The wing's Skin is a thin-walled sheet metal that covers the wing structure.
- **Flaps**: The Flap is a fixed or rotating component of an aircraft's wing that is used to manipulate the Lift and the Drag for a shorter takeoff and a landing with a lower speed. When the Flaps are deployed, the curvature of the airfoil is changed, and the rate of descent is increased while landing. Also, the Lift is increased, allowing the aircraft to produce the same Lift in lower speeds, albeit with Drag being increased too. Flaps can be partially deployed during takeoff for STOL.
- **Ailerons**: The Ailerons provide Roll control. They are usually coupled so that when one is moving upwards, the other is moving downwards. The Lift is increased in the side of the upwards moving Aileron, while decreased in the side of the downwards moving Aileron, thus instigating the aircraft's Roll movement.
- **Wing Tip**: The Wing Tip is the wing's free edge. It can have different geometries and shapes, impacting the generated Drag and the Wing Tip vortices.

Longitudinal is the fuselage axis, also known as the Roll axis. Lateral is the spanwise axis perpendicular to the longitudinal axis, also known as the Pitch axis, as also shown below.

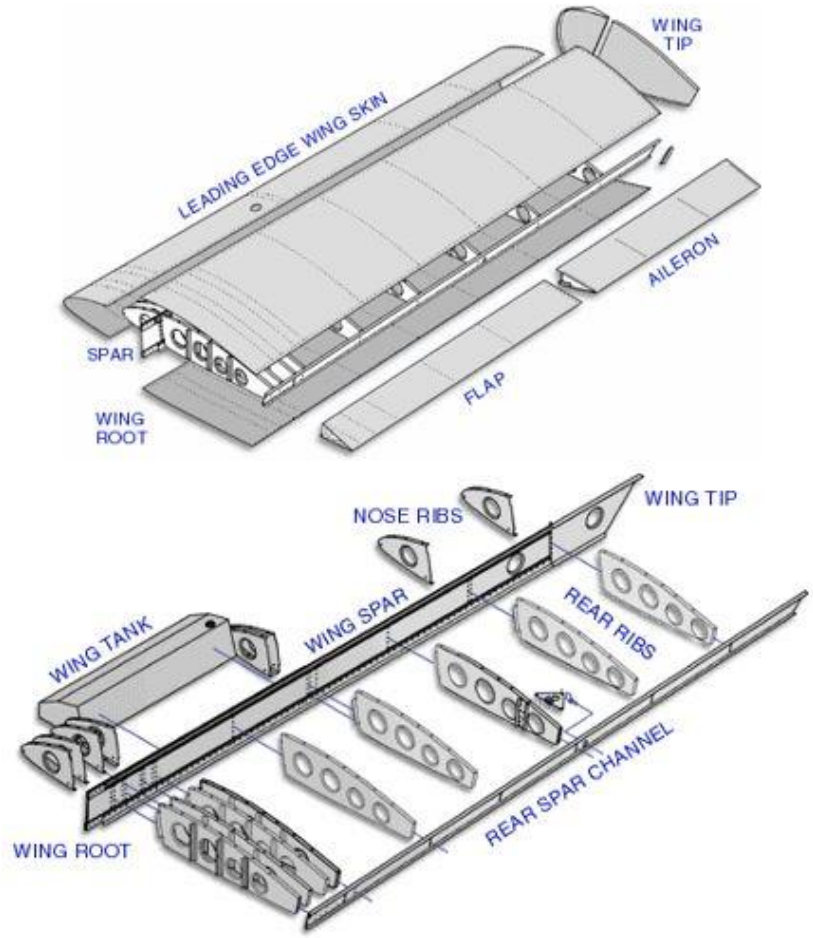

Εικόνα 26: Zenith Zodiac CH 650 B Wing Structure

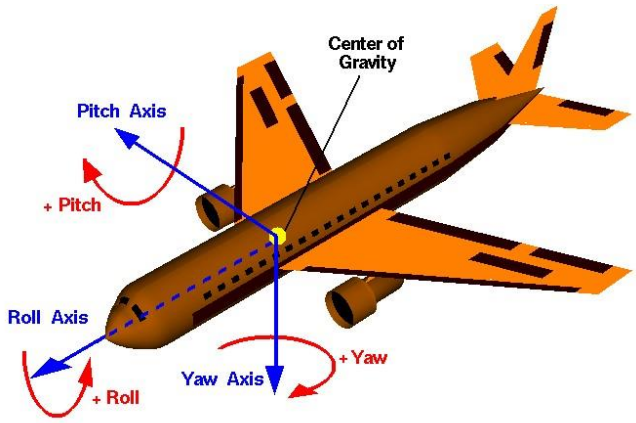

Εικόνα 27: Aircraft Coordinate System

4.0 PROPOSED METHODOLOGY OF WING STRUCTURAL ANALYSIS

4.1 THEORETICAL BACKGROUND

4.1.1 Bending Theory

Assuming a beam similar to the one pictured below, with the coordinate system X,Y,Z as seen. The Bending Theory is used in applied mechanics to explain the way a beam behaves when exposed to external force. When a beam is subjected to a loading system or by a force couple acting on a plane passing through the axis, then the beam deforms. This axial deformation is called bending of a beam. Due to the shear force and bending moment, the beam undergoes deformation. These normal stresses due to bending are called bending normal stresses. The bending moment, M, along the length of the beam can be determined from the moment diagram M.

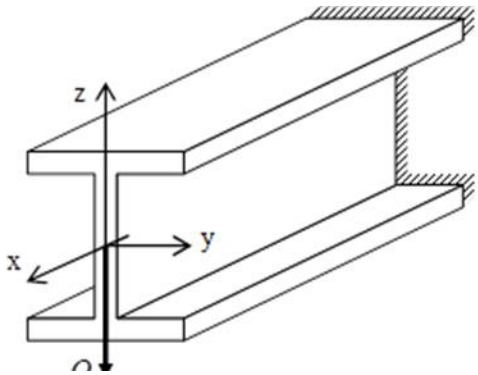

Εικόνα 28: Simple Beam

The Bending Law states:

$$\sigma = \frac{M_y}{I_y} z - \frac{M_z}{I_z} y \quad [MPa]$$

where σ is the bending normal stress, M is the bending moment and I is the second moment of inertia of the cross-section about the axes y, z.

The neutral zone is the locus of points with zero bending normal stress. If the Bending Law is solved for $\sigma = 0$, the neutral zone expression can be obtained:

$$z = \frac{M_z I_y}{M_y I_z} y \quad [m]$$

In the case of simple bending about the y-axis, the Bending Law is simplified as the $-\frac{M_z}{I_z} y$ factor is equal to zero. Hence:

$$\sigma = \frac{M_y}{I_y} z \quad [MPa]$$

The bending stress is zero at the beam's neutral zone and it increases linearly away from the neutral zone until the maximum values at the top and bottom of the beam cross-section. It is the line that passes through the centroid of the cross-section and is perpendicular to the plane of bending.

The maximum bending stress occurs at the extreme fiber of the beam and is calculated as:

$$\sigma_{max} = \frac{M_y}{I_y} z_{max} \quad [MPa]$$

where σ is the bending stress, M is the bending moment and I is the second moment of inertia of the cross-section.

The shear stress is zero at the free surfaces (the top and bottom of the beam), and it is maximum at the center of the cross-section. The equation for shear stress at any point located a distance from the center of the cross-section is given by:

$$\tau = Q_z \frac{S_y(z)}{I_y \cdot t} \quad [MPa]$$

where τ is the shear stress, Q is the shear force, S is the first moment of inertia of the cross-section about the neutral zone, I is the moment of inertia of the cross-section, and t is the width of the cross-section.

4.1.2 Shear Flow Theory

As previously mentioned, the philosophy behind Lightweight Structures is the minimization of weight without compromising the stiffness and the strength of the structure. Thus, thin sheet metal beams are designed, reinforced with strong Flanges and Ribs, due to their sensitivity to low load buckling. This philosophy produces thin-walled beams capable of safely handling the applied loads. Loads are transmitted to the structure mostly through sheet metal shear flows and as a result the beams are also called shear beams [5].

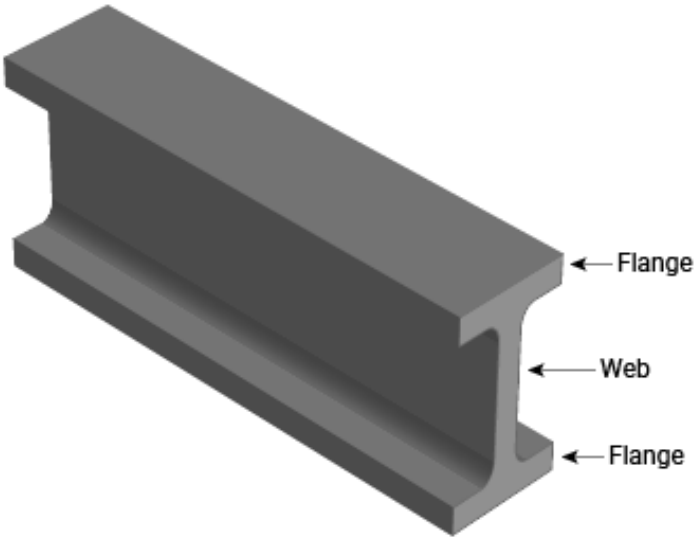

Εικόνα 29: I-Beam Anatomy

Shear Flow Theory's aim is to express simple equations so that an engineer can easily calculate the shear load flow of complicated structures and perform simple analyses with satisfying result precision, as often a quick and satisfying analysis is more important than a detailed one. The theory assumptions are mostly related to the simplification of the structure and its behavior to certain loads. The analysis is performed in the simplified structure model and the accuracy of results depends on the quality of simplification.

In the example of the H-Beam below, the impact of simple assumptions on the analysis and on the results accuracy is examined. From simple Bending Theory, it is known that normal bending stresses (flexural stresses) develop in the beam, which increase linearly with the distance from the neutral zone and become maximum in the outer zones of the beam.

$$\sigma_x(z) = \frac{M_y}{I_y} \cdot z, \qquad \sigma_{max} = \frac{M_y}{I_y}\frac{h}{2} \tag{4.1}$$

Shear stresses are also developed in the beam, and mostly in the Web. The shear stress distribution is parabolic and is function of the distance from the cross-section's center of gravity. The maximum value of the shear stress is located at the cross-section's center of gravity.

$$\mathrm{q}(z) = \tau_{xz}(z) \cdot t = Q_z \frac{S_y(z)}{I_y}, \qquad q_{max} = \mathrm{Q_z}\frac{S_y^{max}}{I_y} \tag{4.2}$$

In the Equations (4.1), (4.2), Q_y is the applied bending Force, I_y is the Second Moment of Inertia about the bending axis y and S_y is the First (or Static) Moment of Inertia of part of the cross-section, between z and h/2, about the bending axis y.

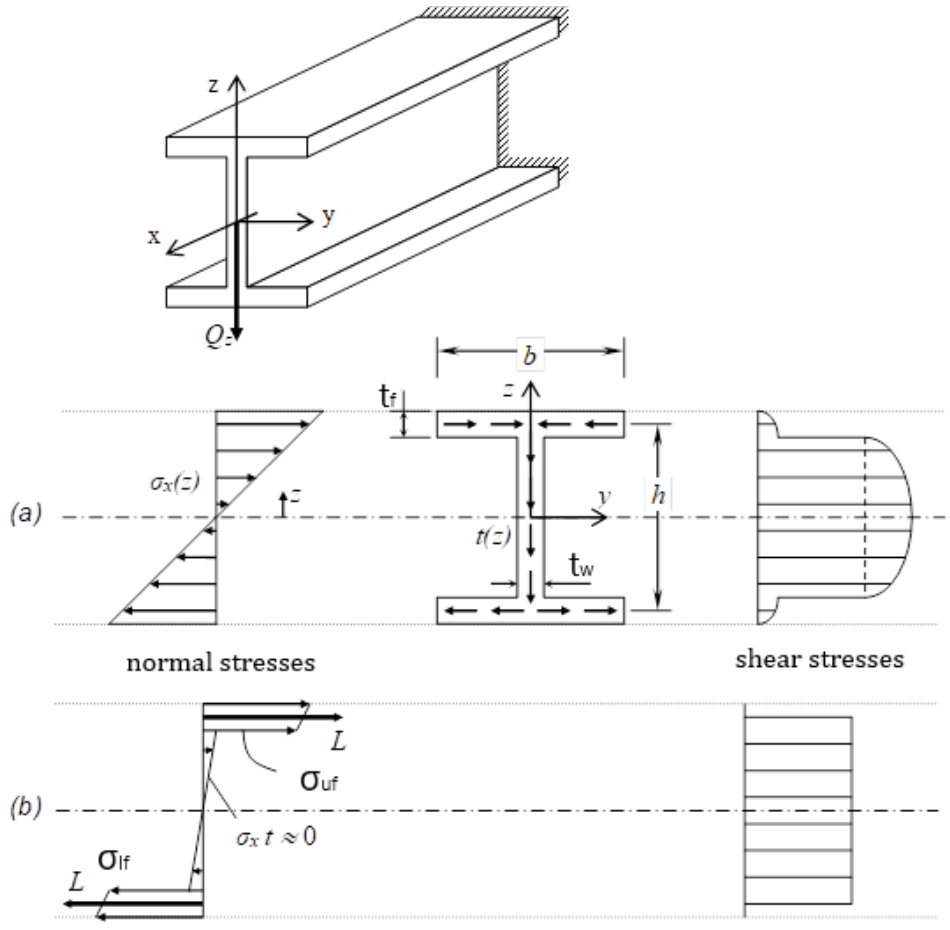

Εικόνα 30: I-Beam Cross Section (Normal and Shear) Stress Distribution

In the Figure above, the distribution of normal and shear stresses in the cross section in a position x of the beam is depicted. The majority of the load is applied to the Flanges, while the Web handles a very small part of the load.

If the assumption that the load handled by the Web is negligible compared to the respective load handled by the Flanges is made, the equations (4.1), (4.2) are significantly simplified. Then, it can be assumed that the normal stresses are received exclusively by the Flanges. Thus, each Flange handles a normal force $L = \sigma F$ where F is the Flange cross-section and σ is the Flange mean normal stress, so that the static equivalence $M_y(x) = Lh$ between the moment $M_y(x)$ and the pair of forces L applies:

$$\sigma = \sigma_{uf} = -\sigma_{lf} = \frac{L}{F_f} = \frac{M_y(x)}{h \cdot F_f} \tag{4.3}$$

In Equation 4.3, σ_{uf} is the normal stress of the upper flange, while σ_{lf} is the normal stress of the lower flange.

Assuming that the Web does not handle any normal stresses, the Web shear flow $q = \tau t$ is constant across the Web's height. This conclusion can be reached by studying the equivalence of a differential section dx of the beam's Flange in the direction x, as shown in the Figure below:

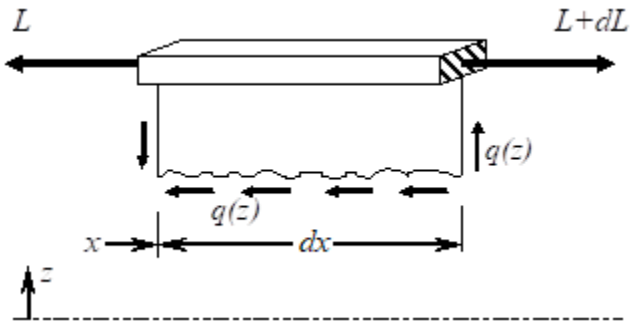

Εικόνα 31: Shear Flow (constant) across Web's height

$$dL = q(z)dx$$

$$q(z) = \frac{dL}{dx} = \frac{d(M/h)}{dx} = \frac{1}{h}\frac{dM}{dx} = \frac{Q}{h} \tag{4.4}$$

It is now mathematically proven that the Web shear flow is constant and not parabolic, and is only a function of the shear force Q and the Web height h.

An easy mistake would be to compare the theoretical maximum normal and shear stresses given by Eq. (4.1) and (4.2) with the respective approximate values given by Eq. (4.3) and (4.4). To compare the normal stresses, the second moment of inertia I_y of the I-beam's cross-section must be calculated first. To calculate the I-beam's second moment of inertia, the cross section is divided into three rectangular sections, the Web and the two Flanges. Apart from the three rectangular sections' moments of inertia, the Flanges' Steiner Factor must be taken into account since the Flanges' center of gravity does not coincide with the I-beam's respective CoG. Thus:

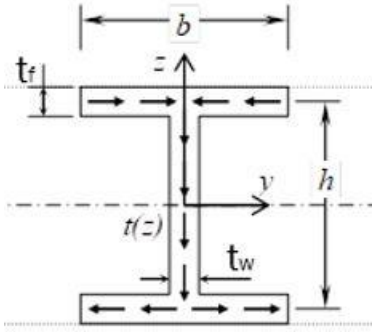

Εικόνα 32: I-Beam Parameters

$$I_y = I_y^{web} + 2 \cdot I_y^{flange} + 2 \cdot SteinerFactor = \frac{t_w \cdot h^3}{12} + 2\frac{b \cdot t_f^3}{12} + 2\left(\frac{h}{2}\right)^2 F_{flange} \Rightarrow$$

$$I_y = \frac{t_w \cdot h^3}{12} + 2\frac{b \cdot t_f^3}{12} + 2\left(\frac{h}{2}\right)^2 F_f = 2F_f\left(\frac{h}{2}\right)^2 \left(1 + \frac{1}{6}\frac{t_w h}{t_f b} + \frac{1}{3}\frac{t_f^2}{h^2}\right) \quad (4.5)$$

If we assume that the factor $\frac{t_f^2}{h^2} \ll 1$, then the Eq. (4.5) gives the second moment of inertia approximate value:

$$I_y \simeq 2\left(\frac{h}{2}\right)^2 F_f\left(1 + \frac{1}{6}\frac{F_w}{F_f}\right) \quad (4.6)$$

Normal Stress: Using Eq.(4.6) in Eq. (4.1), the maximum normal stress in an I-beam is:

$$\sigma_{max} \simeq \frac{M_y}{2\left(\frac{h}{2}\right)^2 F_f\left(1+\frac{1F_w}{6F_f}\right)} \quad (4.7)$$

The difference between the approximate and the theoretical maximum normal stress is only the factor $\frac{1}{6}\frac{F_w}{F_f}$, thus the error is equal to:

$$e = \frac{\sigma_{max} - \sigma_{uf}}{\sigma_{max}} = \frac{1}{6}\frac{F_w}{F_f} \tag{4.8}$$

If we assume that $\frac{1}{6}\frac{F_w}{F_f} \ll 1$, then the error regarding the approximate and the theoretical maximum normal stress is negligible.

Shear Stress: To compare the shear stresses, the maximum first (static) moment of inertia S_y of the I-beam's cross-section must be calculated first.

$$S_y^{max} = \sum z_i F_i = z_f F_f + z_w F_w' = \left(\frac{h}{2}\right) F_f + \frac{\left(h - t_f\right)}{2} F_w' = \left(\frac{h}{2}\right) F_f + \frac{\left(h - t_f\right)}{8} F_w \Rightarrow$$

$$S_y^{max} = \left(\frac{h}{2}\right) F_f + \frac{\left(h - t_f\right)}{8} F_w \simeq \frac{h}{2}\, F_f \left(1 + \frac{1}{4}\frac{F_w}{F_f}\right) \tag{4.9}$$

If we assume that $\frac{1}{4}\frac{F_w}{F_f} \ll 1$, then the Eq. (4.2) is simplified:

$$q_{max} \simeq Q_z \frac{F_f\left(\frac{h}{2}\right)}{2F_f\left(\frac{h}{2}\right)^2} \simeq \frac{Q_z}{h} \tag{4.10}$$

Thus, the maximum shear flow is equal to the approximate value of Eq. (4.4).

Conclusion: If the Web's width t_w is negligible compared to height h so that $\frac{t_w^2}{h^2} \ll 1$ and the Flanges' cross-section area to the Web's cross-section area ratio is equal to $\frac{F_w}{F_f} \ll 4$, then the Flanges' normal stresses and the Web's shear stress can be calculated with satisfying accuracy using the simplified expressions:

$$\boldsymbol{\sigma_f = \pm\frac{M}{hF_f} = \pm\frac{L}{F_f}}, \text{ where } L = \frac{M}{h} \text{ and } \boldsymbol{q = \frac{Q}{h}} \tag{4.11}$$

The Equations (4.11) describe the stress problem of a beam that is composed of two Flanges (the upper and the lower) and a thin sheet metal (Web), with the assumption that the Web does not handle the bending moment M, but does handle only the shear force Q. Such a beam is called a shear beam. The shear beam's cross section is simplified into two concentrated areas (Flanges) and a thin Web.

As previously mentioned, the simplified beam's first and second moments of inertia are equal to:

$$\boldsymbol{I_y = 2\left(\frac{h}{2}\right)^2 F_f} \tag{4.12}$$

$$\boldsymbol{S(y) = F_f \frac{h}{2}} \tag{4.13}$$

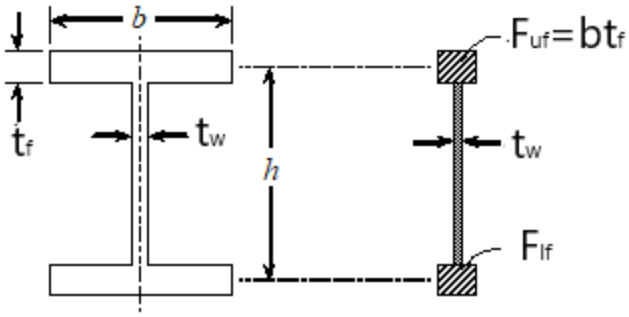

Εικόνα 33: Simplified I-Beam Cross-Section

The accuracy of Equation (4.11) depends mostly on the ratio $\frac{F_w}{F_f}$, where F_w is the Web cross-section area and F_f the Flange cross-section area. Thus, the importance of shear beams in Lightweight Structure Design -where the structure's weight minimization is critical- can be recognized. As a result, a beam's weight is minimized by placing Flanges where high bending stresses are developed and connecting them with thin Webs.

The smooth transmission of concentrated forces to the structure must also be taken into account, leading to the use of appropriate stiffeners. The Flanges usually consist of thin-walled industrial or pressed profiles or combinations of such profiles. Thin sheet metal presents minimal buckling resistance and can easily break when concentrated forces are applied. It is vital for the engineer to use appropriate stiffeners such as rods and ribs in order to ensure a smooth transmission of the concentrated forces to the structure.

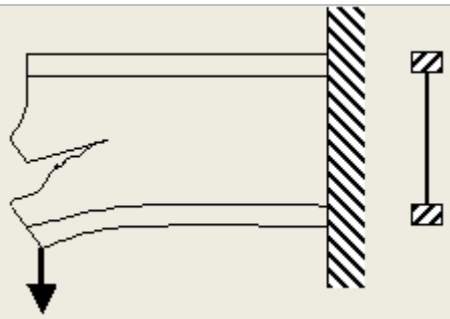	Danger of breaking if the concentrated force is not transmitted smoothly.
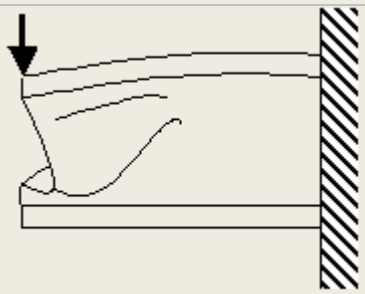	Danger of buckling if the concentrated force is not transmitted smoothly.
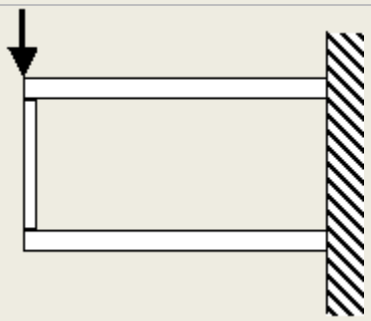	Rod placement to ensure the concentrated force is transmitted smoothly.
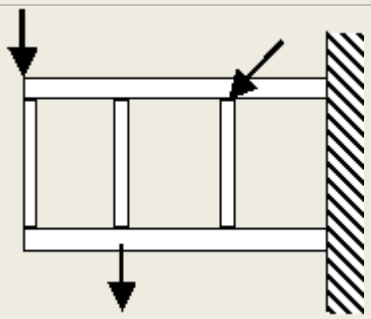	Appropriate stiffener placement where concentrated forces are applied, to ensure smooth transmission.

Πίνακας 8: Examples of Concentrated Force Transfer

4.1.3 Flight Design Envelope

It is understood that during the flight, from take-off to landing, the nature and the magnitude of external loads constantly change. Thus, the Flight Envelope of the aircraft is used. The Flight Envelope describes every possible aircraft load case, for example straight horizontal flight, maneuver, aerodynamic turbulence, landing etc. The Flight Envelope of each aircraft is unique, as different types of aircraft need to satisfy different demands.

As mentioned earlier, the Zenith Zodiac CH 650 B is classified as a Light Sport Aircraft (LSA). The Flight Envelope of the LSA category is presented below. Exceeding the design envelope may result in permanent deformation of the structure or catastrophic structural failure [19].

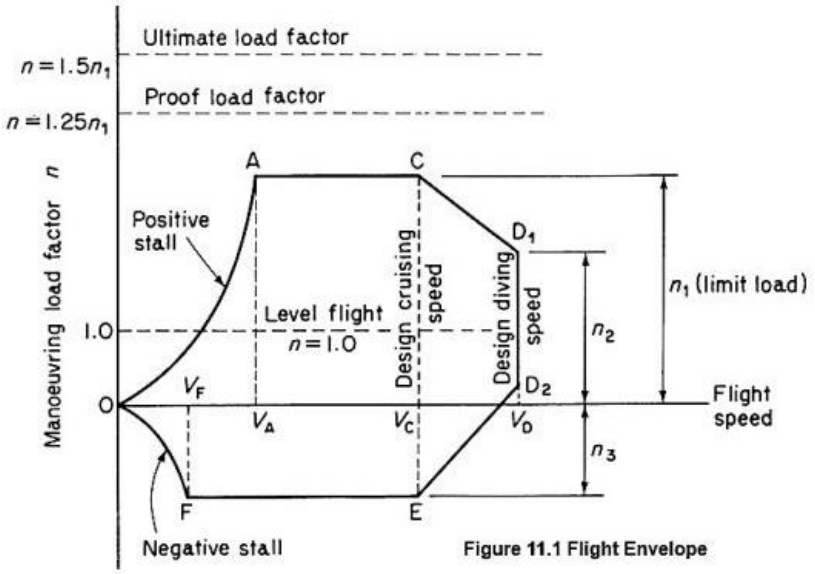

Εικόνα 34: Flight Design Envelope

In a load case scenario where the aircraft is operating at Line AC, the maximum positive load factor is applied.

In a correctly banked turn maneuver, the aircraft flies in a horizontal turn with no sideslip at constant speed [15]. If the radius of turn is R and the angle of bank is Φ, then the forces acting on the aircraft are those shown below:

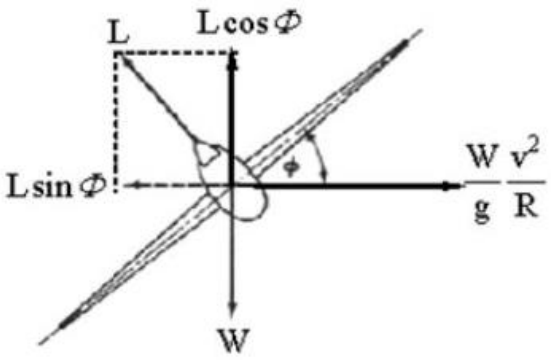

Εικόνα 35: Correctly Banked Turn

$$L \cdot sin\Phi = \frac{W}{g} \cdot \frac{V^2}{R}$$
$$L \cdot cos\Phi = W$$

$$n = \frac{L}{W} = \frac{L}{L \cdot cos\Phi} = \frac{1}{cos\Phi}$$

$$tan\Phi = \frac{V^2}{gR} \Rightarrow R = \frac{V^2}{g \cdot tan\Phi} \quad [m]$$

For horizontal flight turn, the tighter the turn, i.e. R is reduced, the greater the angle of bank Φ should be. If Φ is increased, load factor n is increased also. Aerodynamic theory shows that, for a limiting value of n, the minimum time taken to turn through a given angle occurs when the lift coefficient C_L is maximum, that is with the aircraft on the point of stalling [15].

When studying a load case with the maximum load factor applied at a correctly banked turn with the minimum time taken to turn, with the load factor known, the aircraft speed can be obtained from the Wing Lift Equation:

$$L_{wing} = \frac{1}{2}\rho V_{stall}^2 S_{wing} C_{L,max} \Rightarrow nW = \frac{1}{2}\rho V_{stall}^2 S C_{L,max} \Rightarrow V_{stall} = \sqrt{\frac{2nW}{\rho S_{wing} C_{L,max}}} \quad \left[\frac{m}{s}\right]$$

4.1.4 Aerodynamic Fundamentals

The main loads acting on the wing are:

- Aerodynamic Loads: Lift, Drag, Pitching Moment
- Engine Loads: Thrust, Engine Weight
- Landing Mechanism Loads: Vertical Loads, Braking
- Fuel Load
- Inertial Loads: Acceleration (translative and rotational), Oscillations (Aeroelasticity)

Weight: The wing structure must be strong enough to withstand not only aerodynamic loads acting on it but also its own structural weight along with the weight of the propulsion system mounted usually on the wing of the aircraft.

Thrust: Thrust is defined as the force produced by an aircraft's engines or propulsion system that propels the aircraft forward. It is a crucial aerodynamic force that opposes drag and is necessary for an aircraft to move through the air and maintain flight.

Airfoil: An airfoil is a streamlined shape that is designed to produce lift when it moves through a fluid. An airfoil typically has a curved shape, with the upper curved more than the lower surface. This curved shape is called an airfoil profile. Some important airfoil parameters such as the chord, the mean camber line and the leading and trailing edges are presented below.

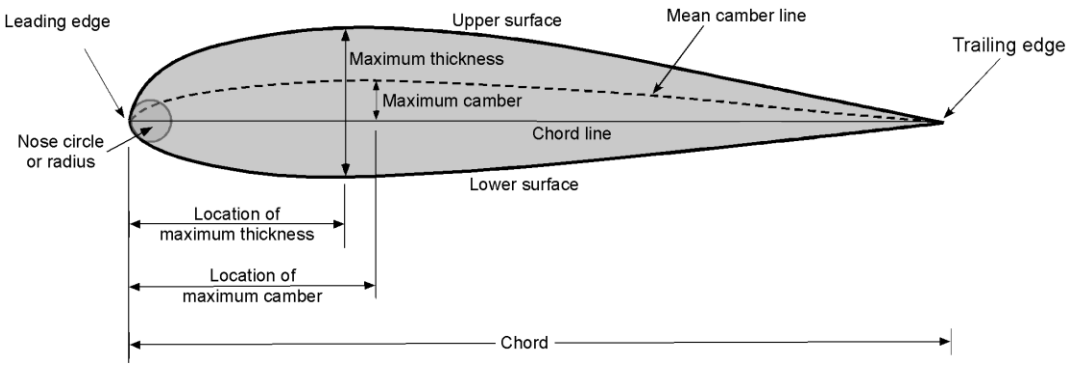

Εικόνα 36: Airfoil Parameters

Airfoil Pressure Distribution: Air pressure varies across the surfaces of the airfoil. Typically, the pressure on the upper surface of the airfoil is lower than the pressure on the lower surface. This pressure difference creates a net force called Lift, which is responsible for the aircraft's ability to generate upward force and stay aloft. The pressure distribution on an airfoil is explained by Bernoulli's principle, which states that as the airspeed increases, the air pressure decreases. On the upper surface of the airfoil, the airflow is faster, resulting in lower pressure, while on the lower surface, the airflow is slower, resulting in higher pressure. This pressure difference contributes to the Lift force.

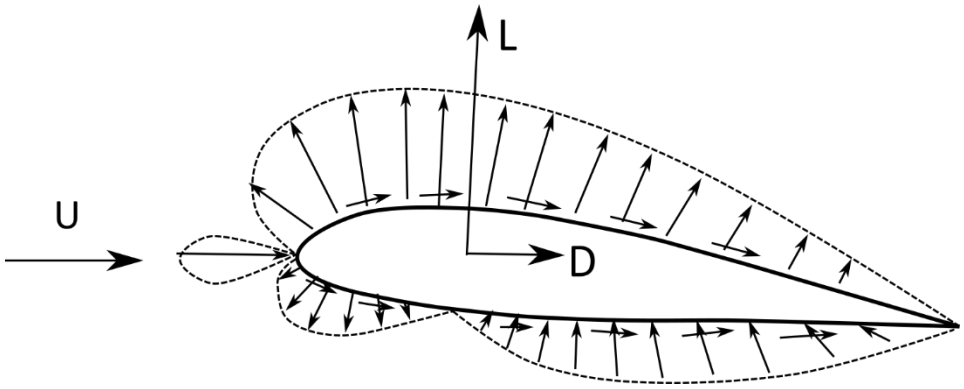

Εικόνα 37: Pressure Distribution around an Airfoil

Lift: Lift refers to the aerodynamic force that acts perpendicular to the relative motion of an object moving through a fluid. Lift is the force that opposes the force of gravity, allowing an aircraft to become airborne, stay aloft, and control its altitude and flight path.

Drag: It is the resistance or force that opposes the motion of an object as it moves through a fluid, such as air or water. Drag acts in the direction opposite to the object's motion and is caused by the interaction between the object and the fluid. Drag is divided in Parasitic and Induced Drag. Induced Drag is specific to lifting surfaces, such as the wings of an aircraft. It occurs as a byproduct of generating lift and is related to the production of wingtip vortices. Parasitic Drag includes all forms of Drag except for Induced Drag. It encompasses Pressure Drag (which is associated with the pressure differences between the front and rear surfaces of an object moving through a fluid) and Skin Friction Drag (which is caused by the resistance of the fluid to slide along the surface of the object).

The Lift and Drag forces can be expressed either as a function of the air velocity direction or as a function of the chord line. These two expressions are L,D and N,A respectively. The constituted force is R. The Angle of Attack (AoA) is the angle between the aircraft's chord line and the air's velocity direction. It is an important parameter regarding the generated Lift and Drag. It is depicted below as the angle α [6].

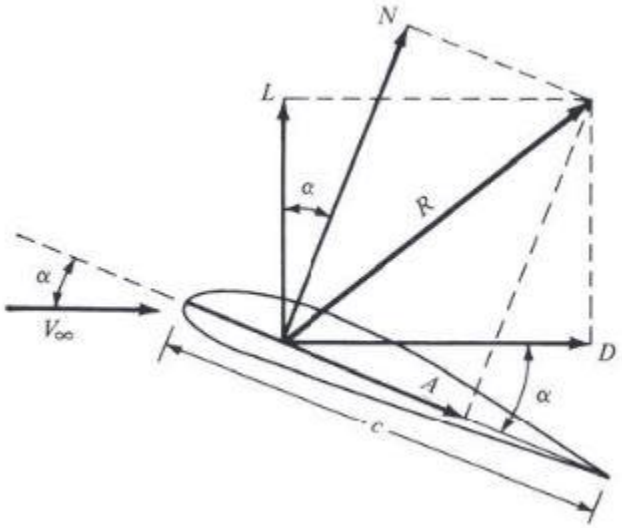

Εικόνα 38: Aerodynamic Lift (L,N) and Drag (D,A) Forces on an Airfoil

When the oncoming air interacts with an airfoil, the resultant constituted force is R, and there also a resultant moment or torque M, which is the Pitching Moment [6].

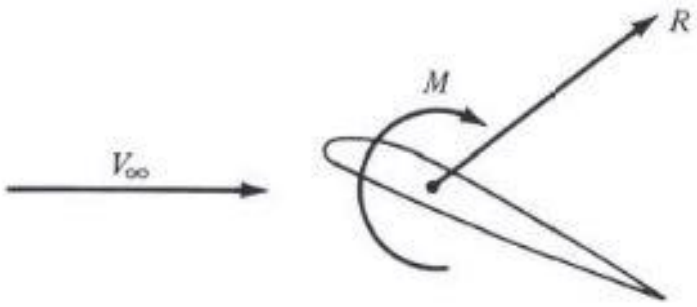

Εικόνα 39: Aerodynamic Constituted Force (R) and Moment (M)

Pitching Moment: It is the moment or torque that tends to cause an aircraft to rotate or pitch about its lateral axis. It is a measure of the tendency of the aircraft to rotate nose-up or nose-down and also one of the important parameters used to describe the stability and control characteristics of an aircraft. Pitching moments can be caused by various factors, including changes in the angle of attack, changes in airspeed, control surface deflections (elevator or stabilator movements), and shifts in the center of gravity (CoG) location.

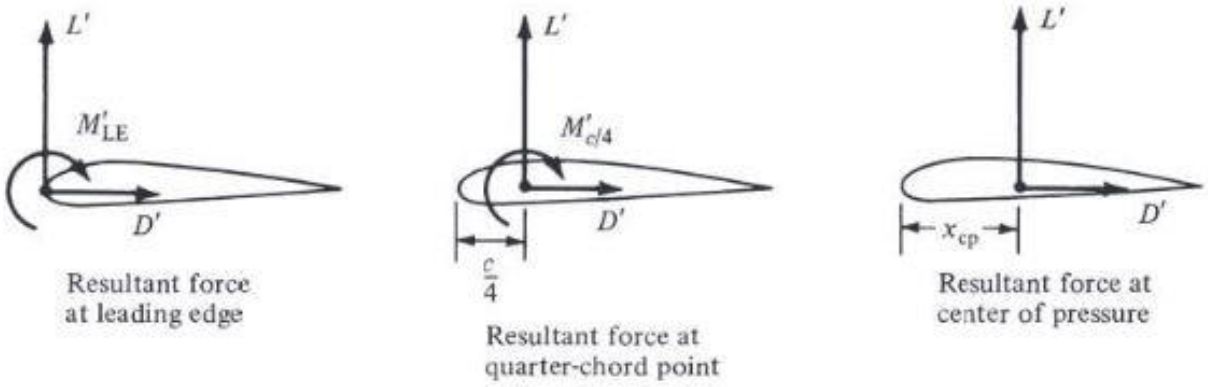

Εικόνα 40: Equivalent Aerodynamic Forces and Moments

Pressure Center: It is the location where the resultant of a distributed load effectively acts on the body. If moments were taken about the center of pressure, the integrated effect of the distributed loads would be zero. Hence, an alternate definition of the center of pressure is that point on the body about which the aerodynamic moment is zero [6].

Aerodynamic Center: The Pressure Center is not always a convenient concept in aerodynamics. However, this is no problem. To define the force-and-moment system due to a distributed load on a body, the resultant force can be placed at any point on the body, as long as the value of the moment about that point is also given. The Aerodynamic Center is usually assumed to be located at 25% of the chord line, towards the leading edge.

Lift Distribution: The spanwise distribution of Lift and Drag can be obtained from Aerodynamics [6]. As seen below, according to Prandl, the ideal distribution of Lift across the aircraft's wingspan follows an elliptical distribution in an elliptical wing. In rectangular and trapezoid wings, the ideal Lift distribution is not achieved and hence, the Schrenk distribution is applied. The Schrenk distribution essentially is the mean distribution of the ideal elliptical and the wing planform distributions [15].

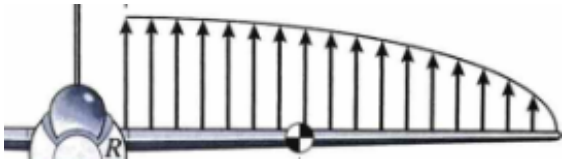

Εικόνα 41: Spanwise Elliptical Lift Distribution

Schrenk Distribution: The Schrenk distribution is an approximation method for the spanwise lift distribution which has been proposed by Dr. Ing Oster Schrenk and has been accepted by the Civil Aeronautics Administration (CAA) as a satisfactory method for civil aircraft [15]. The Schrenk method relies on the fact that the lift distribution does not differ much from elliptical planform shape if the wing is not swept and has no aerodynamic twist, i.e., zero lift lines for all wing sections lie in the same plane (constant airfoil section). The Schrenk method proposed that the lift distribution per unit span length is the mean value of actual wing chord distribution and an elliptical wing chord distribution that has the *same area* and the *same span*.

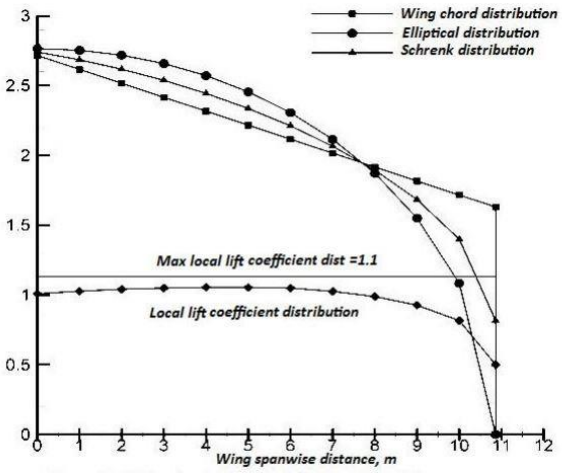

Εικόνα 42: Spanwise Schrenk Lift Distribution

Drag Distribution: The spanwise distribution of Lift and Drag can be obtained from Aerodynamics [6]. As seen below, according to Prandl, the ideal distribution of Drag across the aircraft's wingspan follows an elliptical distribution in an elliptical wing. The induced Drag is not taken into account due to its calculation escaping the purposes of this Diploma Thesis. Therefore, the Schrenk distribution is applied in rectangular and trapezoid wings. The Schrenk distribution essentially is the mean distribution of the ideal elliptical and the wing planform distributions [15].

4.1.5 Slipstream Effect

The slipstream effect is an aerodynamic effect related to propeller use and as a result impacts the production of Lift and Drag in an aircraft wing. In general, the stream tube behind a propeller in which the velocity of the axial flow is higher than the undisturbed flow and a rotational velocity is present, is called the propeller slipstream [13].

Aircraft components which are located behind the propeller experience the slipstream as a variation in the oncoming airflow, which have no parallel streamlines and different pressure distribution (consequently lift, drag and pitching moment). In general, all effects coming from the slipstream interaction with aircraft components are defined as indirect effects [13].

In this case, the beneficial effect of the propeller-fluid interaction allows for obtaining a higher lift capability for the wing. Indeed, the use of DEP and the effects of slipstream, among many benefits, involve a large reduction of the wing area, decreasing the friction drag, a higher cruise lift coefficient (close to the maximum efficiency point), less gust/turbulence sensitivity and comparable take-off and landing speed [13].

As previously mentioned, the use of Propellers in a DEP system presents the advantage of increasing the Lift during Take-Off, resulting in significant reduction of the needed Runway Length (STOL capabilities). The Slipstream effect will be studied as the Propeller use alters the **spanwise Lift Distribution** that a fixed wing would otherwise have, and thus the Load applied on the Wing Structure.

The Lift Distribution is altered when propellers are used, compared to a bare wing. The slipstream effect can be divided into the impact of slipstream velocity and the impact of slipstream rotation. The impact of slipstream velocity in Lift Distribution is due to the increase of air dynamic pressure, caused by the axially-induced propeller velocity, whereas the impact of slipstream rotation is due to the change of local angle of attack, caused by the tangentially-induced propeller velocity.

Lift is a function of the air dynamic pressure. The dynamic pressure in the wingspan region where the propeller is operating is increased, due to the propeller axially-induced velocity increased the total air velocity interacting with the wing.

Lift is also a function of the lift coefficient C_L which is dependent on the angle of attack. The local angle of attack is increased in the propeller rotating-up region and decreased in the propeller rotating-down region due to the propeller tangentially-induced velocity.

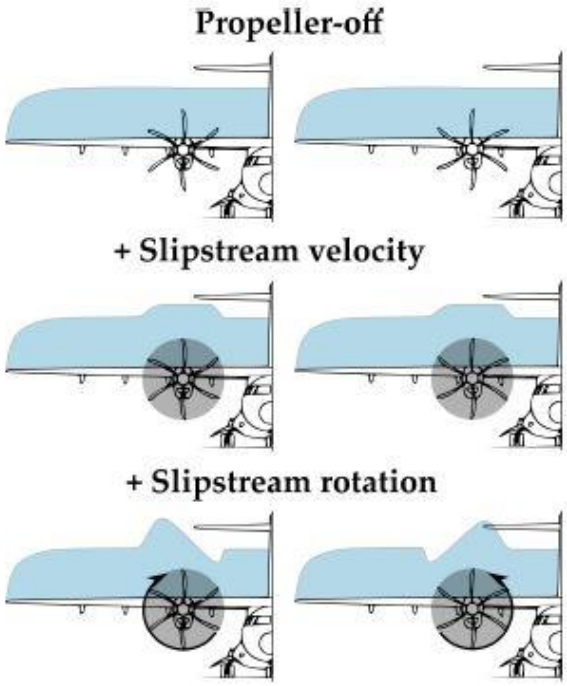

Εικόνα 43: Effects of Inboard-Up and Outboard-Up Propeller Slipstream on Lift Distribution

The calculation of the propeller slipstream velocity is completed below, using the Momentum Theory and the Disk Actuator Theory, where the propeller is considered a one-dimensional disk with an infinite number of blades [18].

Slipstream Velocity

The overall scheme of the velocity evolution in the propeller stream [14] and the definition of the distance between the propeller and the wing is shown below:

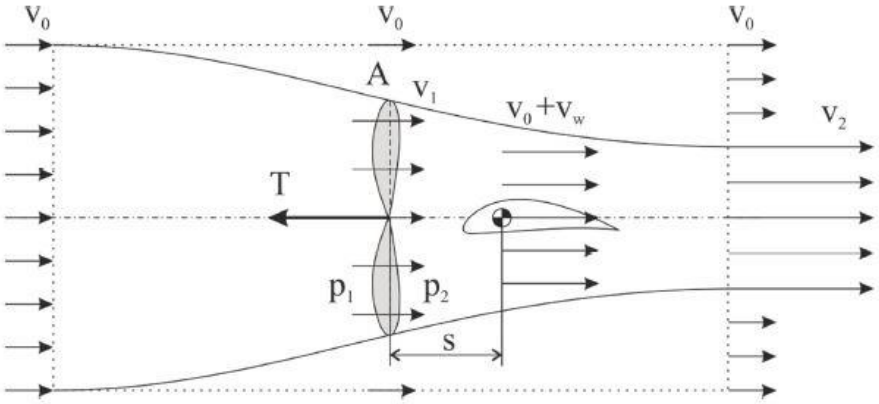

Εικόνα 44: Propeller-Air Interaction Flow Field

The additional axial velocity interacting with the wing is a function of propeller axially-induced velocity v_i and multiplied by the development factor k_d:

$$v_w = v_i k_d \quad [\frac{m}{s}] \tag{4.14}$$

The increase in velocity from the propeller is described by the development factor k_d, which depends on the distance of the propeller from the wing s and the propeller radius r:

$$k_d = 1 + \frac{s}{\sqrt{r^2+s^2}} \tag{4.15}$$

In order to calculate the propeller-induced velocity, the relationship between the propeller thrust and the propeller-induced velocity must be utilized. Using the Momentum Theory to model the flow field behind the propeller and the Actuator Disk Theory, the propeller thrust is equal to:

$$T = \dot{m}(v_2 - v_0) \tag{4.16}$$

Where T is the propeller thrust, v_0 is the freestream velocity and v_2 is the velocity behind the propeller [14]. The mass flow $\dot{m}$ corresponds to:

$$\dot{m} = A\rho v_1 \tag{4.17}$$

Where A is the area of the propeller disk and v_1 is the velocity at the propeller location. The propellers studied are designed to increase the dynamic pressure in landing and take-off conditions, i.e., at low flight speeds, so we could consider the flow without the effect of compressibility [14]. Thus, the speed v_1 can be thought of as the average of the input and output velocity and as the sum of freestream and induced velocity:

$$v_1 = \frac{v_2+v_0}{2} = v_0 + v_i \ \ [\frac{m}{s}] \tag{4.18}$$

After inserting the Equations (4.17) and (4.18) into Equation (4.16), Thrust is a function of the speed of flight and the value of the induced velocity:

$$T = A\rho(v_0 + v_i)2v_i \tag{4.19}$$

With the propeller Thrust known, the axially induced velocity is calculated from Eq. (4.19):

$$v_i^2 + v_0 v_i - \frac{T}{2A\rho} = 0 \tag{4.20}$$

The air velocity that interacts with the wing is:

$$\boldsymbol{v_{wing} = v_0 + v_w = v_0 + v_i k_d} \ \ [\frac{m}{s}] \tag{4.21}$$

The Equation (4.21) proves mathematically the Lift augmentation in a propeller-blown wing, as the velocity of the air interacting with the wing and producing Lift, is higher than the freestream air velocity.

Also, the Lift Equation equilibrium regarding a normal wing versus a DEP one, proves mathematically that for similar conditions (density, freestream velocity and angle of attack), the DEP wing produces the same amount of Lift that a normal wing with much larger surface area does.

$$L = L_{DEP} \Rightarrow$$

$$\frac{1}{2}\rho v_0^2 c_L S = \frac{1}{2}\rho(v_0 + v_w)^2 c_L S_{DEP} \Rightarrow$$

$$\frac{S}{S_{DEP}} = \frac{(v_0 + v_w)^2}{v_0^2}$$

Slipstream Rotation

The tangentially-induced velocity impacts the distribution of the already augmented lift, rather than the magnitude of it [18].

Essentially, in an “Inboard-Up, Outboard-Down” propeller, the local angle of attack is increased inboard and decreased outboard, following a sinusoidal form. Therefore, the point where the distributed Lift acts as a concentrated force is moved further inboard, improving the aircraft stability.

On the contrary, in an “Inboard-Down, Outboard-Up” propeller, the local angle of attack is decreased inboard and increased outboard, following a sinusoidal form. Therefore, the point where the distributed Lift acts as a concentrated force is moved further outboard, hampering the aircraft stability.

As seen below, the wingspan is divided in sections I, II, III and IV, moving from the wing root towards the wing tip. Since it is an “Inboard-Up, Outboard-Down” propeller, the local AoA is increased in sections I and II, and decreased in sections III and IV. The dynamic pressure is increased in sections II and III due to the propeller axially-induced velocity.

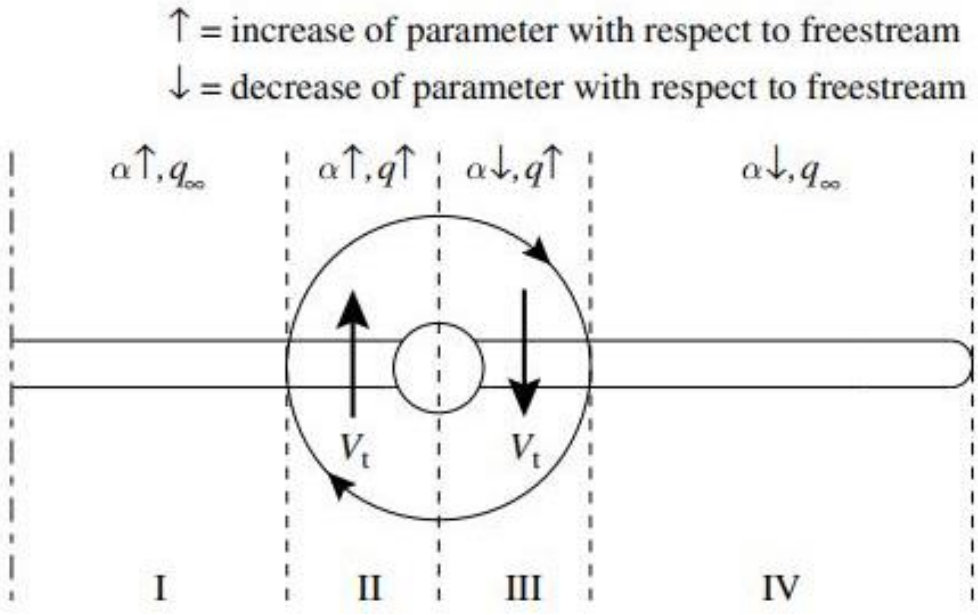

Εικόνα 45: AoA and Dynamic Pressure Change due to Inboard-Up Propeller Rotation

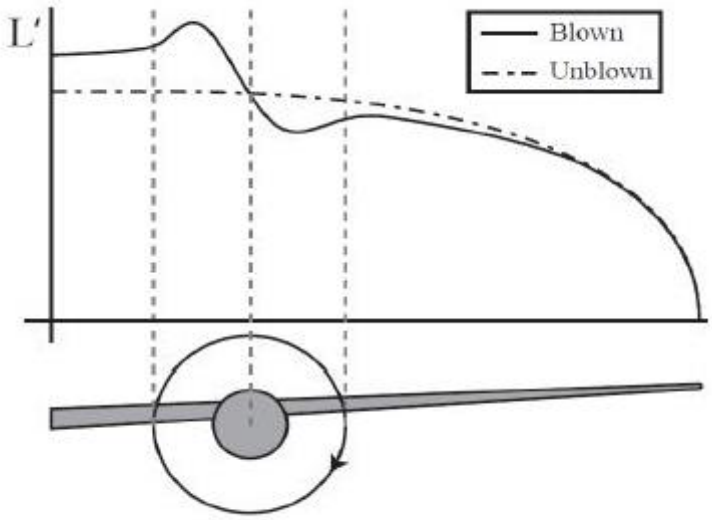

Εικόνα 46: Sinusoidal Variation in Lift Distribution due to Propeller Rotation

Due to this Thesis centered around a conceptual structural study and with the Momentum Theory and Disk Actuator Theory being followed as a low-fidelity, quick estimation method, the Slipstream rotation factor will not be taken into consideration regarding the tangentially-induced velocity. As a result, only the axially-induced velocity will influence the air interacting with the wing, and thus the Lift and Drag distribution.

The limitations of the methods referenced above are the lack of the tangential component in the propeller induced velocities, the oversight of the presence of the propeller hub and the inability to account for the drag component and the thrust deterioration at blade tips [18].

For the purposes of this Thesis, it is also assumed that the axially-induced velocity is constant along the propeller radius [18].

4.1.6 Wing Loads

Normal Stress

The first step in the Structural Analysis is the calculation of normal stresses. The normal stress will be calculated at the critical cross-section of the Spar. In order to locate the critical cross-section, the Shear Force Q and the Bending Moment M must be known. The Shear Force Q diagram is obtained by integrating the spanwise Load Distribution area and the Bending Moment M diagram is obtained by integrating the Shear Force Q area.

The Load Distribution is obtained by superposition of the wing distributed loads, such as Lift Distribution, Wing Structural Weight, Engine/Motor and Propeller Weights.

The Lift Distribution is obtained using the Schrenk Approximation Method [15], as the studied aircraft wing has a trapezoid planform (straight leading edge and tapered trailing edge).

$$L_y = \frac{1}{2} \cdot \rho \cdot V_y^2 \cdot c_y^{schrenk} \cdot C_{L,wing} \ [\frac{N}{m}] \tag{4.22}$$

where ρ the air density, V_y the air velocity in each section, c_y the wing chord in each section and C_L the wing lift coefficient. Thus, the Chord Distribution must be calculated. The studied span of one wing is $l = 3.255\,m$ will be discretized to a number of sections ranging in the y-axis, starting from $y = 0m$ to $y = 3.255m$.

Zenith Zodiac CH 650 B Wing Parameters			
Root Chord	$\boldsymbol{c_r}$	1.6	m
Tip Chord	$\boldsymbol{c_t}$	1.4	m
Area (One Wing)	$\boldsymbol{S_w}$	4.8825	m^2
Span (One Wing)	$\boldsymbol{l}$	3.255	m

Πίνακας 9: Wing Parameters

The aircraft's wing root chord is equal to $c_r = 1.6\,m$ and the wing tip chord is equal to $c_t = 1.4\,m$. Since the wing planform is trapezoid, the area of one wing is equal to:

$$S_w = S_{rectangular} + S_{triangle} = c_t l + \frac{1}{2}(c_r - c_t)l = 3.255\left(\frac{3}{2}1.6 - \frac{1}{2}1.4\right) = 4.8825\,m^2$$

The trapezoidal chord distribution is equal to:

$$c_y^{trap} = c_r\left(1 - 0.125\frac{y}{l}\right) = 1.6\left(1 - 0.125\frac{y}{3.255}\right)\ [m] \tag{4.23}$$

The Schrenk method proposes that the lift distribution per section is the mean value of actual wing chord distribution and an elliptical wing chord distribution that has the *same area* and the *same span*. In order to satisfy those two demands, we have an ellipse with radiuses r_1, r_2 with $r_2 > r_1$, $r_2 = l = 3.255m$ and $S_e = S_w = 4.8825m^2$. The ellipse quarter area is equal to $S_e = \frac{\pi}{4} r_1 r_2$, hence the radius $r_1 = \frac{4S_e}{\pi r_2} = 1.909m$.

The elliptical chord distribution is equal to:

$$c_y^{ellip} = r_1\sqrt{(1 - \left(\frac{y}{l}\right)^2} = 1.909\sqrt{(1 - \left(\frac{y}{3.255}\right)^2}\ \ [m] \tag{4.24}$$

The Schrenk chord distribution is equal to:

$$c_y^{schrenk} = \frac{1}{2}\left(c_y^{trap} + c_y^{ellip}\right)\ \ [m] \tag{4.25}$$

The local lift coefficient can be calculated by dividing the Schrenk chord distribution by the actual wing chord distribution, which in this case is trapezoidal. Essentially, the local lift coefficient in each section is equal to:

$$C_{L,local}(y) = \frac{c^{schrenk}(y)}{c^{trapezoidal}(y)}$$

The wing lift coefficient can be calculated by the expression [20]:

$$C_{L,wing} = \frac{C_{L_{airfoil}}}{0.95} \tag{4.26}$$

The wing Lift equation with the appropriate load factor provides the air velocity that the wing interacts with during Lift production.

With the propeller Thrust values known, the velocities v_0, v_i, v_{wing} of Eq. (4.14), (4.20), (4.21) from Slipstream Effect (Chapter 4.1.5) can be calculated for a DEP system.

Then, the Lift Distribution of each section can be obtained from Eq. (4.22). The overall Load Distribution can be calculated by subtracting the inertial loads (wing structural, fuel, motor or propeller distributed loads) from Lift Distribution:

$$p(y) = L_y - w_{total}(y) \quad [\frac{N}{m}] \tag{4.27}$$

Since the span is discretized, the Shear Force Q and the Bending Moment diagrams are obtained by numerical integration. The Trapezoid Rule is used:

$$Q_z(y) = -\int_0^{y_{tip}} p(y)dy = -\sum E(p) \text{ where } E(p) = \frac{p_i(y)+p_{i+1}(y)}{2} h \ [N] \tag{4.28}$$

$$M_x(y) = -\int_0^{y_{tip}} Q_z(y)dy = -\sum E(Q) \text{ where } E(Q) = \frac{Q_i(y)+Q_{i+1}(y)}{2} h \ [Nm] \tag{4.29}$$

The normal stress can be calculated using the Shear Flow Theory - explained in Chapter 4.1.2 - and specifically from Eq. (4.11). It is equal to:

$$\sigma_y(y) = \frac{M_x(y)}{h \cdot F_f(y)} \quad [MPa]$$

The Drag Distribution is obtained using the Schrenk Approximation Method [15], as the studied aircraft wing has a trapezoid planform (straight leading edge and tapered trailing edge).

$$D_y = \frac{1}{2} \cdot \rho \cdot V_y^2 \cdot c_y^{schrenk} \cdot C_{D,wing} \ [\frac{N}{m}] \tag{4.30}$$

where ρ the air density, V_y the air velocity in each section, c_y the wing chord in each section and C_L the wing lift coefficient.

The wing drag coefficient can be calculated by the expression [20]:

$$C_{D,wing} = \frac{C_{D_{airfoil}}}{0.95}$$

Drag is acting on the direction of the chord, while Lift is acting on a direction perpendicular to the chord. A simplified explanatory figure is presented below:

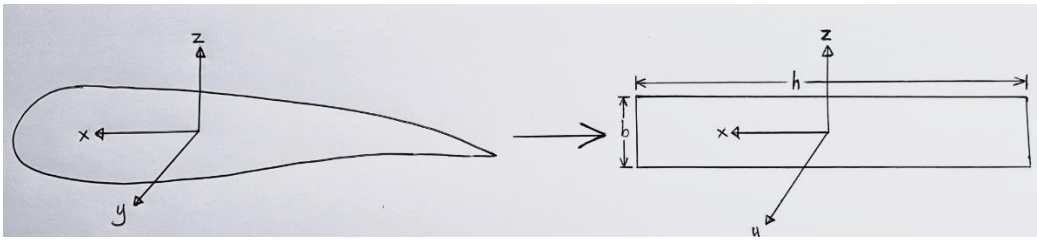

Εικόνα 47: Airfoil Cross-Section Simplification

Assuming that Lift acts on the figure's z-axis and Drag acts on the figure's x-axis, the second moment of inertia of the airfoil about axis x and z respectively is significantly different. If the airfoil is simplified as a rectangular beam, the second moments of inertia are equal to:

$$I_x = \frac{1}{12} h b^3$$

$$I_z = \frac{1}{12} h^3 b$$

Taking also into account the high Lift-to-Drag ratio of airfoils ($L \gg D$), the bending moment created by Lift is significantly higher than the respective bending moment created by Drag. Furthermore, a higher second moment of inertia equals a lower normal bending stress. Therefore, the normal bending stress created by Drag is minimal compared to the normal bending stress created by Lift. As a result, the contribution of Drag in normal stress calculation is often ignored, due to Drag corresponding to a low-magnitude, high-inertia load case, contrary to Lift which corresponds to a high-magnitude, low-inertia load case.

CoG of Distributed Load

The distributed load center of gravity corresponding to the equivalent concentrated force (for example the CoG of Lift Distribution) in a discretized area can be obtained by the equation:

$$y_{CG} = \frac{\sum y_{c,i} F_i}{\sum F_i} \ [m]$$

where $y_{c,i}$ the centroid of each rectangular section area and F_i the area of each rectangular section.

Shear Stress

The Pitching Moment is equal to:

$$M_P = \frac{1}{2}\rho V^2 S\bar{c}C_M \quad [\text{Nm}] \tag{4.31}$$

where $\overline{c}$ is the mean chord and C_M is the pitching moment coefficient.

Additional Moments are created by loads when they are not applied to the airfoil CoG which is also the Shear Center due to the airfoil being a closed section. As a result, the Torsion Moment is equal to:

$$M_T = M_P \pm \sum M = M_P \pm \sum(F \cdot d) \quad [Nm] \tag{4.32}$$

where F is a force and d is the lever arm of force F to the CoG/Shear Center.

The Shear Flow due to ***torsion***, according to Bredt's law, is equal to:

$$q_T = \frac{M_T}{2\Omega} \quad [\frac{N}{mm}] \tag{4.33}$$

where Ω the airfoil section surface area.

The Shear Flow due to ***shear*** is obtained by the superposition method [5], by addition of a closed section shear flow and an assumed-open section shear flow.

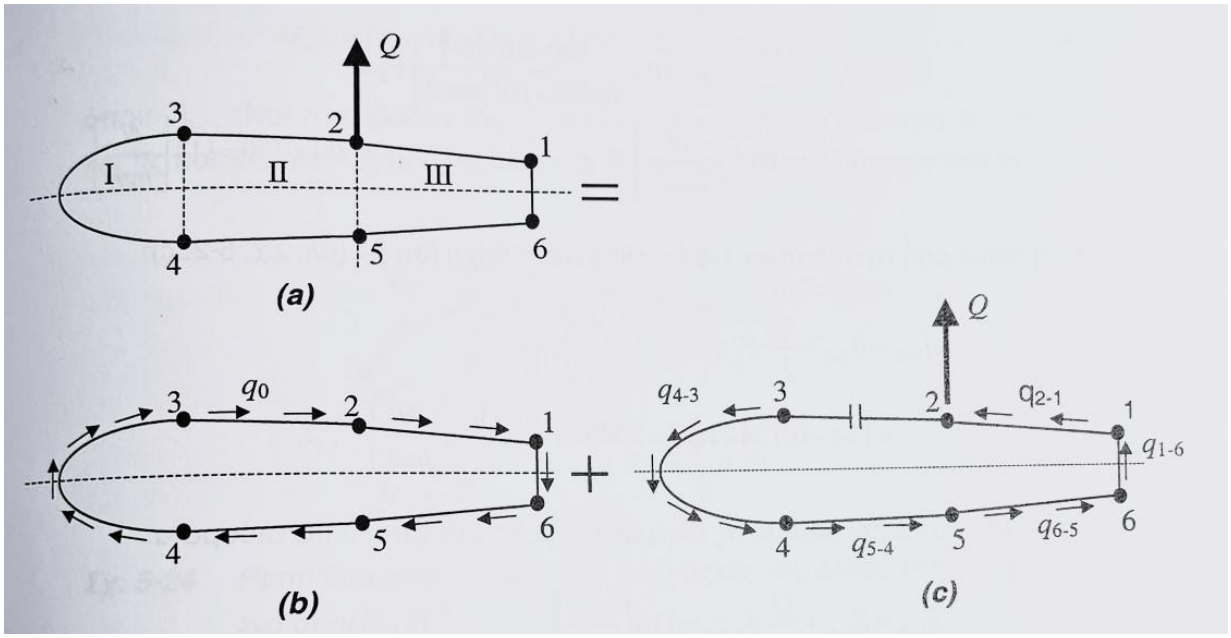

Εικόνα 48: Shear Flow Superposition [5], Closed (b) & Open (c) Sections

The assumed-open section Shear Flow is equal to:

$$\tilde{q}_n = \tilde{q}_{n-1} + \frac{Q_z}{I_x}\int z\, dF \simeq \tilde{q}_{n-1} + \frac{Q_z}{I_x} F_n z_n \quad \left[\frac{N}{mm}\right] \tag{4.34}$$

The closed section Shear Flow q_0 can be calculated from the aerodynamic center Moment equilibrium $\sum M_{i-j} = 0$, where $M_{i-j} = 2A_{i-j}q_{i-j}$.

$$q_0 = -\frac{\sum A_{i-j}q_{i-j}}{\sum A_{i-j}} \quad [\frac{N}{mm}] \tag{4.35}$$

The total Shear Flow due to shear can be obtained by superposition of Eq. (4.34), (4.35) and combined with the Shear Flow due to torsion, the Shear Stress is equal to:

$$q = q_0 + \tilde{q} \quad [\frac{N}{mm}] \tag{4.36}$$

$$\tau = \frac{q+q_T}{t} \quad [MPa] \tag{4.37}$$

Equivalent Stress

The equivalent stress according to Von Mises is equal to:

$$\sigma_{eq} = \sqrt{\sigma^2 + 3\tau_{max}^2} \quad [MPa] \tag{4.38}$$

Riveting

When forces are applied to a riveting, the bearing pressure applied to the rivet is equal to:

$$p_b = \frac{T}{d \cdot t_1} \quad [MPa]$$

The pressure applied to the rest of the joint is equal to:

$$p_b = \frac{T}{d \cdot (t_2 + t_3)} \quad [MPa]$$

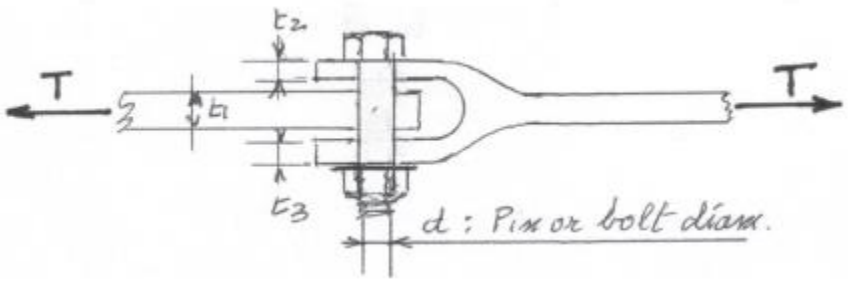

Εικόνα 49: Forces Acting on a Riveting

Holes created in order to house riveting result in increased stress values, as seen below. This phenomenon is called stress concentration and is associated with the geometry.

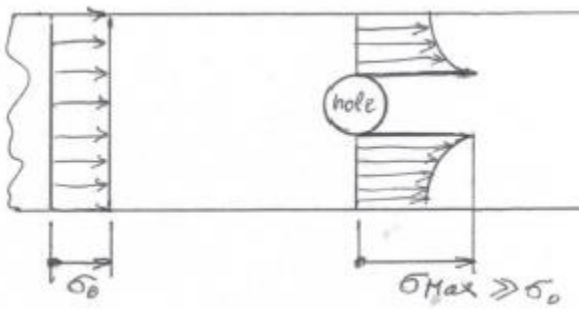

Εικόνα 50: Riveting Stress Concentration

A usual measure to combat stress concentration is to align the holes and to alternate their diameters.

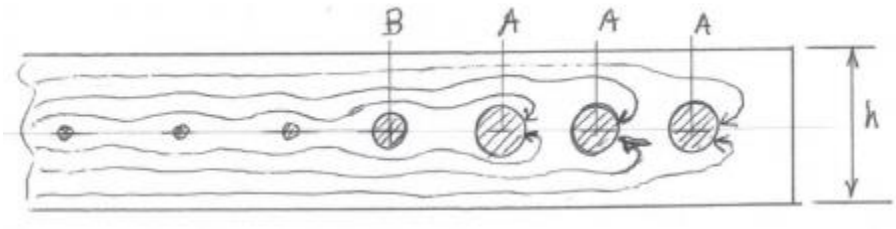

Εικόνα 51: Methods of Alleviating Stress Concentration

When 2 rivets are used, each rivet handles ½ of the load. When 3 rivets are used, each rivet handles 1/3 of the load etc. For safety reasons (increased factor of safety), the ratio below can be used:

2 ηλώσεις				
	0.5	0.5		για N=1
	0.6	0.4		για N=1.2
	0.4	0.6		για N=1.2
	0.75	0.75		για N=1.5
3 ηλώσεις				
	0.33	0.33	0.33	για N=1
	0.4	0.2	0.4	για N=1.2
	0.5	0	0.5	για N=1.5

Εικόνα 52: Riveting Ratios for different Factors of Safety and Number of Rivets

The riveting bearing pressure must be checked at the rivets handling the largest loads.

Deflection

The Curvature Surfaces Method is used to calculate the wing's deflection. The beam's bending moment M diagram is divided by the Young's elastic modulus E and the cross-section's second moment of inertia I. The new M/EI diagram expresses the beam's curvature as a function of its length. The surface area of the M/EI diagram is called the curvature surface of the beam.

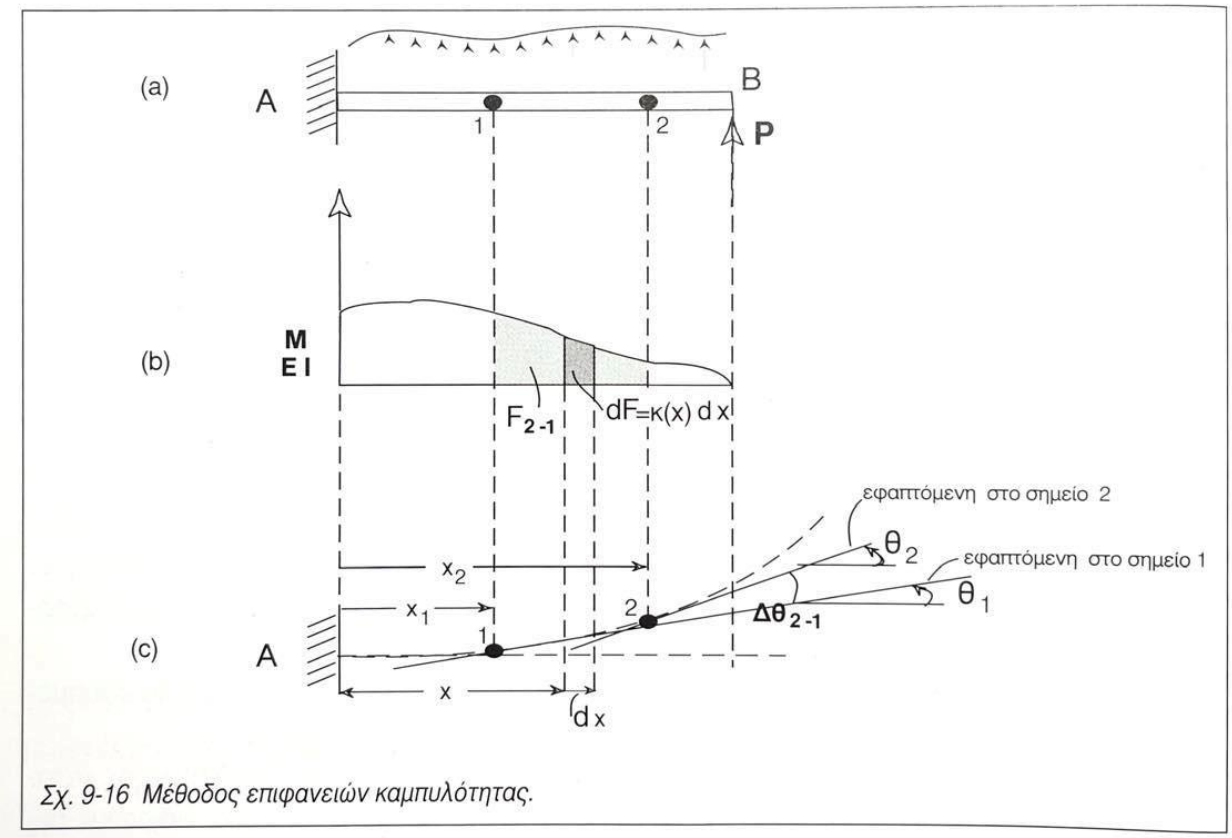

Εικόνα 53: Curvature Surfaces Method (1/3)

Assuming two beam axis points 1 and 2, as pictured above. In the deformed state, an angle $\Delta\theta_{2-1}$ between the tangent lines θ_1 and θ_2 is created. This angle must be equal to the curvature surface between points 1 and 2. Therefore:

$$\Delta\theta_{2-1} = \theta_2 - \theta_1 = \int_{x_1}^{x_2} \frac{M(x)}{E \cdot I(x)} dx \tag{4.39}$$

Symbolizing the curvature surface area as F_{2-1}, the equation above can be expressed in a simpler manner as $\Delta\theta_{2-1} = F_{2-1}$.

In order to calculate the deflection of the beam at point 2 relative to point 1, the impact of curvature on an infinitesimal element dx must be investigated. Therefore, it is assumed that the beam besides the element dx is undeformed. The elastic element dx with the bending moment M(x) acting on it, is deformed as a cycle arc, as seen below, and the tangent lines at points 1 and 2 form an angle dθ equal to the curvature surface corresponding to the infinitesimal element. Those tangent lines intersect the vertical line at point 2 of the beam at two points separated by a distance of $dv = d\theta(x_2 - x)$.

Substituting the distance, $dv = \frac{M(x)}{EI(x)}(x_2 - x) = dF(x_2 - x)$. The factor $dF(x_2 - x)$ is the static or first moment of inertia of surface dF about the vertical axis intersecting point 2.

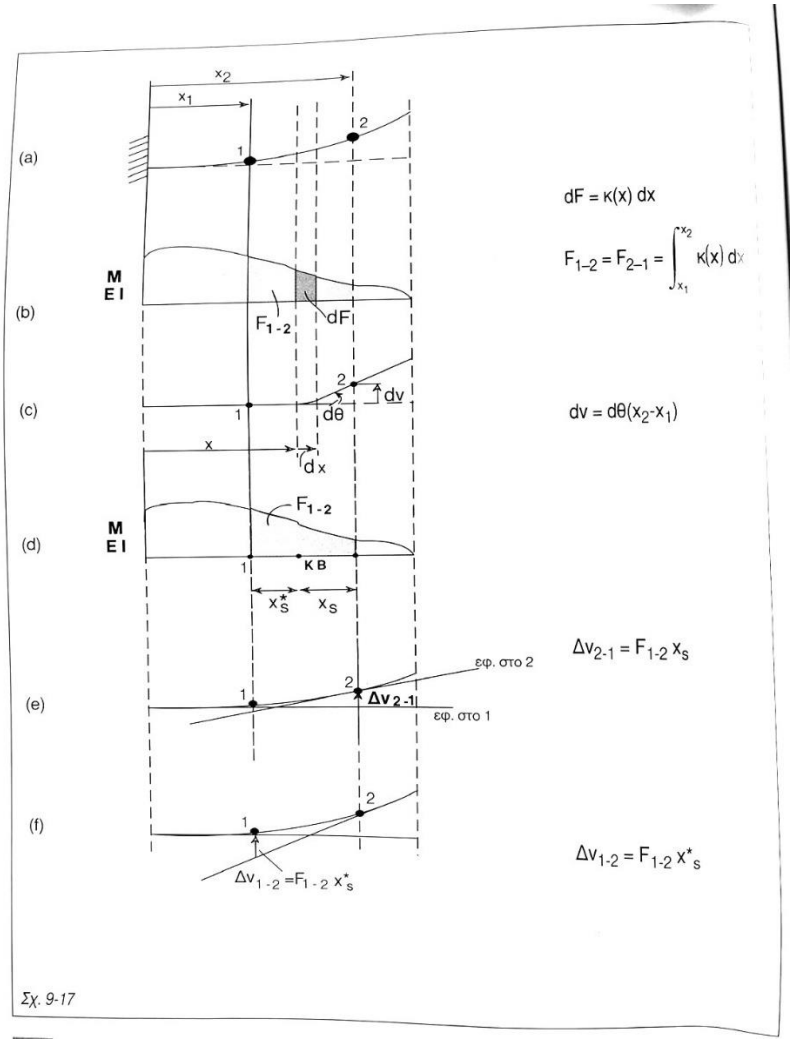

Εικόνα 54: Curvature Surfaces Method (2/3)

Assuming the whole section between points 1 and 2 is elastic, the impact of every element's curvature on the deflection will occur by integration between x1 and x2. Therefore, the deflection Δv_{2-1} of point 2, caused by the deformation of the beam section between points 1 and 2 is equal to:

$$\Delta v_{2-1} = \int_{v_1}^{v_2} dv = \int_{x_1}^{x_2} d\theta (x_2 - x) = \int_{x_1}^{x_2} \frac{M(x)}{EI(x)} (x_2 - x)\, dx$$

Knowing that the static or first moment of inertia of a surface about an axis is equal to the surface area times the center of gravity distance from the axis, the formula above can be expressed as $\Delta v_{2-1} = F_{2-1} x_s$, where F_{2-1} is the curvature surface area between points 1 and 2, and x_s is the distance separating the center of gravity of the surface F_{2-1} from the vertical line at point 2.

As seen below, the total displacement of point 2 is equal to the deflection of point 1, plus the slope of point 1 θ_1 times the distance $x_2 - x_1$, plus the quantity Δv_{2-1}.

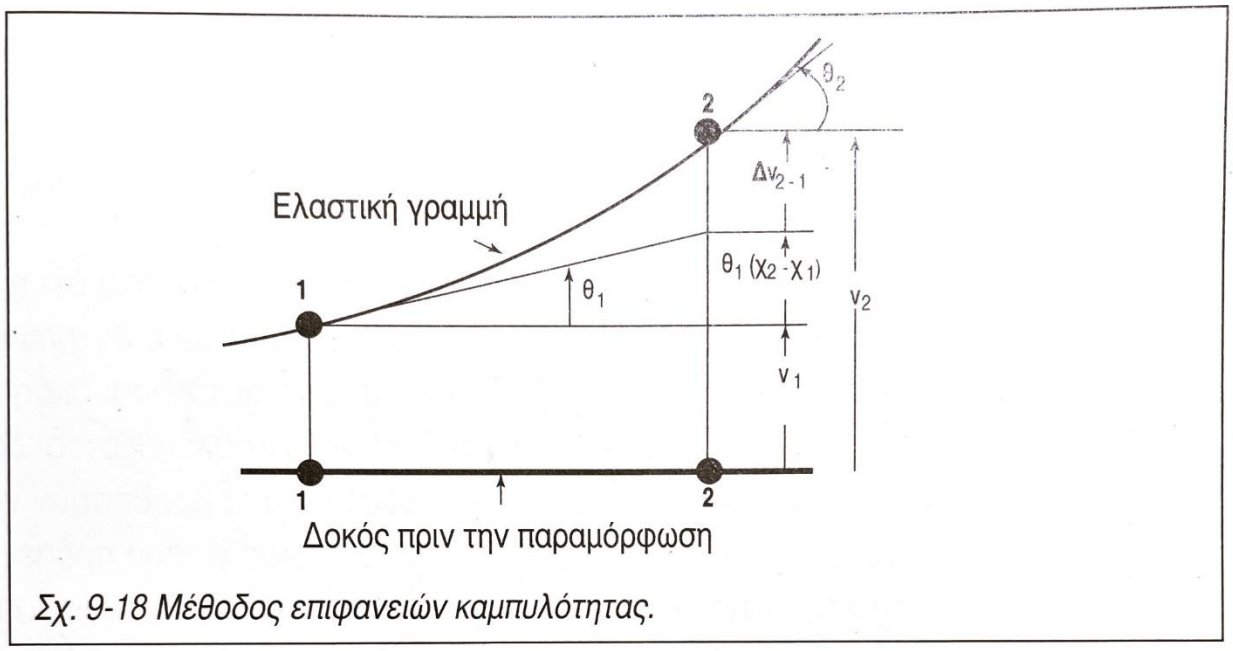

Εικόνα 55: Curvature Surfaces Method (3/3)

$$v_2 = v_1 + \theta_1 (x_2 - x_1) + \int_{x_1}^{x_2} \frac{M(x)}{E \cdot I(x)} (x_2 - x_1) dx \quad [m] \tag{4.40}$$

4.1.7 Runway Length

The Takeoff distance can be calculated from Raymer's book [24]. Takeoff distance is calculated from the graph below, using the Take Off Parameter (TOP). The (TOP) can be calculated from the equation below:

$$(TOP) = \frac{(W/S)}{\sigma C_{L,max}(HP/W)}$$

where W/S is the wing loading in $\frac{lb}{ft^2}$, i.e. the aircraft MTOW divided by the wing surface, $\sigma = \frac{\rho}{\rho_{@sea\ level}}$ is the density ratio and obviously equal to $\sigma = 1$ at sea level, $C_{L,max}$ is the maximum lift coefficient and (HP/W) is the aircraft power-to-weight ratio in $\frac{HP}{lb}$.

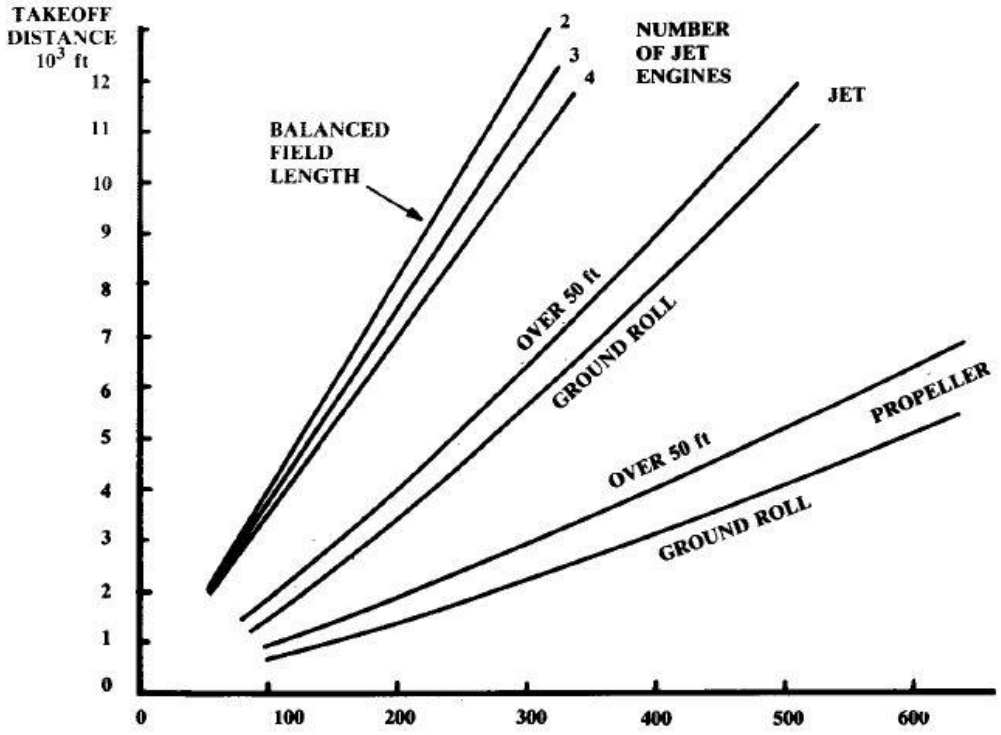

Εικόνα 56: Takeoff Distance Estimation Graph

After calculating the (TOP), Takeoff Distance can be estimated using the graph above and specifically the Ground Roll curve.

4.2 ASSUMPTIONS

The structural analysis assumptions are presented below:

- The aircraft has a trapezoidal wing planform with a straight leading edge and a tapered trailing edge. For the calculation of chord and lift distributions, the Schrenk method is used.
- Motor and propeller weights are distributed along their respective regions. Electricity power lines made from Aluminum are considered, but their weight and positioning is not taken into account.
- The reduction in weight due to liquid hydrogen use is minimal. Therefore, the aircraft weight is assumed constant (and equal to the MTOW) during the whole flight. As a result, structural safety in reality is increased.
- The analysis can be performed numerically in Excel, discretizing the wingspan in sections.
- When calculating the velocity from the lift equation for a given load factor, half of the MTOW is used since only the semispan is studied.
- In DEP configurations, where propellers create the slipstream effect, the velocity calculated from the lift equation for a given load factor is not equal to the True Aircraft Speed, due to the increase in dynamic pressure of air.
- The slipstream rotation and thus the propeller radially-induced velocity, are not taken into account while calculating the lift distribution.
- The wingtip vortex is assumed eliminated due to the wingtip-mounted cruise propeller. Thus, induced drag is also eliminated, and the Schrenk method can also be used to calculate the drag distribution.
- The induced drag in the original configuration is ignored due to its calculation escaping the purposes of this Thesis. Hence, the drag distribution can be calculated using the Schrenk method.

- The shear force and bending moment created by the drag distribution can be ignored during normal stress calculations, first due to drag being significantly lower compared to lift according to the airfoil lift-to-drag ratio and second due to difference in second moments of inertia of the airfoil cross-section, corresponding to the direction lift and drag are acting. Essentially, drag is a low-magnitude load acting on a direction with a high second moment of inertia, while lift is a high-magnitude load acting on a direction with a low second moment of inertia.
- The lift force can be assumed to be applied on the wing spar, which is located at the aerodynamic center, at 25% of the chord distance, measuring from the leading edge.
- Normal stresses (compression and tension) are not handled by the skin (upper and lower respectively), only by the wing spar.
- The wing spar flanges handle the normal stresses, while the wing spar web handles the shear stresses, both due by bending.
- The wing spar web, located between the two flanges, is flat and remains flat during bending.
- The wing spar cross-section is thin walled ($t/H < 0.1$), where t is the width and H is a characteristic dimension of the cross-section.
- The beam (wing) length is large ($t/L < 0.1$), where L is the beam length (semispan).
- During skin shear flow and stress calculations due to shear, a constant wing cross-section with a mean chord calculated from the root and tip chord values can be assumed, thus not taking into account the wing taper ratio.
- The material used (Al6061-T6) is isotropic.
- The horizontal correctly banked turn in the analysis corresponds to a pure roll maneuver of the aircraft, assuming that the roll and yaw maneuvers are decoupled.
- The nacelles housing the High-Lift and Cruise electric motors, can be considered a non-structural member of the wing and thus assumed not stressed.

4.3 FINITE ELEMENTS

4.3.1 Finite Element Theory

Finite Element Methods were developed in the 1950s, due to the need for more accurate studies compared to analytical methods, and are used in a wide range of applications. In FEA, the behavior of the structure is approximated by a set of mathematical equations derived from the principles of continuum mechanics. These equations govern the relationship between stresses, strains, displacements, and other mechanical quantities within each finite element. By discretizing the structure into smaller elements, FEA transforms these partial differential equations into a system of algebraic equations that can be solved numerically. The finite element method relies on the interpolation of nodal displacements or other variables within each element using shape functions. These shape functions define how the values of the primary variables vary spatially within the element. By imposing equilibrium and compatibility conditions at the element boundaries and nodal points, FEA ensures the continuity of displacement and stress fields throughout the structure. FEA procedure includes matrix calculations, geometrical transform implementation and requires deep understanding of each element's theoretical background. The analysis is completed by computer.

The simplest FEA is that of a 2D truss. From the relation between forces and displacements, we can obtain the vector equation for a bar element:

$$\{P\} = [K]\{u\} \tag{5.1}$$

where P are the nodal forces and u the respective displacements. The stiffness matrix K connects forces and displacements. In a typical analysis, the forces and the stiffness matrix are known. By solving the system, the displacements are obtained and thus the strains. Forces are essentially the system's boundary conditions. The stiffness matrix K depends on the local geometry of each element, the material and the type of analysis performed.

For the 2D bar example, the steps are the following: 1) System discretization/meshing, 2) Calculation of the stiffness matrix, 3) Calculation of the bar forces, 4) Equation solving

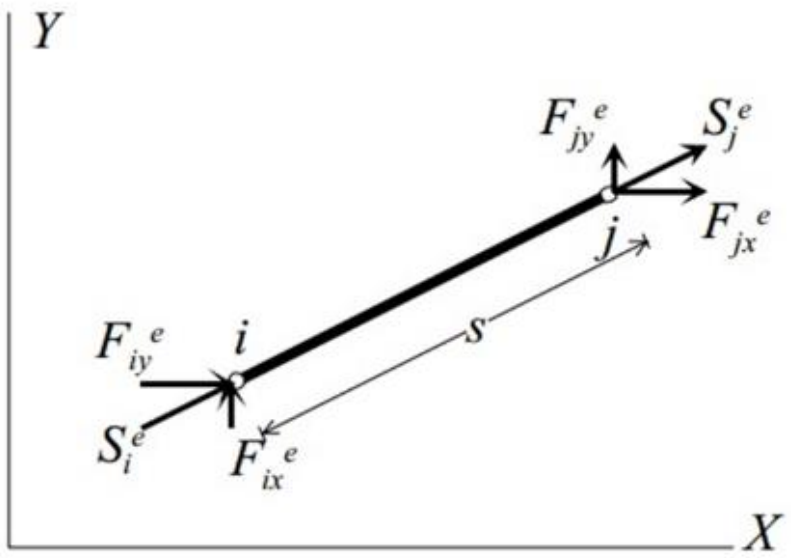

Εικόνα 57: 2D Bar Element Free Body Diagram

4.3.2 Finite Elements Analysis Software

In this case, the use of a commercial program is necessary, as wing geometries are very complex. Therefore, ANSYS Workbench Static Structural is used for a 3D analysis utilizing. ANSYS Workbench is a leading software platform for engineering simulation. It offers a user-friendly interface and a wide range of tools for pre-processing, solving, and post-processing FEA simulations. The following sections describe the process of setting up and analyzing a finite element model in ANSYS Workbench.

Pre-processing

Geometry Import: The first step is importing the CAD geometry of the commercial aircraft wing with Distributed Electric Propulsion into ANSYS Workbench. The geometry must be clean and suitable for meshing.

Mesh Generation: A mesh for the wing structure using appropriate meshing techniques is generated. ANSYS Workbench provides various meshing tools, including automatic meshing algorithms and manual mesh controls, to ensure a high-quality mesh.

Setting Up the Finite Element Model

Material Properties: Material properties of the wing components are defined, including Young's modulus, Poisson's ratio, and density. These properties are crucial for accurately simulating the structural behavior of the wing.

Boundary Conditions: Appropriate boundary conditions to the finite element model are applied, in order to represent the loading and support conditions experienced by the wing during operation. This may include aerodynamic loads, distributed propulsion forces, and constraints at attachment points.

Solving the Finite Element Model

Solver Settings: Solver settings in ANSYS Workbench are configured, including convergence criteria, solution methods, and other numerical parameters.

Solution Process: The solution process is initiated, in order to compute the response of the finite element model under the applied loads. ANSYS Workbench utilizes advanced algorithms to efficiently solve large-scale FEA problems.

Post-processing

Results Visualization: Visualize the results of the finite element analysis using ANSYS Workbench's post-processing tools. Plot contours of stress, strain, displacement, and other relevant quantities to gain insights into the structural behavior of the wing.

Analysis of Results: Simulation results are interpreted, in order to evaluate the structural behavior of the commercial aircraft wing with Distributed Electric Propulsion. Results in areas of high stress and deformation are identified and compared to the respective analytical.

The imported geometry must be designed either in ANSYS’s Space Claim or imported as an STP file, designed in CAD software i.e. Dassault CATIA, Dassault SolidWorks, Autodesk Inventor etc.

5.0 THESIS REVIEW

5.1 SUMMARY

This Student Thesis investigates the definition of Distribution Propulsion. A Literature Review is performed investigating the types of Distributed Propulsion, potential advantages and disadvantages. Growing sustainability demands lead to a thorough look on the All-Electric Aircraft. Moreover, a brief Historical Review regarding conceptual and actual DP as well as AEA aviation milestones is presented.

The general aviation aircraft selected to be implemented with a Distributed Electric Propulsion powered by a liquid Hydrogen Fuel-Cell system is also presented. Designs and specifications are shown, while also showcasing its wing structure.

The Student Thesis also provides the methodology and framework behind a wing structural analysis. Basic principles of Strength of Materials, Lightweight Structures and Aerodynamics are presented, leading to the expression of equations based on theories used in the analytical method. Finally, a brief introduction to Finite Element basic theory was made.

5.2 BRIDGING THEORY TO APPLICATION

The basic framework provided in this Student Thesis can be expanded and applied to the Diploma Thesis. Two structural analyses using both analytical and FEA methods can be performed in order to see the structural behavior (normal, shear, equivalent stress and deformation) of the wing with the DEP system compared to the original configuration.

The analytical method requires a very precise calculation of the aerodynamic loads produced by the DEP system operation, whereas the FEA method utilizes the ANSYS Workbench software but requires prior design and modeling of the wing structure in both configurations in CAD software.

The structural analysis results along with the evaluation of performance improvements will lead to useful conclusions regarding implementation of alternative and sustainable propulsion solutions in current and future aviation.

REFERENCES

1. Gohardani, A. S., Doulgeris, G., & Singh, R. (2011). Challenges of future aircraft propulsion: A review of distributed propulsion technology and its potential application for the all-electric commercial aircraft. In *Progress in Aerospace Sciences* (Vol. 47, Issue 5, pp. 369–391). https://doi.org/10.1016/j.paerosci.2010.09.001
2. Kim, Hyun Dae (2010). Distributed Propulsion Vehicles, 27th International Congress of the Aeronautical Sciences, 2010
   https://ntrs.nasa.gov/citations/20100036222
3. Ko, A., Schetz, J. A., & Mason, W. H. (2003). Assessment of the Potential Advantages of Distributed Propulsion for Aircraft
   https://www.academia.edu/80005621/Assessment_of_the_potential_advantages_of_distributed_propulsion_for_aircraft?f_ri=24557
4. Katsiropoulos, C. (2018), Introduction to Aeronautical Materials, Lecture 10: New Trends in Aviation, University of Patras, Greece
5. Kermanidis T., Labeas G., (2021), Lightweight Structures and Aircraft Structure Analysis, University of Patras, Greece
6. Anderson Jr, J., (2017), Fundamentals of Aerodynamics - Sixth Edition, McGraw-Hill Education, USA
   https://aviationdose.com/wp-content/uploads/2020/01/Fundamentals-of-aerodynamics-6Edition.pdf
7. Unifier-19, retrieved from:
   https://www.unifier19.eu/www.unifier19.eu/index.html
8. HY4, retrieved from:
   https://www.h2fly.de/
9. X-57 Maxwell, retrieved from:
   https://www.nasa.gov/aeronautics/x-57-maxwell/
10. Al6061-T6, retrieved from:
    https://www.makeitfrom.com/material-properties/6061-T6-Aluminum
11. Zenith Zodiac CH 650 B Engines, retrieved from:
    http://www.zenithair.com/zodiac/xl/3300.html
    http://www.zenithair.com/zodiac/xl/o200.html
12. Zenith Zodiac CH 650 B, retrieved from:
    https://zenithair.net/
13. Cusati, V., Corcione, S., Nicolosi, F., & Zhang, Q. (2023). Improvement of Take-Off Performance for an Electric Commuter Aircraft Due to Distributed Electric Propulsion. Aerospace, 10(3). https://doi.org/10.3390/aerospace10030276
14. Hospodář, P., Klesa, J., Demovič, D., & Žižkovský, N. (2022). Aerodynamic and Structural Aspects of a Distributed Propulsion System for Commuter Airplane. *Aerospace*, *9*(11). https://doi.org/10.3390/aerospace9110712

15. 10 Prepared, C., & Al-Hussaini, A. A. (2013). UOT Mechanical Department / Aeronautical Branch Aircraft Design Chapter Ten / Air-Inertia Load Distribution. https://uotechnology.edu.iq/dep-MechanicsandEquipment/Lectures%20and%20Syllabus/Lectures/Aircraft/Foruth%20Grade/Aircraft%20Design3.pdf
16. GA 35-A-415 Airfoil Data, retrieved from: https://www.bigfoil.com/f775da41-bbff-4788-9a16-5afd1009622f_info.php
17. Ganesh, R. V. (2018). Design Optimization of a Regional Transport Aircraft with Hybrid Electric Distributed Propulsion Systems. https://vtechworks.lib.vt.edu/bitstream/handle/10919/84494/Rajkumar_V_T_2018.pdf?isAllowed=y&sequence=1
18. Load Factors, Maneuvers, Banked Turns Flight Design Envelope, retrieved from: https://www.flight-study.com/2021/01/load-factors-aerodynamics-of-flight.html?m=1&expand_article=1
19. Sadraey, M. (n.d.). *CHAPTER 5 WING DESIGN*. http://wpage.unina.it/fabrnico/DIDATTICA/PGV_2012/MAT_DID_CORSO/09_Progetto_Ala/Wing_Design_Sadraey.pdf
20. RAYMER(*Aircraft Design - A Conceptual Approach 2nd Ed. - D. Raymer (1992) WW*, n.d.) https://www.airloads.net/Downloads/Textbooks/Aircraft%20Design-A%20Conceptual%20Approach.pdf